Analysing wave-induced velocity fields around a saltmarsh cliff

An experimental study on the application of Particle Imaging Velocimetry in a complex hydrodynamic region

Pieter Faber

14-12-2023

Supervisors:
dr.ir. B.W. Borsje
dr.ir. J.J. van der Werf
ir. J.R.M. Muller
ir. D. Dermenzoglou

UNIVERSITY OF TWENTE.

Analysing wave-induced velocity fields around a saltmarsh cliff

An experimental study on the application of Particle Imaging Velocimetry in a complex hydrodynamic region

Pieter Faber

This thesis is the final part for obtaining a Master's degree of science at the University of Twente.

Supervisors:

Bas Borsje, Associate prof. University Twente (head graduation committee)

Jebbe van der werf, Associate prof. University Twente (supervisor)

Jos muller, PhD student University Twente (daily advisor)

Dimitris Dermenzoglou, PhD student Delft University of Technology (supervisor)

Institution:

University of Twente - Faculty of Engineering Technology

Department

Civil Engineering and Management (CEM)

Project duration:

April 2023 - December 2023

Cover image: Shoreline erosion of the tidal saltmarsh adjacent to Plum Island Sound (USA). (Fagherazzi, 2019)

Summary

The Netherlands has large coastal zones in Friesland, Groningen and Zeeland containing saltmarshes. These coastal wetlands are daily inundated by saltwater tides. They play a crucial role during storms when water levels are higher than the saltmarsh. Wave energy is dissipated as they travel over the saltmarsh, mitigating their impact on coastal dikes. Despite this wave damping effect, Dutch coastal protection standards do not account for saltmarshes due to a lack of conclusive evidence regarding the stability and effectiveness of saltmarshes.

The vegetation of a saltmarsh has a reinforcing effect on the local soil. Moreover, sediment is effectively trapped between the canopy, making it typically more elevated. The bare mudflat in front lacks this vegetation and is more susceptible to erosion, resulting in a distinct cliff. Numerous studies have observed the erosion trends, including cliff erosion and lateral retreat of saltmarshes along the Dutch coast, under various wave conditions. However, a comprehensive understanding of the hydrodynamics governing cliff erosion during storm conditions remains unclear. Therefore, further research is required to explore the hydrodynamics driving cliff erosion under extreme storm conditions. This study specifically aims to identify wave-induced near-bed velocities at a cliff, as a proxy for erosion under extreme storm conditions.

In order to gain insight into the wave-induced velocities during storm conditions, experiments were conducted in a wave flume. A 1:10 scaled model of a typical coastal saltmarsh transect was designed featuring a foreshore, cliff, saltmarsh, and dike. Particle Imaging Velocimetry (PIV) is used to measure velocity fields in a non-intrusive way. PIV, an imaging technique for measuring flow velocities, utilizes the motion of seeding particles in the water column to calculate speed and direction. In this setup, a thin LED light sheet was used to illuminate the particles, resulting in 20 2D (vertical and horizontal) velocity fields per second. Experiments have been conducted with differing wave heights, water depths and wave periods.

Analysing the obtained velocity fields shows diverse patterns surrounding a 12 cm saltmarsh cliff, including stokes drift, return flow, a vortex in front of the cliff, and a vortex on top of the saltmarsh. This study confirms the influence of wave characteristics on the vortex in front of the cliff, as found in previous research. Increasing the wave height or period creates a larger and stronger vortex in front of the cliff, although this effect seems to be absent when waves directly break at the cliff.

The vortex in front of the cliff causes high near-bed velocities on the mudflat directed towards the dike, and upward velocities on the cliff face. The saltmarsh platform immediately after the cliff edge is susceptible to the return flow and the vortex on top of the platform. On the salt marsh platform further towards the dike, there are high near-bed velocities towards the sea wall. These occur as the wave crest passes over this region.

The water depth, wave height and wave period parameters have been varied to assess their influence on the maximal near-bed velocity in the four areas described above. The wave period is found to be the most influential parameter, because it has the highest influence on the size of the vortex in front of the cliff. A more general relationship for the maximal near-bed velocities has been derived for three of the four locations, the offshore Ursell number. The Ursell number is a parameter that describes the non-linearity of waves based on the water depth, wave height and wave length (which is dependent on the wave period). If further research substantiates this positive linear relation between the Ursell number and the maximal near-bed velocity, the maximal near-bed velocities can be estimated with only measurements of offshore wave conditions.

Table of Contents

Table of Tables

Table of Figures

Preface

Presented before you is my Master's Thesis titled "Analysis of wave-induced velocity fields around a saltmarsh cliff: An experimental study on the application of Particle Imaging Velocimetry (PIV) in a complex hydrodynamic region." This thesis fulfils the final requirement for the completion of the Master's degree in Civil Engineering and Management at the University of Twente.

I wish to express my gratitude to my supervisors Bas Borsje, Jebbe van der Werf, Jos Muller, and Dimitris Dermenzoglou. Bas played a crucial role in connecting me to this thesis and providing the opportunity to delve into researching the effect and stability of a more nature-based coastal protection through collaboration in the Living Dikes project. During the scaled flume experiments, I spent two months in Delft, where I gained valuable insights into conducting experiments under controlled conditions, thanks to Jos, Dimitris, and another MSc student, Stijn Lakerveld. Working alongside them in the flume was not only enjoyable but also led to excellent data, a result of the critical perspectives provided by Jebbe and Wout Bakker (Deltares employee) concerning our PIV measurements. Their assistance, coupled with Jos's dedication to optimizing the PIV setup, contributed significantly to the success of data acquisition.

Lastly, I extend my appreciation to my friends and family for their support and joy throughout this thesis and the preceding phases of my academic journey. I hope you will find enjoyment in reading my thesis and that it will contribute value to the Living Dikes project.

Pieter Faber

Enschede, 14-12-2023

1. Introduction

Dikes stand as the primary defense against high water and flooding in the Netherlands. After the Watersnoodramp in 1953, in which the southern part of the Netherlands was flooded, the Delta programme was initiated to prevent future disasters (Rijkswaterstaat, 2023). The need to reinforce dikes arises from the combined challenges of rising sea levels and intensifying storms (DeltaProgramma, 2023; EEA, 2022). Traditional dike reinforcement schemes involves increasing their height and applying hard surfaces like revetment or asphalt. However, this approach comes with significant costs and has a finite lifespan.

Yet, a growing awareness underscores the potential advantages offered by natural coastal features, specifically saltmarshes, positioned in front of dikes. These areas present societal, economic, and environmental opportunities (Ecoshape, 2022; Nieboer, n.d.). Coastal regions are a popular location for recreation. Moreover, natural coasts serve functions that the world can benefit from amidst today's climate dilemmas. Plants growing on foreshores sequester substantial amounts of carbon, which can then be stored in the soil (Brodeur, 2022). In addition, saltmarshes contribute to reducing wave energy and are therefore considered a nature-based solution. Waves passing through or over vegetation, lose energy, lessening their impact on dikes (Arunakumar et al., 2019; Meijer, 2005; Van Veelen et al., 2021; Willemsen et al., 2020).

Despite the wave damping efficacy of saltmarshes along the Dutch coast, it is not integrated into the national coastal protection standards. The lack of conclusive evidence regarding the stability and effectiveness of saltmarshes prevents their inclusion in coastal safety calculations. If the added value of the saltmarshes were incorporated into flood protection standards, (future) reinforcements could be cancelled or a plan could be made to create more reliable saltmarsh areas to enhance flood safety.

The National Operational Management Programme for Water and Coastal Defences has initiated a research consortium, "The Living Dikes Programme," to address knowledge gaps in implementing saltmarshes for coastal defence (NWO, 2022). The consortium aims at quantifying the stability and effectiveness of vegetated foreshores in deltaic areas and delivering a strategy on implementing a Living Dike for future projects. Research for this objective consist of various methods, including storm impact evaluations on saltmarshes in the field, measurement campaigns within saltmarshes, numerical model development, and laboratory experiments to better understand saltmarsh dynamics.

This thesis is part of the laboratory experiments and focusses on observing near-cliff velocities induced by waves at the saltmarsh edge under varying wave conditions that represent extreme storms. This edge marks the transition from offshore mudflat to a vegetated cover, typically featuring an abrupt elevation change known as a cliff. These cliffs can grow in the order of 0.2 to 2.0m at the Dutch coast.

1.1. Background

Saltmarshes are a global ecosystem and can occur in both salt and fresh water environments (Figure 1-1). The vegetated foreshores dissipate storm-driven waves during extreme conditions, protecting the inland. Particularly in countries with limited financial resources, saltmarshes offer a cost-effective solution for primary coastal defence. Whether these saltmarshes will increase or decrease in height is dependent on the available sediment budget at a specific location (Fagherazzi et al., 2020). Lateral erosion could be compensated when there is enough sediment transported towards the saltmarsh. This accretion process has the potential to lead to increasing saltmarsh elevation, matching or even surpassing the local sea level rise. This adaptive capacity implies that the coastal protection system can effectively respond to the challenges posed by climate change.

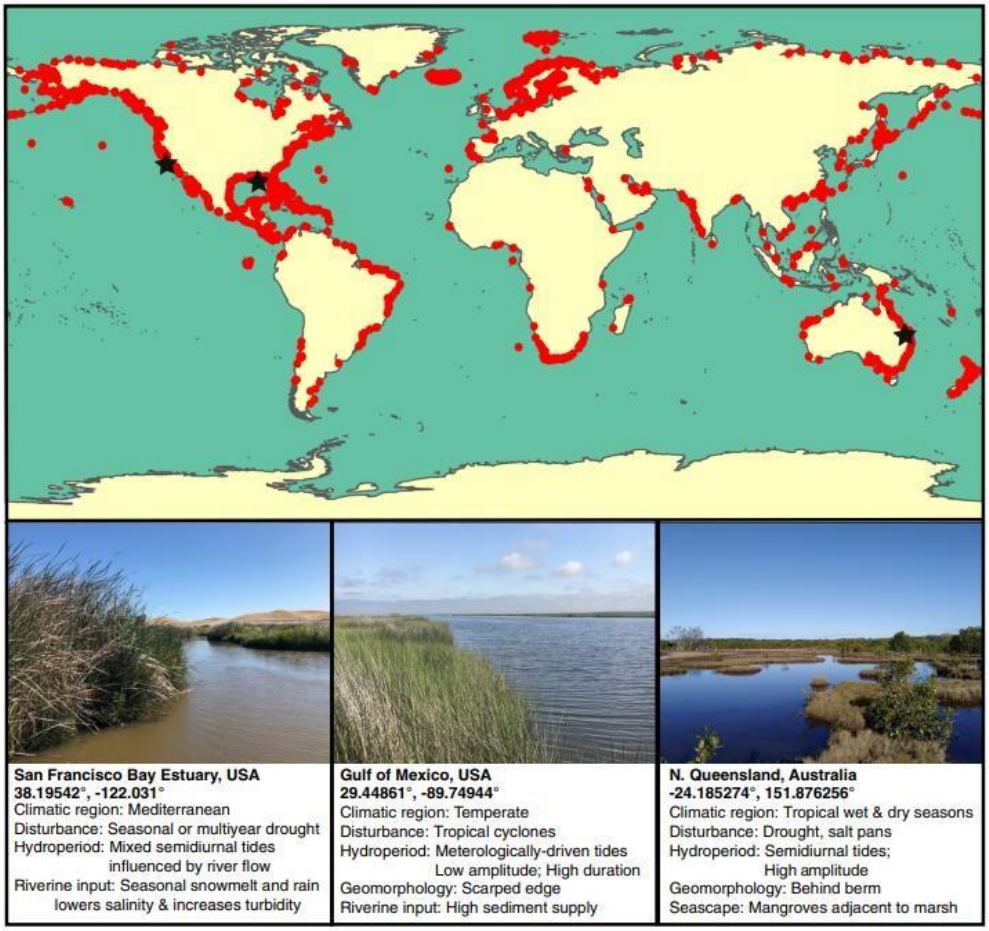

Figure 1-1, Global map of saltmarsh areas, with examples at the west coast of America, the east coast of America and the east coast of Australia (pictures going from left to right) (Ziegler et al., 2021).

The different climates in which these saltmarshes are located create their own dynamics. The vegetation type, the vegetation diversity, the soil type and the tidal range govern the saltmarsh characteristics. A classification is made for saltmarsh types based on how often the vegetation is submerged (Töpke, 2023). Saltmarshes that experience regular submersion give rise to their own ecosystem, where water transported onto the saltmarsh is drained through creeks when the sea level drops. Saltmarshes that are inundated only during extreme flood events mostly do not contain extensive creek networks, which is mostly the case in the Netherlands.

In the Dutch context, saltmarshes are situated along the most southern part of the North Sea coast in Zeeland and the northern coast at the Wadden Sea. While saltmarshes are already present in large sections of these coasts, human intervention offers the potential to create additional areas. Figure 1-2 shows an opportunity map for saltmarsh presence at the Wadden Sea coast in the northern part of the Netherlands. The map highlights that there are only small sections where a saltmarsh might not be applicable, with the majority of the coastal foreshore offering the potential to contribute to the coastal defence system as a saltmarsh. The driving processes of (lateral) saltmarsh erosion are still unclear, calling into question the stability, and therefore saltmarshes are not included in national flood safety calculations (Chen et al., 2023; Koppel et al., 2005).

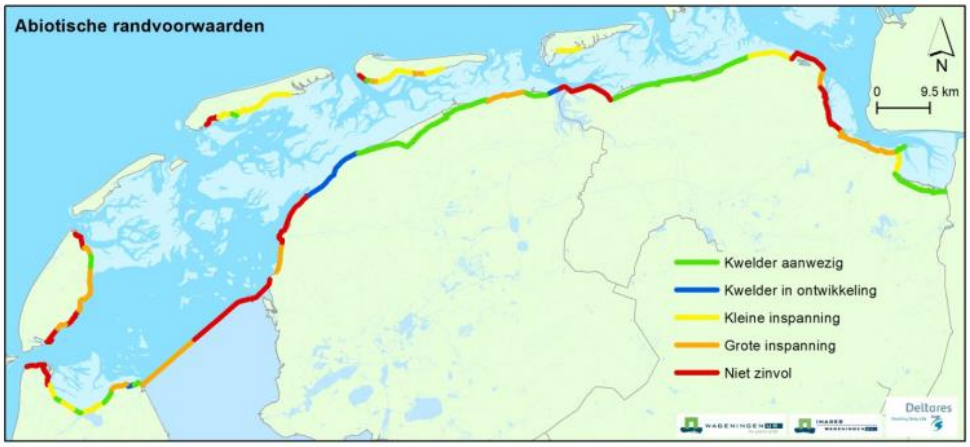

Figure 1-2, Saltmarsh opportunities along the Wadden Sea coast. In the coloured sections a saltmarsh is: present in green, in development in blue, not applicable in red, developable with low effort in yellow and with high effort in orange (van Loon-Steensma et al., 2012).

1.2. State of the art

There are numerous recent studies assessing wave attenuation over saltmarshes and their effects on coastal morphology. Arunakumar et al. (2019) showed how the vegetation height in comparison to the water depth is related to the wave attenuation over vegetation in a scaled setup with rigid vegetation, where Van Veelen et al. (2021) studied the effect of flexible vegetation. These studies show high wave energy reductions as long as the water level is not multiple magnitudes higher that the vegetation height. The principles used in their studies for the velocity profiles through vegetation are based on the emergent and aquatic flow behavior described by Nepf (1999, 2012).

The studies of Arunakumar et al. (2019) and Van Veelen et al. (2021) contain scaled flume setups in which the vegetation was not part of the coastal protection, but placed in a flume with and without a current in it. In a study for quantifying the wave attenuation at several locations in the Western Scheldt, Willemsen et al. (2020) found that the vegetated cover has the highest impact on wave attenuation over a saltmarsh. Their study concludes that the wave attenuation capacity under design conditions is much lower than actually measured with a vegetated saltmarsh.

The vegetation patches on a saltmarsh are almost always present on the transition from the mudflat onto the saltmarsh. The roots of these plants hold the ground together, while the soil on the mudflat can erode easier. A sudden elevation change, or cliff can be formed, from a significant erosion event washing out both the mudflat and the first offshore part of a saltmarsh (Koppel et al., 2005). This behaviour is also seen by Willemsen et al. (2018) who conducted measurements in the Western Scheldt on bed level change of the mudflat and the saltmarsh (Figure 1-3). Willemsen et al. concluded that the location of the saltmarsh edge is determined by the combined effects of bed level change and inundation time, which both control plant growth.

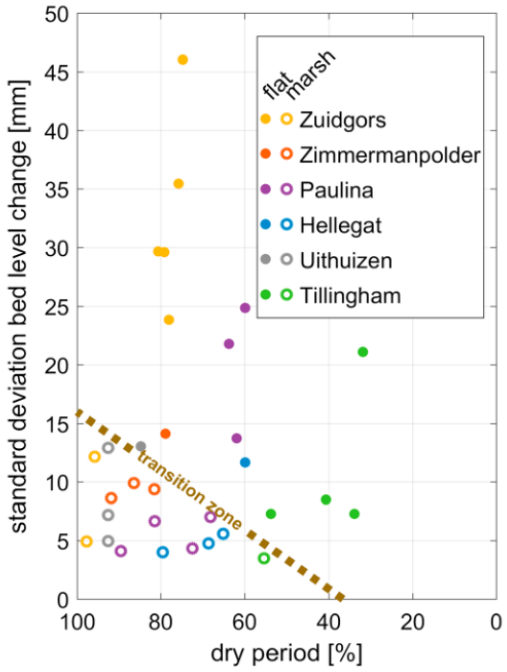

Figure 1-3, Mudflat and saltmarsh bed erosion in the Western Scheldt estuary, the Netherlands (Willemsen et al., 2018).

The findings of Willemsen et al. (2018) match the conclusions drawn in a study by Cao et al. (2021) into how different plant traits can influence the cliff height. In this study it was found that the Spartina Anglica has the highest potential for growing a cliff under various circumstances (Figure 1-4). This plant is common for the coast of the Netherlands, and therefore cliffs are likely to occur in Dutch saltmarshes. In a report about soil characteristics and vegetation on cliff erosion, Rahman (2015) states that the plants are the main contributors to reducing cliff erosion. He concludes that soil characteristics do influence the erodibility of a cliff, but that effect is insignificant compared to the influence of plants.

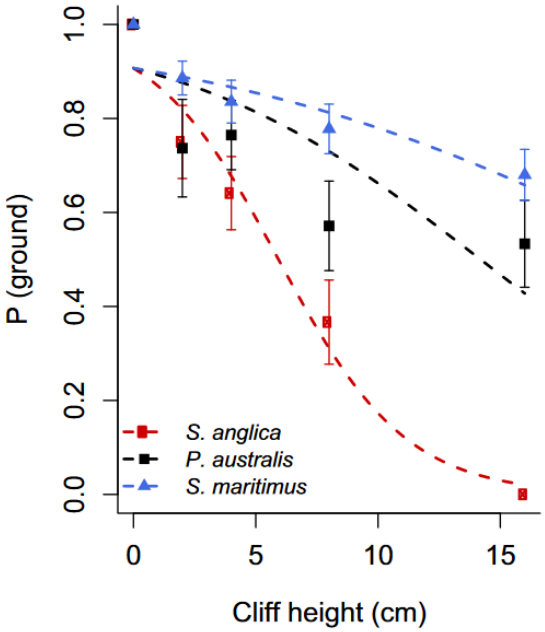

Figure 1-4, Cliff height with different vegetation expansion succession rates (P (ground)) for 3 different vegetation types (Cao et al., 2021).

Bendoni et al. (2016, 2021) and Francalanci et al. (2013) have extensively discussed the vulnerability of cliffs to erosion in intertidal areas, by executing both field measurements and flume studies to investigate the impact of soil and vegetation on cliff erosion. Their findings indicate that waves that travel over the saltmarsh do not significantly contribute to lateral saltmarsh erosion. Instead, both reports emphasize that lateral cliff erosion results from the direct wave impact on the cliff face, which is also observed by Tonelli et al. (2010). They identify two mass failure mechanisms for lateral retreat, illustrated in Figure 1-5. On the left there is lower level erosion underneath soil that is hold together with vegetation roots. When this gap becomes too large the vegetation patch hanging over the mudflat creates too much tension and can break from the rest. The erosion mechanism in the right figure is a block of sediment with a lack of cohesion in the soil toppling over due to wave-induced pressure differences. For intertidal processes these failure mechanisms can be main drivers, but the Dutch coast mainly consists of higher elevated saltmarshes that do not get inundated every tidal cycle (Van Loon-Steensma, 2015).

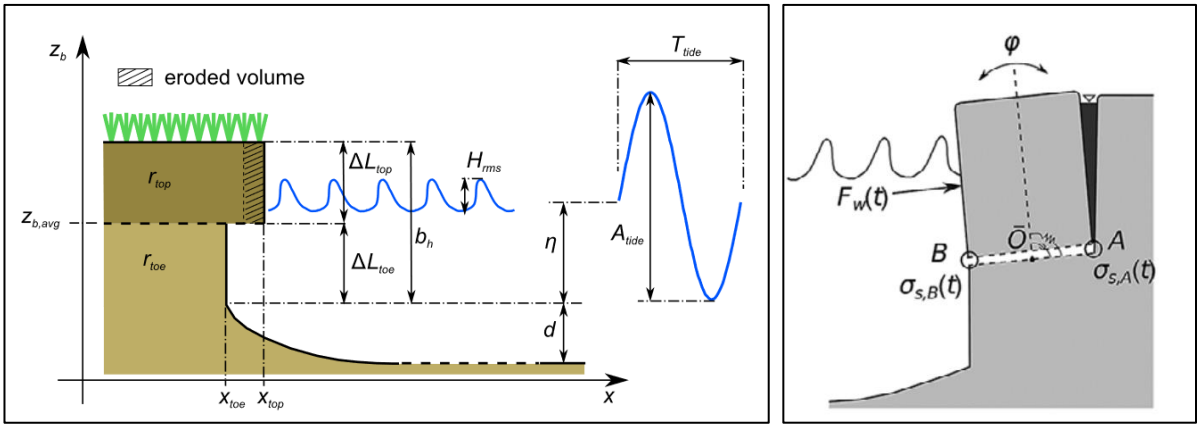

Figure 1-5, Mass cliff failure due to: lower level erodibility on the left, and toppling failure on the right (Bendoni et al., 2021; Francalanci et al., 2013).

In a study examining the relationship between lateral saltmarsh erosion and wave energy, Leonardi et al. (2016) claims a linear trend (Figure 1-6). While severe storms can result in sudden lateral retreats, their findings suggest that storms with higher frequency exert a more substantial influence on the overall lateral retreat. They state: “As wave energy increases, saltmarsh response to wind waves remains linear, and there is not a critical threshold in wave energy above which saltmarsh erosion drastically accelerates”. This linear relationship is reanalysed by Houttuijn Bloemendaal et al. (2023). They question the assumption that the unique characteristics of a saltmarsh do not impact the relationship between wave power and lateral erosion. In their specific case, they found an exponential growth of erosion with increasing wave power, suggesting that intense storms significantly affect lateral saltmarsh retreat. As climate change causes sea level rise and increased storm intensities, the significance of such extreme storm events is expected to grow.

In the Western Scheldt, a study conducted by Van Der Wal et al. (2023) focusses on lateral cliff retreat. Although mass failure events were identified, they did not contribute significantly to the total erosion. The lateral erosion was monitored with terrestrial laser scanners, and a pressure transducer measured wave and water level characteristics. The gradual erosion from high interval events were found most important for long term lateral cliff erosion. Lateral saltmarsh retreat is assumed to be affected by a differing water depth in their report due to hydrodynamic forcing on the bottom sediment. This creates a high interest in the near-bed velocities on the saltmarsh and cliff face under different conditions, with which the assumption can be assessed.

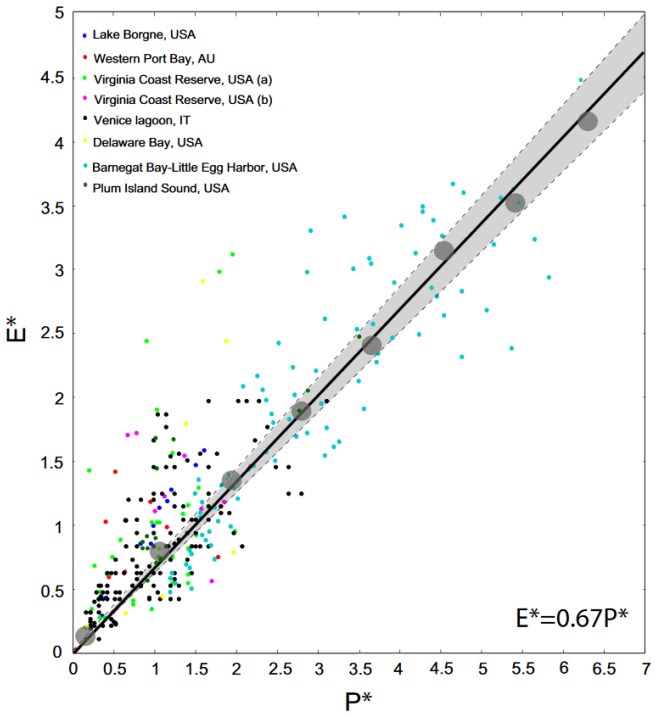

Figure 1-6, Linear relation between lateral saltmarsh erosion and wave power. The dimensionless erosion (E/Eavg), during all different storm types at 8 locations, plotted against the dimensionless wave power (P/Pavg) (Leonardi et al., 2016).

Suzuki & Klaassen (2011) looked into the effect of hydrodynamics around a cliff in the context of seedling establishment. In this study both wave flume experiments and a numerical model were used. In the flume the Particle Tracking Velocimetry (PTV) method is used, where balls are tracked by taking 2 consecutive pictures of the water column to derive the path travelled by the balls, resulting in a velocity vector at the ball locations . There is also the Particle Image Velocimetry (PIV) method, in which much more balls (particles) are used to create a velocity field with a higher resolution. With PIV the balls are not tracked, but the particle displacement in a small area is determined. During the generated waves, the occurrence of a vortex in front of the cliff is qualitatively reported for both the flume and the numerical model results (Figure 1-7). Plants in front of the cliff are found to be negatively affected by this vortex, and the report states that the vortex grows stronger with increasing wave height and period.

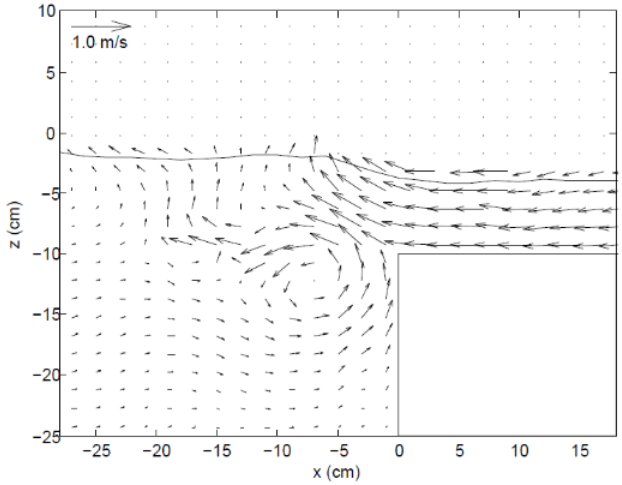

Figure 1-7, A vortex in front of a cliff derived in a numerical model (Suzuki & Klaassen, 2011).

1.3. Problem description and knowledge gap

While there has been extensive research on the general relationships for different wave conditions, soil types and vegetation on saltmarsh erosion, the specific hydrodynamics responsible for lateral saltmarsh retreat during extreme storm conditions remain largely unexplored.

Cliff erosion, or lateral saltmarsh erosion, has been studied by various scientists, but the actual mechanics driving cliff erosion is not clear yet. One study shows how the cliff retreats gradually with less extreme events, while others show that the episodic retreats and weakening of the cliff during storms are the main drivers (Houttuijn Bloemendaal et al., 2023; Leonardi et al., 2016; Van Der Wal et al., 2023). For the saltmarshes to be included into the Dutch coastal protection guidelines, there must be more consensus in this field of research. When an excessive storm would erode a large part of the saltmarsh, the wave attenuating function is significantly reduced, and the contribution to flood safety is lost. At that case, whole sections of coastal dikes would immediately be at risk for future extreme events.

There is limited knowledge about the hydrodynamics that drive lateral saltmarsh retreat. The study of Suzuki & Klaassen (2011) showed possible locations that could be vulnerable during storm conditions due to a vortex in front of the cliff. However, the actual velocities that occur during storm conditions, and the most sensitive parameters that drive these velocities are not quantified. The PTV measurements they conducted lack temporal resolution and the numerical model that was used in their study lacks spatial resolution. Further research is needed to explore the hydrodynamics that force cliff erosion during extreme storm conditions. Therefore we propose an intrusive measurement method with which a higher spatial and temporal resolution can be achieved: PIV. If this measurement method can measure velocity fields accurately, it can assess the near-bed velocities around the cliff to assess the hydrodynamic forcing on the bottom sediment (Van Der Wal et al., 2023).

1.4. Research objective and questions

For this study the following objective is defined: To understand and quantify the near-bed wave-induced velocities as a proxy for cliff erosion of a coastal saltmarsh, using 2D PIV. The objective of this study has four components. First, the use of 2D Particle Imaging Velocimetry (PIV) is assessed on its applicability for capturing wave-induced near-cliff velocity fields with a spatial resolution higher than Suzuki & Klaassen (2011). The second goal of this research is to compare the PIV measurements in the near cliff region to other measurement techniques to validate the accuracy of the PIV velocity fields. The third goal is to find the near-cliff hydrodynamics that contain high near-bed velocities during extreme storm conditions. And the last goal is to assess the sensitivity of differing wave characteristics on peak near-bed velocities. In order to reach these objectives the research questions (RQ) are formulated as follows:

RQ1 **What are the requirements to carry out 2D PIV measurements in a complex hydrodynamic region of a saltmarsh cliff?**

RQ2 **How well can PIV measure velocities in a complex region of a saltmarsh cliff compared to other measuring techniques in terms of accuracy.**

RQ3 **What wave-induced near-bed velocities patterns are critical for erosion of a saltmarsh cliff during storm conditions?**

RQ4 **what is the effect of differing wave characteristics on the peak near-bed velocities that drive erosion?**

1.5. Thesis outline

This thesis is structured starting by explaining the methodology used for answering the questions above in chapter 2. This chapter consists of a description of the experimental setup, featuring a scaled coastal transect within a flume, and the experiments that are conducted in it. The transformation process of the gathered PIV-images into velocity fields is explained, and the requirements for PIV to function effectively are presented. Subsequently, an analysis of the accuracy of the velocity fields is presented, involving a comparison with an alternative measurement technique. Lastly the methods used for near-bed velocity analysis are explained.

The results in chapter 3 present whether this experimental setup meets the PIV requirements, how well this PIV setup compares to another measurement technique, which velocity field patterns create high near-bed velocities and the influence of different wave characteristics on the peak near-bed velocities.

In Chapter 4, these findings are discussed together with how they fit the existing knowledge base. Chapter 5 wraps things up with our conclusions, where the research questions are answered. Finally, in Chapter 6, recommendations are made for further research.

2. Materials and methods

This section outlines the methods used to address the research questions. The presented data are collected through a series of wave flume experiments. The materials and steps to answer the research questions are visualized in a flow diagram (Figure 2-1). In the first section of this chapter, an overview of the scale model is given, followed by a description of the PIV materials used and the experiments that are conducted. Then the requirements for a PIV setup are presented, which will be used to answer RQ 1. The methods for data processing, including calibration, calculation of velocity vectors and post-processing, are then explained. After that, the PIV validation is explained, which is used for RQ 2. Finally methods that are used for the velocity field analysis are presented. Those velocity fields are used to find high near-bed velocities and the effect of differing wave characteristics on the near-bed velocities (RQ 3 and 4).

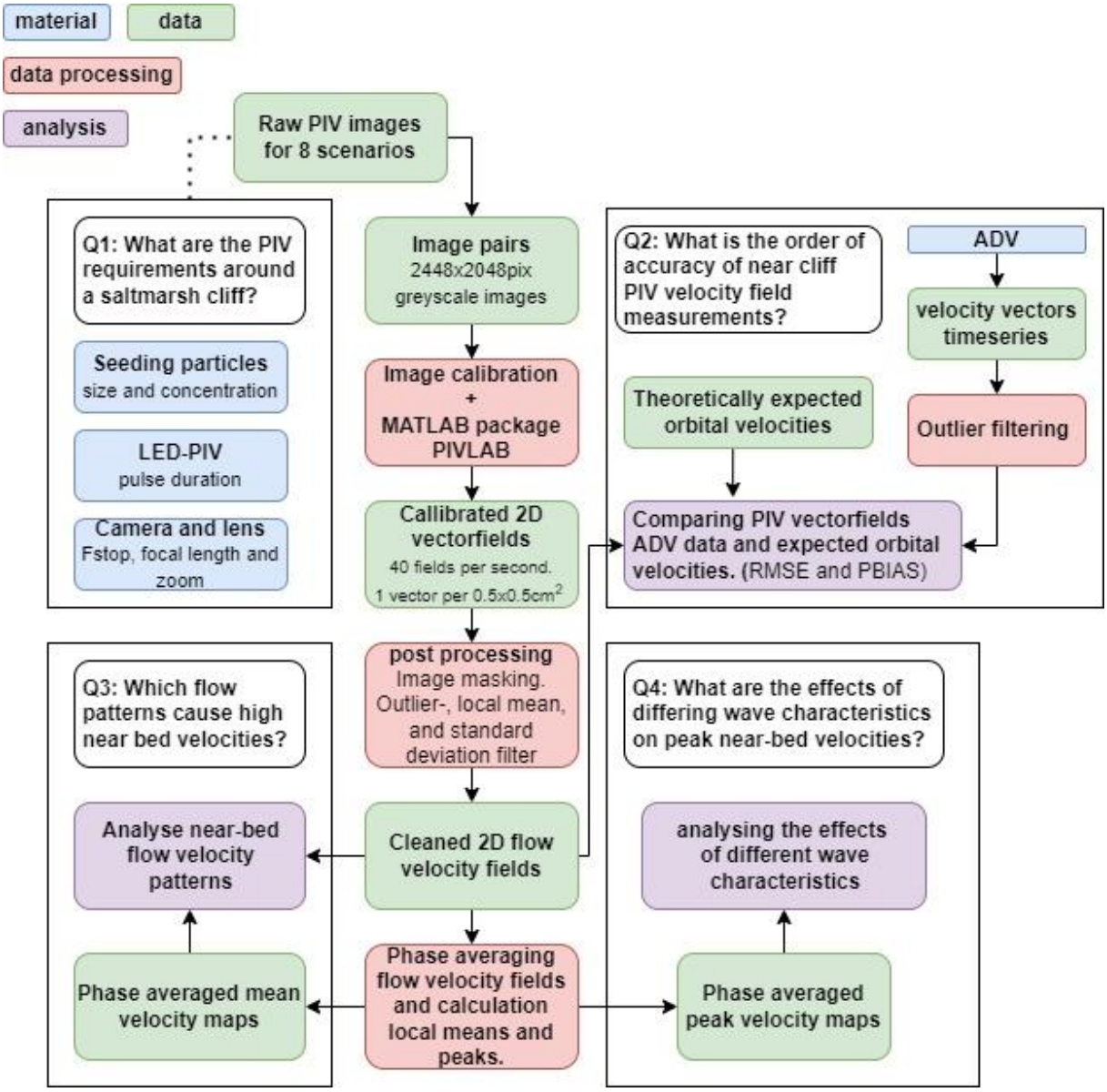

Figure 2-1, Flow diagram of the materials data and methods used to answer the research questions.

2.1. Flume experiments

For this research, a series of wave flume experiments are carried out to capture wave-induced velocity fields during various wave conditions around the saltmarsh cliff. Particle Imaging Velocimetry (PIV) is used to obtain full 2D flow velocity fields near the saltmarsh cliff.

The flume is situated at Hydraulic Engineering Lab at the Delft University of Technology and is 40 m long, 80 cm wide and about 1 m high. The setup mimics a coastal transect with a foreshore, saltmarsh and dike on a 1:10 scale according to Froude similitude, which can be used for when surface friction effects are neglectable (Taveira Pinto, 2020)(Figure 2-2). With Froude similitude the real world velocities are assumed to be proportional to the root of the model scale, as shown in the equations below. In the formula *Fr* is the Froude number *V* is the velocity and *L* the length scale.

$$Fr_{real} = \frac{V_{real}}{\sqrt{g * L_{real}}} = \frac{V_{model}}{\sqrt{g * L_{model}}} = Fr_{model}$$
$$V_{real} = V_{model} * \sqrt{\frac{L_{real}}{L_{model}}} \quad (1)$$

On the back of the flume a piston-type wave maker is present that can generate multiple hydrodynamic wave conditions. A 15 m long section of flat bottom, representing offshore deep water is followed by a sloped section, representing a mudflat. The first part of the mudflat has a 1:9 slope and followed by a 1:45 slope. The 1:9 slope is a transitional slope implemented to save length in the flume and construction materials while maintaining most of smooth shoaling. The total slope ends at a height of 24 cm higher than the offshore.

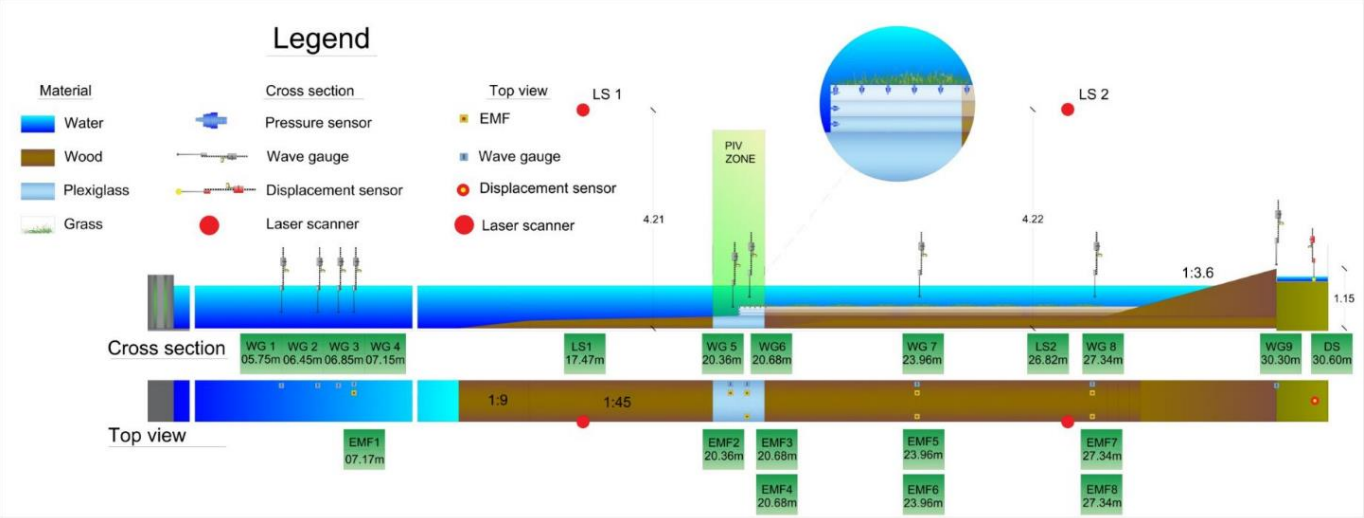

Figure 2-2, Schematic flume representation. A cross section is shown at the top and a top view is provided in the bottom. The legend shows the different measurement tools used. The circle is a zoomed in section of the cliff. The 3 different horizontal lines represent the different elevations that are possible in this setup.

Starting at 20.5 metres from the wave generator, there is a 7 m long level saltmarsh which ends at a dike section sloped at a 1:3.6 gradient. The saltmarsh setup can be interchanged between two states; either smooth wooden panels that represent a saltmarsh platform absent of vegetation, or panels filled with rubber cylinders (Figure 2-3), which mimic coastal vegetation found along saltmarsh coasts in the Netherlands. These elastic cylinders are scaled according to Cauchy similitude are modelled after fully grown *Spartina Alterniflora*. The scaling procedure was outside the scope of this thesis and was

prepared by an involved PhD students. As previously mentioned, a cliff can be observed at the edge of the saltmarsh. This cliff is formed by raising the saltmarsh platform. Figure 2-2 shows the three distinct saltmarsh elevations: one at 0cm elevation resulting in a continuous foreshore mudflat transect, and two cliff elevations at 6cm and 12cm. These three elevations, with and without vegetation coverage, lead to a total of six different experimental setups.

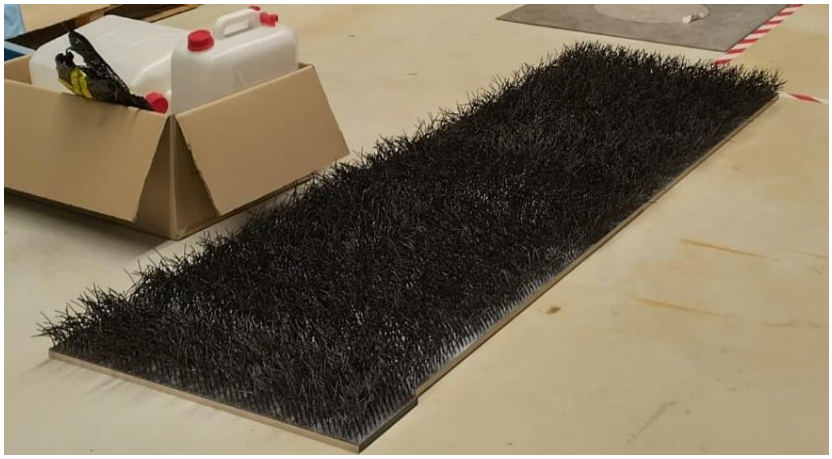

Figure 2-3, Scaled vegetation panels

Our experiments aim to investigate the influence of varying wave characteristics on the hydrodynamic processes that force cliff erosion during extreme storm conditions. During these experiments the cliff height is 12 cm and no vegetation is present on the saltmarsh, with which the hydrodynamics of solely a cliff is observed. Table 1 displays the performed experiments with their corresponding characteristics. The experiments are designed based on the M07 base case experiment, to investigate the impact of changing a single parameter. Therefore every experiment differs on either the water depth, offshore wave height, or the wave period. In every experiment 10 waves are recorded, Therefore the experiment duration is 10 times the wave period.

Table 1, Experiments conducted to analyse the effect of differing wave characteristics in a non-vegetated 12 cm cliff setup. Experiment M01 is marked red as it can not be used for PIV due to air bubbles (which is explained in section 3.1.1.3).

Experiment reference code	Water depth on the saltmarsh (m)	Offshore wave height (m)	Wave period (s)	$Experiment\ duration\ (s)$
M01	0.04	0.10	1.5	15
M02	0.09	0.05	1.5	15
M03	0.09	0.15	1.5	15
M04	0.09	0.10	1.2	12
M05	0.09	0.10	2.0	20
M06	0.09	0.10	2.5	25
M07	0.09	0.10	1.5	15
M08	0.19	0.10	1.5	15

2.2. PIV setup

In this research, Particle imaging velocimetry (PIV) is used to capture wave-induced velocity fields around the saltmarsh cliff. Velocity fields in the flume are captured non-intrusively in a 2D plane from the side of the flume, which corresponds to the vertical and horizontal direction of the flume. Variation in the velocity profile in the width of the flume is of minor interest in this flume experiment, as the velocities and gradients are expected to be small.

PIV is an imaging method that utilizes tracer particles. By calculating the displacement of these particles, a vector field representing velocity is obtained. Appendix A contains a detailed explanation for extracting velocity vectors from PIV images. The imaging process takes place in a darkroom, in which the particles are illuminated by a light source (Figure 2-4). The tent is constructed of black cloth over a wooden frame. Figure 2-5b shows a schematized version of the PIV setup and highlights the plane where velocity fields are measured (Area of Interest (AoI)). At this location, a LED light source illuminates only a very narrow part of the water column (Figure 2-6). The light sheet can pass the bottom of the flume through a transparent, plexiglass-strip in the middle of the flume.

Figure 2-4, dark room tent placed over the wave flume for blocking light from the PIV measurement area.

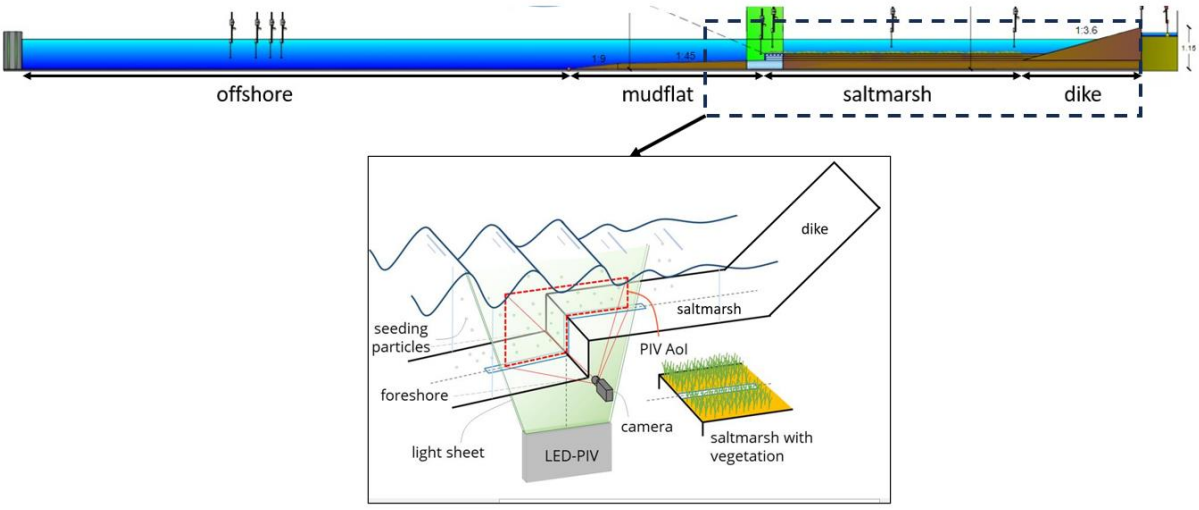

Figure 2-5, Dashed squared section in the full flume in the top (a); PIV Area of Interest (AoI) highlighted in this section in the bottom (b);

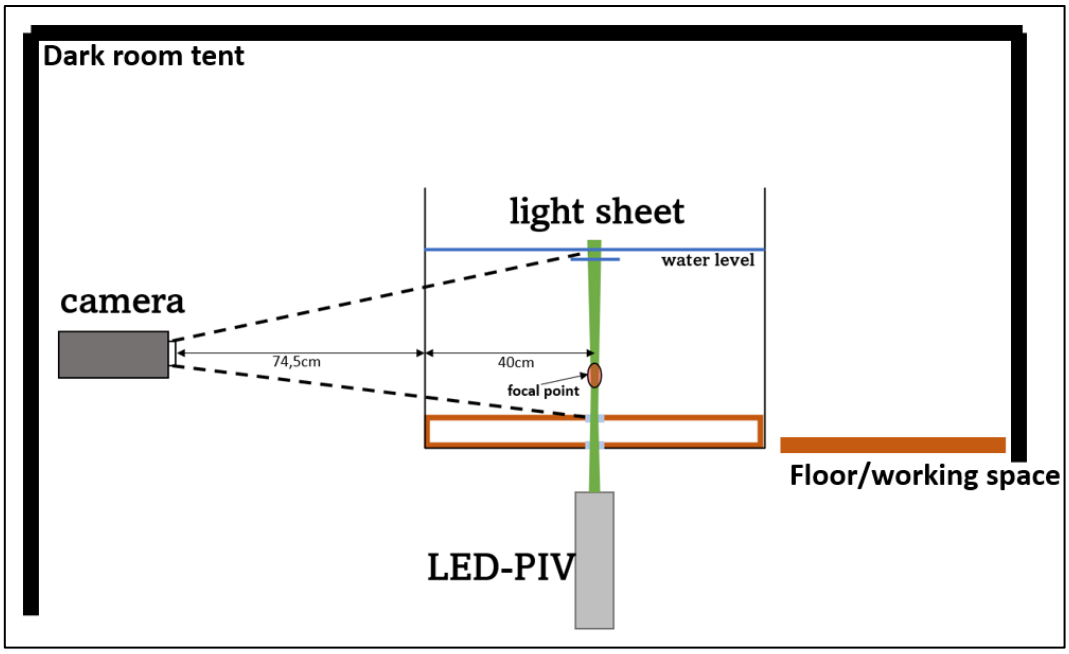

Figure 2-6, Cross sectional schematization of the full PIV setup, including the camera distance to the light sheet and its focal point, the dark room tent covering the setup and the working space on the side of the flume in the tent.

As a light source, the so-called LED-PIV is used, which is in-house developed at Delft University of Technology (Bakker et al.) The LED-PIV is located beneath the flume at a distance where the light sheet width converges and forms a focal point approximately 20 cm away from the mudflat floor. When the light sheet diverges , the intensity decreases, resulting in less illumination of particles. The sheet of light passes through a plexiglass floor of the model, calm water, and a plexiglass cover from the mudflat/saltmarsh. Because of the complex refraction of entering and leaving different materials and substances, the focal point was manually checked. Figure 2-7 displays the initial measurements executed outside the flume that are validated inside the flume.

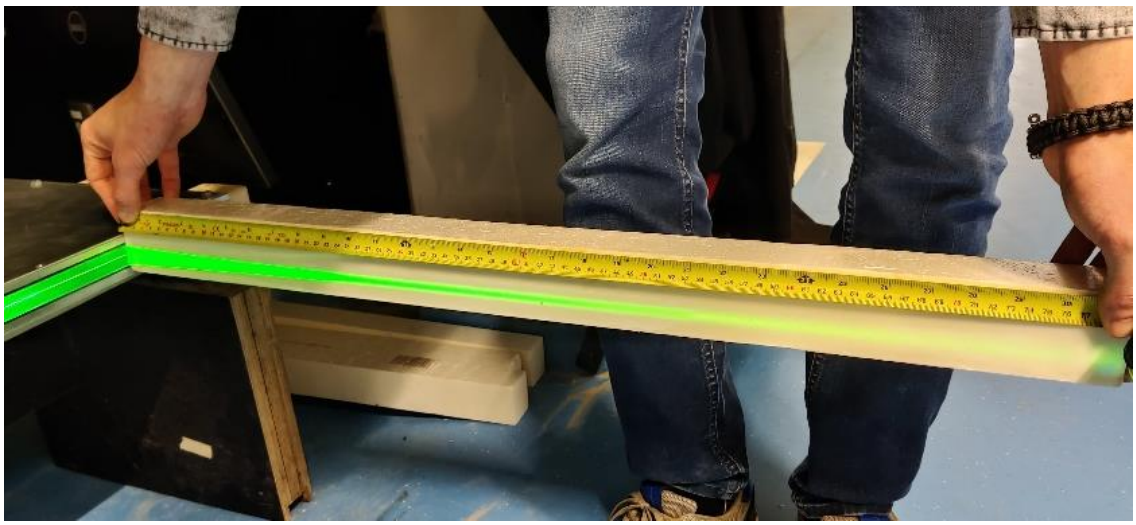

Figure 2-7, Light sheet convergence of the LED-PIV

The Oryx ORX-10G-51S5M-C camera is used with a 12.5 mm focal length Television lens and a f/stop of 5.6. Positioned perpendicularly to the light sheet, the camera is situated 115.75 cm away from its centre, capturing a span of 40 cm of water, 1 cm of glass of the flume wall, and 74.75 cm of air towards the camera's aperture (Figure 2-6). The resulting area of view of the camera is 50 cm high and 60 cm

wide. The acquired images possess a resolution of 2048x2448 pixels and are configured to record at 40 frames per second. The timing for LED-PIV activation is set to create image pairs with a 4200 µs interval between the first and second frame illuminations (explained in detail in Appendix A). This parameter is determined based on expected maximal orbital velocities.

The seeding particles in the water are small polyamide spheres with a diameter of 100 µm (Vestosint (Evonik, 2022)). The density of these particles is just lower than fresh water, having an insignificant effect on the particles following the flow. The particles are added to the water in and around the area of interest. The particle concentration in the water column depends on the spatial resolution of the vector fields extracted.

2.3. Design rules-of-thumb for PIV experiments (RQ 1)

In order for PIV vector calculations to function effectively, certain requirements must be fulfilled, which will be outlined in this section.

The first requirement is that a seeding particles must be clearly captured in the image. To provide a technical definition, a single particle must be larger than one pixel on the camera chip to be accurately distinguished by the computer software. The size of one particle in the image is determined by the distance between the camera and light sheet, the diffraction caused by light breaking of water, and the camera settings. For the PIV software to work appropriately, the particle diameter should be larger than the distance between 2 pixel centres in the image.

$$d_{particle\ in\ image} > d_{pixel} \tag{2}$$

The time interval between the first and second frame of a frame pair, along with the size of the interrogation window, determines the velocities that can be captured and must be appropriately scaled relative to each other. This calculation area is commonly known as an "interrogation window", typically defined in pixel dimensions, such as 32x32 pixels. In the second frame, this window is enlarged to twice its height and width to search for the highest cross-correlation. Figure 2-8 shows the visualisation of this interrogation window with the red boxed area in the first image (at $t = t_0$) . The yellow box in the second image (at $t = t_0 + \Delta t$) is the search area for the highest cross-correlation. The area inside the blue square has the highest cross-correlation with the red boxed area of the first image, which is why the resulting vector points to the left up (Furter information on the cross-correlation and defining a flow vector, see Appendix A). The maximal particle displacement can be predicted and should not exceed half an interrogation window during the time between the two frames, because a particle from within the red box could travel outside the yellow box. The timestep at which this would happen will be approached by calculating maximal orbital velocities (van der Werf, 2021).

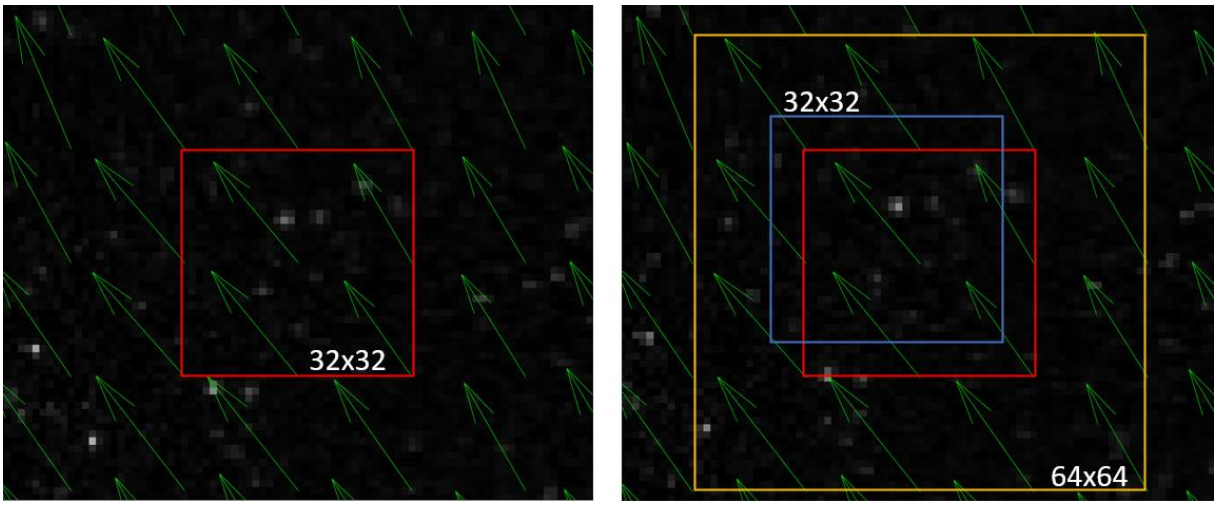

Figure 2-8, An example of a resulting vector. The blue square in the right image has the highest correlation with the red area in the left image.

A third criterion evaluates the interrogation window size by analysing a histogram of sub-pixel displacement. Kislaya (2016) presented how an insufficient interrogation window size can bias the resulting vectors to integer values of pixel displacement. This means that the images have inadequate resolution for this interrogation window size. The PIV software can not distinguish sub-pixel displacement of the tracer particles, and is therefore biased towards integer values of pixel displacement. Figure 2-9 illustrates an example of this tendency, where the peaks are clearly visible around the integer values, and this phenomena is known as peak locking.

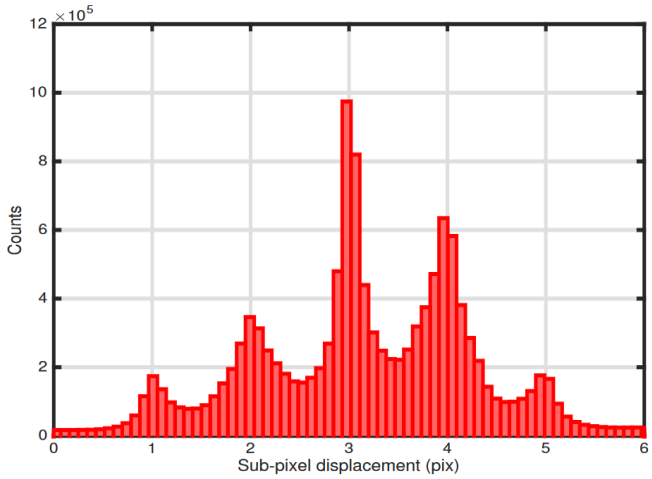

Figure 2-9, Example of Peak locking, where particles show a tendency to travel a distance equal to a round number of pixels (Kislaya, 2016)

The next criterion is that cross-correlation fields require an appropriate number of particles in each interrogation window to maintain accuracy. The ideal average value is around 10 particles per interrogation window for reliable results (Raffel et al., 2007). Having too few particles, e.g. fewer than 4, leads to a high signal-to-noise ratio. Also, having more than 25 particles per interrogation window can result in numerous directions showing a correlation peak. This occurs because the interrogation window becomes saturated with particles, increasing the likelihood of accidental similarities between the first and second interrogation areas.

Another critical consideration for achieving precise and effective PIV is the necessity of obtaining clear images. Presence of debris, litter, or air bubbles in the water that deviate from the flow pattern can introduce false displacements during PIV measurements. Additionally, light interference can make it challenging to distinguish particles. The water is closely monitored during the tests, ensuring the absence of contamination in the area of interest and a bubble-free water column. A preliminary examination of the images before the evaluation of the resulted vector fields of an experiment is crucial to exclude false velocity patterns.

2.4. Data processing

2.4.1. PIV velocity fields

The images are recorded in 16 bit grey-scale, resulting in 2448x2048 pixels with grey-scale values up to 65536 (16bits)(Figure 2-10). The camera needs to change position in between the experiments to record the full water column. When the water level is high, the camera needs to be in the middle of the water column. If the water level is low, the camera must be placed lower, otherwise it will record the water surface instead of the water column.

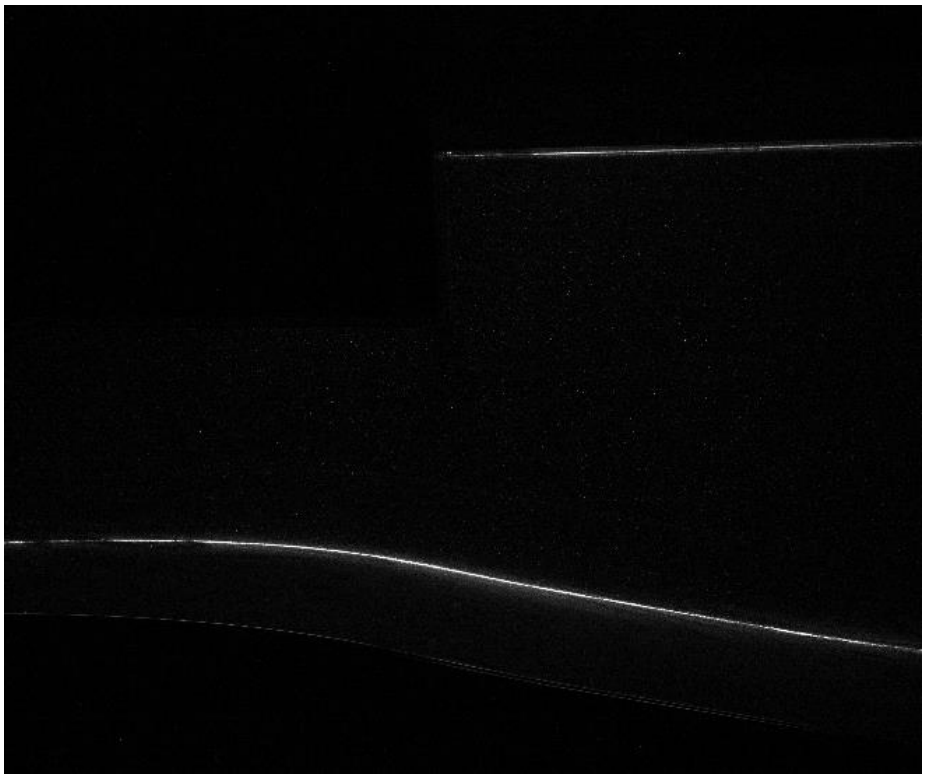

Figure 2-10, Raw image data example for a setup with a 12cm cliff. The image is upside down, so the waterline is the white layer in the bottom and the flume floor is at the top of the image.

2.4.1.1. Camera calibration

The images need to be calibrated before they can be used to calculate real world velocities. The images are calibrated both intrinsically and extrinsically. The intrinsic calibration corrects for distortions of the raw image due to the lens itself and internal miss-alignment of the lens and camera chip. The extrinsic calibration is used to transform the images to orthogonal *x-y* coordinates for every new camera setup. This is done by making a reference image of a checkerboard, that is placed exactly in the middle of the light sheet and in correct focus for the camera (COGNEX, 2020; University College London, 2019) (Figure 2-11). The calibration process was performed by the involved PhD student.

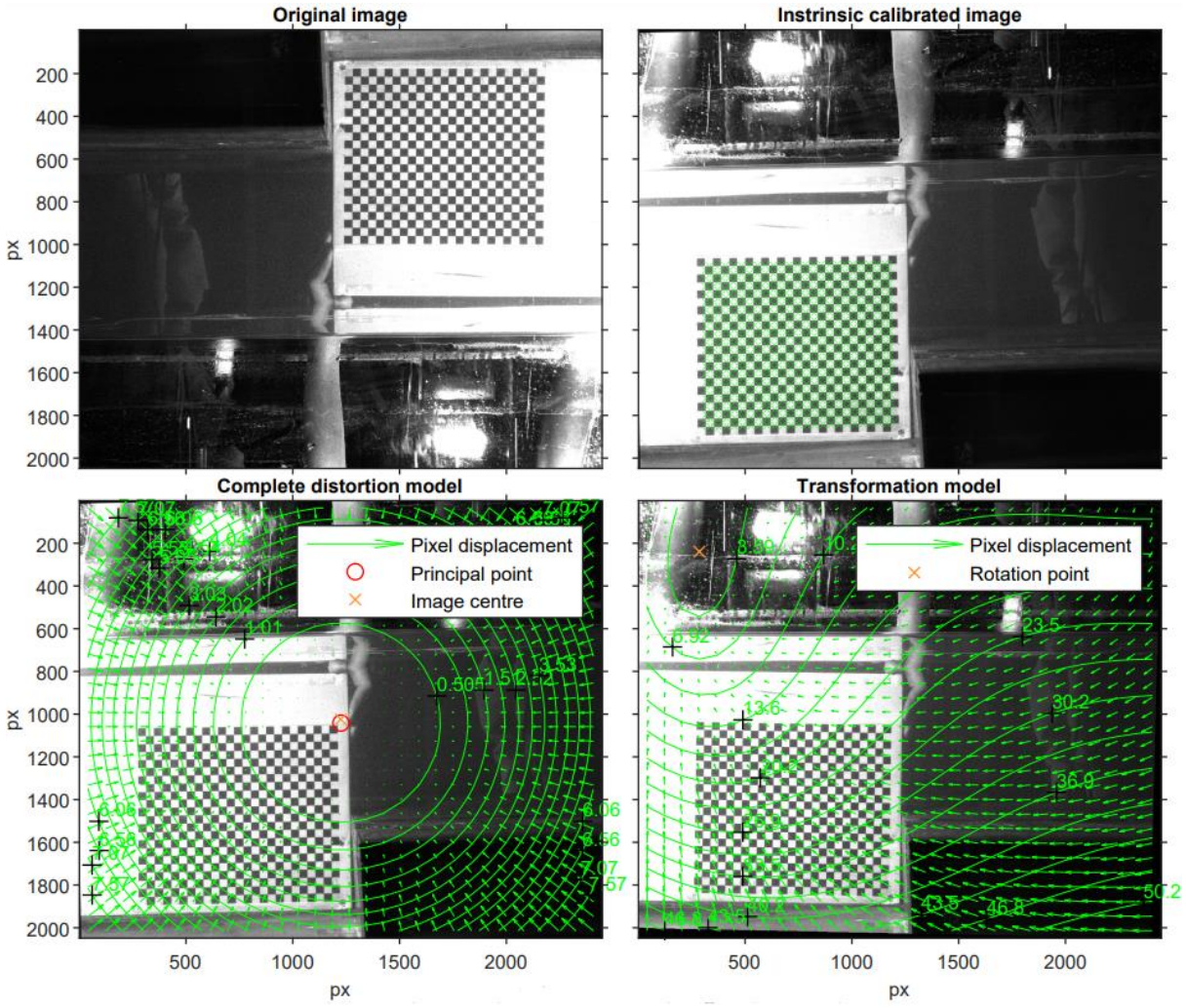

Figure 2-11, Raw image calibration. On the right top the intrinsic calibration is applied and the image is flipped, in the bottom left the checkerboard is orthogonalized and the last picture shows a rotational transformation to get the coordinate directions for the x and z direction in the image equal to the real world. These transformations are then saved and applied to all the PIV images taken with this setup (Muller, 2023).

2.4.1.2. PIV calculations

To perform pairwise image cross-correlation and post-processing the calculated velocity vectors, the MATLab PIV processing toolbox, PIVLab, was used (Thielicke, 2023). This toolbox contains the necessary scripts to perform the cross-correlation for all image couples, explained in the PIV explanation section. Figure 2-12 shows a resulting vector field at one moment in time. The mudflat on the left and the saltmarsh starting with a 12 cm cliff at the right are marked black because there is no water in those regions. The top of the figures show no clear pattern in velocity vectors as this part is above the water and no tracer particles are present. The interrogation window size is 32x32 pixels, which equals 0.86x0.86 cm^2. Moreover, each interrogation window is cross-correlated with a 50% overlap to produce 127x152 *u* and *w* velocity components for each image pair.

The resulting vector fields are filtered on outliers with a standard deviation filter and local median filter. The standard deviation filter assesses whether all vectors have a reasonable magnitude. This is achieved by generating a distribution of all vectors in the vector field and identifying vectors that deviate more than 5 times the standard deviation from the mean as outliers. The local median filter focuses on the local velocity pattern, ensuring that the vector under consideration does not deviate too much from the surrounding vectors. For each vector, the median of the eight surrounding vectors

is determined. If the displacement of any vector component deviates by more than 2 pixels from the median, that vector is marked as an outlier. When a vector is identified as an outlier, the missing value is replaced using a 'spring method'. In this method, the vector is determined through interpolation between the vectors on opposite sides, including above and below, left and right, and the two diagonal lines. The interpolated values are then averaged to ensure that all neighbours contribute to the outlier's replacement.

Cameron (2022) explains in his report how minimal errors in the resulting vector fields can be when the conditions are perfect. However some parameters such as the seeding concentration can vary because it is added by hand in our experiments. The glass we filmed through is also not perfectly transparent due to some scratches, so incidental inconsistencies in the velocity fields are expected to occur. Bakker et al. (2021) tested the LED-PIV, which is used in this study as well, for an 0.7x0.7 m^2 area where flow velocities up to 1 m/s are recorded. They reported on small vector underestimations when the vectors are located against object surfaces. The scale of their study is highly comparable with the scale of this study. With a 64x64 pixels interrogation window, 5% of the velocity vectors are marked as outliers in Bakker et el.'s analysis. This is therefore also expected to happen with the vectors measured in our experiments.

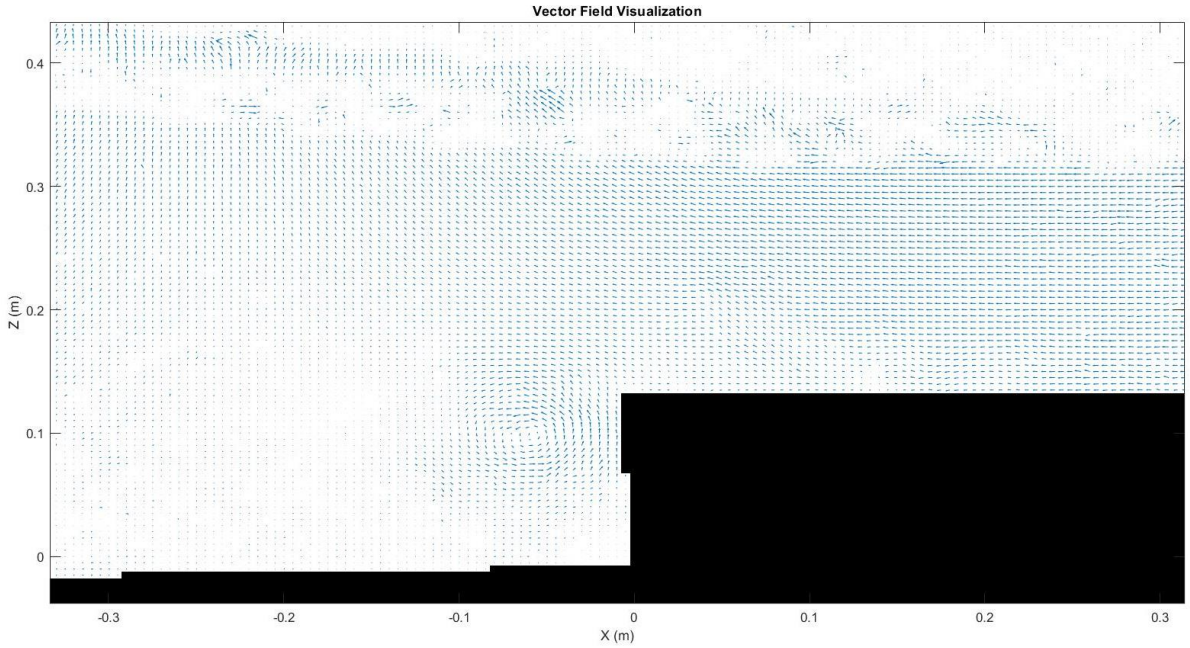

Figure 2-12, A PIV vector field in a setup with a 12 cm cliff (the mudflat and saltmarsh are marked black).

2.4.1.3. Errors in image saving

During the experiments, it turned out the image capturing software for PIV was not able to store the incoming images at the requested framerate. On averages, 6 per 100 frames are missing. Since PIV requires two consecutive images at a precise timestep, when one image is missing, the corresponding flow velocity field for that time step is not correct. As such, these instances were manually identified, deleted from the timeseries and linear interpolation is applied to estimate the missing data.

2.4.2. ADV measurements

For validation purposes, point velocity measurements are gathered with an Acoustic Doppler Velocimeter (ADV) (fixed head, point measurement Vectrino (NORTEK, 2023)). The device measures the flow velocity in the x, y and z direction. During deployment, the instrument was positioned parallel

to the flume wall, making the mean velocity in the y-plane negligible. The left part of Figure 2-13 shows the raw data from an experiment with no cliff or vegetation where a constant wave travels over the saltmarsh. The ADV records data at 5-millisecond intervals, capturing mean wave orbital velocities and small-scale turbulence.

The ADV measures 5 cm below the transducer, in a cylindrical volume of 5 mm high with a diameter of 6 mm. It has an accuracy of ±0.5% of the measured value added with ±1 mm/s. So a velocity of 1 m/s is measured in the range: 0.994 and 1.006 m/s.

The raw data shows spiked signals, indicating false measurements, which are subsequently filtered out. Spikes in the ADV data are identified by comparing the raw data to the moving average, and the data points associated with spikes are replaced with the corresponding moving average values. To validate the PIV results, the ADV data is smoothed get rid of turbulent fluctuations. Smoothing is achieved by eliminating high-order frequencies through a low-band frequency filter. The resulting time series is presented in the right part of Figure 2-13.

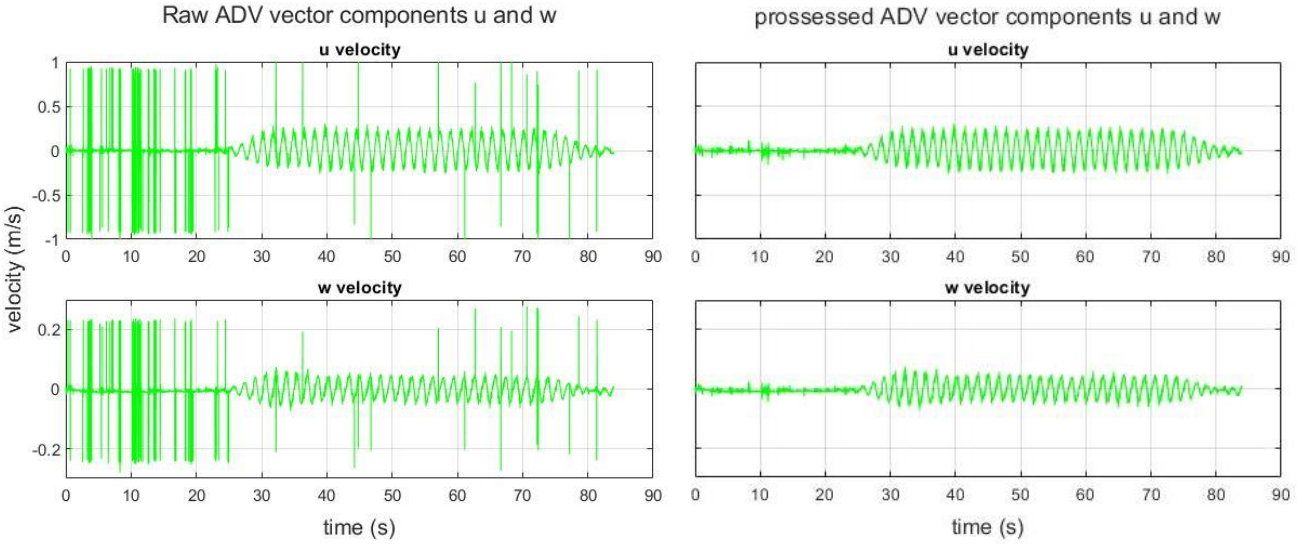

Figure 2-13, Raw and processed ADV data plotted over time.

2.5. PIV validation (RQ 2)

To validate the PIV measurements, ADV measurements and analytical approximations are used as comparisons. For the comparisons, a setup with and without a cliff are used, to validate the PIV for smooth orbital velocities, when no cliff is present, as well as the less understood complex hydrodynamics around the cliff.

The validation with no cliff is done at 12 different locations (Figure 2-14). The offshore wave conditions for the validation with no cliff are: a wave height of 0.10 m and a wave period of 1.6 s at a water depth of 0.7 m. In the validation locations ADV measurements are executed and are compared with the extracted PIV velocities at those locations. As the vectors are 2-dimensional and compared over time, they will be separated into *u* and *w* components.

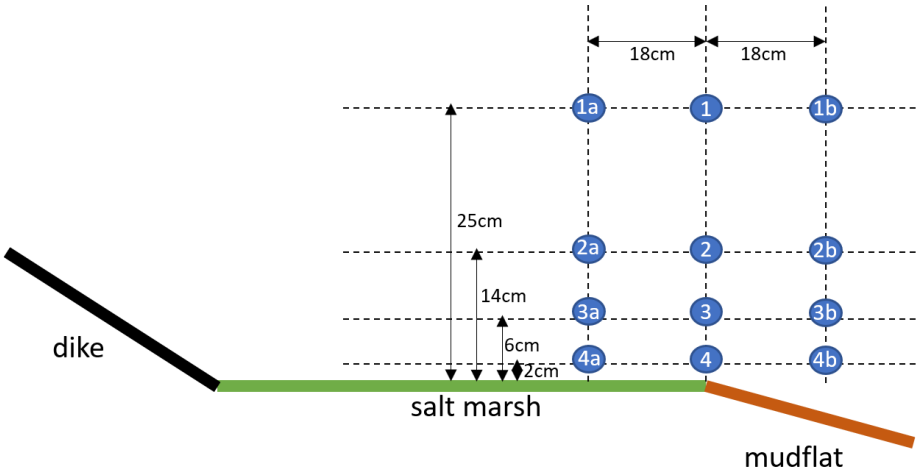

Figure 2-14, ADV validation measurement locations for the scenario with no cliff

The vector data in these points are assessed based on two signal quality metrics, namely 1) the root mean square error (*RMSE*) and 2) the bias compared with the ADV measurements. The RMSE is calculated with the formulas shown below. *N* is the total amount of measurements and the *u* and *w* are the vector components resulting from both measuring methods. The value resulting is an error which has only meaning when compared to the magnitude of the measurements.

$$RMSE_u = \sqrt{\frac{\sum_{n=1}^{N}(u_{ADV\,n} - u_{PIV\,n})^2}{N}}$$
$$RMSE_w = \sqrt{\frac{\sum_{n=1}^{N}(w_{ADV\,n} - w_{PIV\,n})^2}{N}} \quad (3)$$

The bias is used to check if there is an overall offset or bias between the two measurement techniques. It is calculated by subtracting the PIV measurement value from the ADV measurement value, and dividing it by the ADV measurement value. This is done for all the values and summed to gain an average percentage. The percentage bias (*PBIAS*) formula can result in both negative and positive values depending on a negative or positive shift of the PIV relative to the ADV.

$$BIAS\ \%_u = \sum_{n=1}^{N} \frac{u_{PIV\,n} - u_{ADV\,n}}{u_{ADV\,n}}$$
$$BIAS\ \%_w = \sum_{n=1}^{N} \frac{w_{PIV\,n} - w_{ADV\,n}}{w_{ADV\,n}} \quad (4)$$

The peaks in both the *u* and *w* component can be compared with orbital velocities that are expected under a wave. In this setup the shallow water equations do not yet apply (since $h < 0.05L$ is not met), therefore the general orbital velocity formula is used to calculate the maximal *u* and *w* velocity component.

$$\hat{u}(z) = \frac{\pi H}{T} * \frac{\cosh\,[k(z+h)]}{\sinh\,(kh)}$$
$$\hat{w}(z) = \frac{\pi H}{T} * \frac{\sinh\,[k(z+h)]}{\sinh\,(kh)} \quad (5)$$

At the measurement location the local water level (*h*) is 0.46 m, the offshore wave height (H_0) is 0.10 m and the wave period (*T*) is 1.6 s. The wave number (*k*) and the wave height (H) are determined with

an analytical lookup table (van der Werf, 2021), based on the relation between the offshore water wavelength and the water depth. The offshore wavelength, the resulting relation between the wave height and offshore water height, and the resulting relation between the wave number and water depth are given below.

$$L_0 = \frac{g\,T^2}{2\pi} = 3{,}99\text{m}; \quad \text{H} = \text{H}_0 * 0{,}926 = 0.093\text{m}; \quad \text{k} = \frac{0.940}{\text{h}} = 2{,}05 \tag{6}$$

The expected peak orbital velocities at the different water levels are shown in

Table 2.

Table 2, Expected maximum orbital velocities at the ADV measurement locations

Component and water depth	Velocity (m/s)
$\hat{u}(-0.21)$	0.223
$\hat{u}(-0.32)$	0.189
$\hat{u}(-0.40)$	0.184
$\hat{u}(-0.44)$	0.177
$\hat{w}(-0.21)$	0.105
$\hat{w}(-0.32)$	0.052
$\hat{w}(-0.40)$	0.022
$\hat{w}(-0.44)$	0.007

Similar procedure is followed for a saltmarsh setup including a 12 cm cliff. For this validation the offshore wave conditions where, a water depth of 0.55 m, an offshore wave height of 0.10 m and a wave period of 1.5 s. Validation measurements were taken at 11 locations around the cliff (Figure 2-15). The locations in front of the cliff and near the bed are expected to show complex flow patterns and are therefore of the highest interest. A comparison between the measurements and the maximum orbital velocities from linear wave theory will deviate, due to the abrupt change in bed level in form of the cliff.

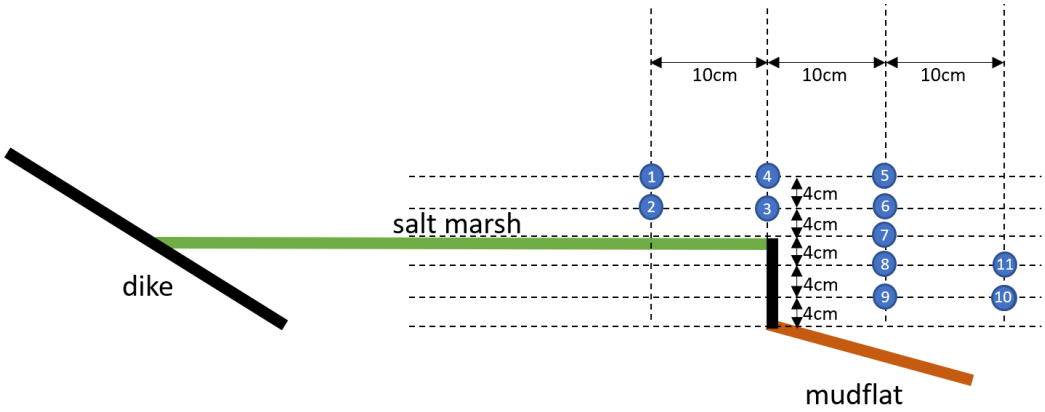

Figure 2-15, ADV measurement locations of the validation case with a 12cm cliff.

2.6. Near-cliff velocities analysis

When the accuracy of the velocity fields are stated, they are used to investigate the hydrodynamics of which high near bed velocities are part of. This will be derived by analysing the velocity fields of the base experiment, M07, which will be compared to the other experiments.

The effect of a difference in water level is analysed by comparing M08 to base experiment M07, where the water level increases from 9 to 19 cm on the saltmarsh and the wave height and period stay the same. The M01 experiment was carried out to assess the influence of lowering the water level, but to much noise was present in the area of interest by air bubble entrainment due to wave breaking at the cliff. M02 and M03 are used for analysing the effect of change in wave height compared to M07. The M04, M05 and M06 experiments are used to analyse the effects of change in wave period. The comparison between experiments for analysing the effect of changing a wave characteristic is shown in Table 3.

Table 3, Experiments used to analyse the effect of changing a specific wave characteristic. The M07 experiment is displayed in bold as it is the base experiment.

Wave characteristic investigated	Experiments used
WL on the saltmarsh	**M07**, M08
Wave height	M02, **M07**, M03
Wave period	M04, **M07**, M05, M06

Each experiment results in 20 velocity fields every second, during the time for 10 fully developed waves to transverse over the cliff. To analyse important patterns in the velocity fields, the phase-average velocity maps are calculated for each experiment. The phase-averaging process involves calculating the average velocity field for all the waves in a certain wave phase. This reduces the effect of incidental inaccuracies in the wave generation or in the velocity field measurements.

2.6.1. Velocity patterns (RQ 3)

Initially, the velocity fields in different points in time and the time-averaged velocity map of the base case M07 are visualized. The time-averaged *u* component is analysed to visualize processes such as Stokes drift and undertow. Particular attention is given to velocities in front of and on top of the cliff which are part of the vortices that are created by return flow detachment over the cliff. This vortex is described to be a probable cause of lateral cliff erosion by Suzuki & Klaassen (2011). They also report on a vortex on top of the saltmarsh, which will be investigated as well.

The patterns found in the time-averaged velocity fields of the base case M07 are compared to the other experiments. When remarkable differences are found the phase-averaged velocity maps are analysed to describe the hydrodynamics that cause them.

2.6.2. Effect of wave characteristics on near-bed velocities (RQ 4)

The velocity patterns that have large near-bed velocities are of interest, and are therefore found with local peak near-bed velocity maps. The flow direction in which the high near-bed velocities are directed and the locations at which they occur are listed. The hydrodynamics of which these near-bed velocities are part of, are observed and reported.

The effect of differing wave characteristics on the peak near-bed velocities is assessed in those regions. The local velocity peaks in the positive and negative direction of both the *u* and *w* are extracted from the phase-averaged velocity fields. This results in 4 peak velocity maps: one with velocities pointing upwards, one downwards, one towards the dike and the last on towards offshore. The saltmarsh and cliff surfaces are impermeable, and thus no velocities are expected in the direction perpendicular to the surface. Therefore, only the positive and negative *u* components are of interest on the saltmarsh and on the mudflat, while that is the case for the *w* components against the cliff face (the parallel directions). Then the maximal near-bed velocities are extracted from the peak-velocity maps to visualize the peak near-bed velocities over the mudflat, saltmarsh and against the cliff face. The effect

of a changing wave height, water depth and wave period can be analysed with this data, and conclusions are drawn from them.

3. Results

3.1. PIV setup verification

3.1.1.1. Particle size and concentration

Using the setup outlined in section 2.2 (PIV setup), the particles in the water should appear in the PIV images larger than one pixel according to an initial calculation sheet. Assessing the raw image from an arbitrary experiment (M08 in Figure 3-1) confirms this by displaying several particles that cover more than 1 pixel.

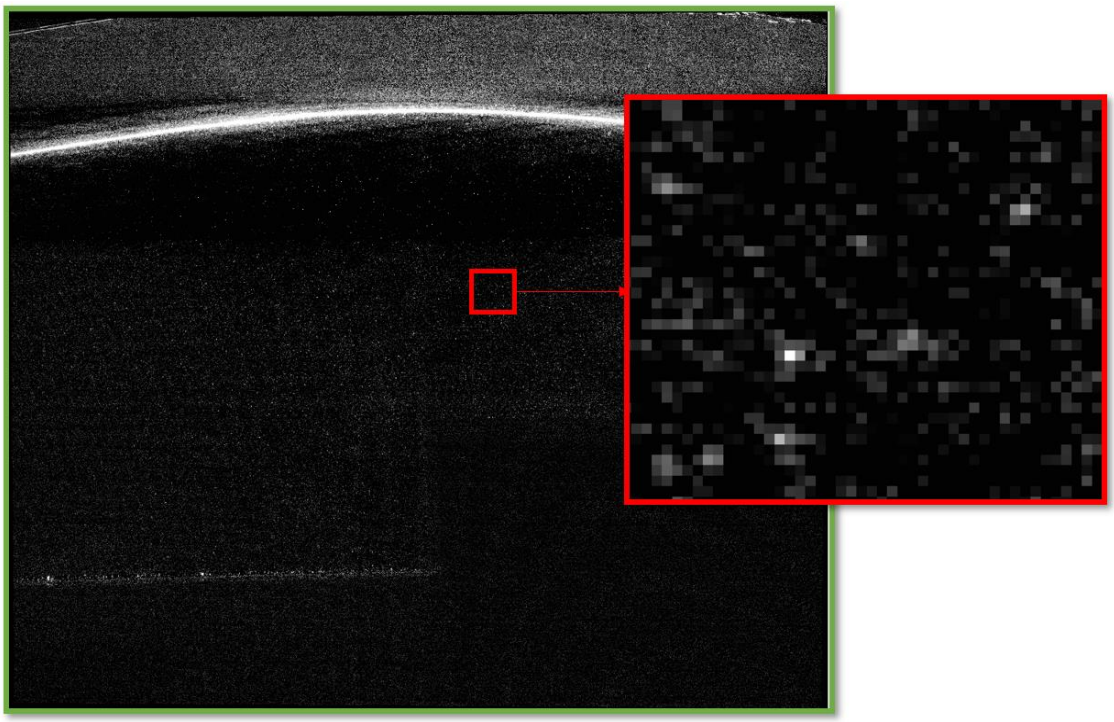

Figure 3-1, , Raw captured image (green) and zoomed section (red) in which particles cover several pixels.

The interrogation window size is set to 32x32 pixels. In one interrogation window on average 10 particles should appear. A first check is made by zooming in to one interrogation window and counting the amount of particles visible by the eye. Figure 3-2 presents an interrogation window and the 11 particles that are captured within it, which is well within the required particle concentration boundaries. When the number of particles per interrogation window would be outside the boundaries, a significant amount of false vector arrows would be present in the vector field. Most of the calculated vectors are not rejected by either local mean or standard deviation threshold (Figure 3-3). This indicates that the particle concentration is well within boundaries.

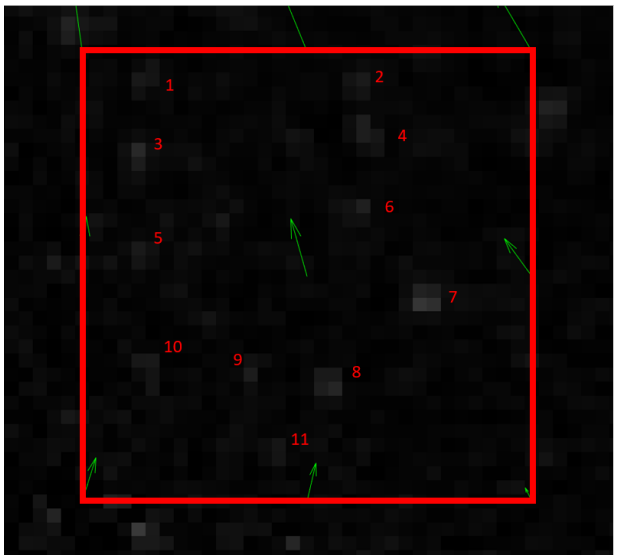

Figure 3-2, Number of particles counted in one interrogation window on an image captured as it is. no processing has been performed on this image. The resulting vector magnitude and direction is shown by the green arrow in the centre of the interrogation window. There are arrows on the edges of the interrogation window because an overlap of 50% is used to increase the vector density of the field.

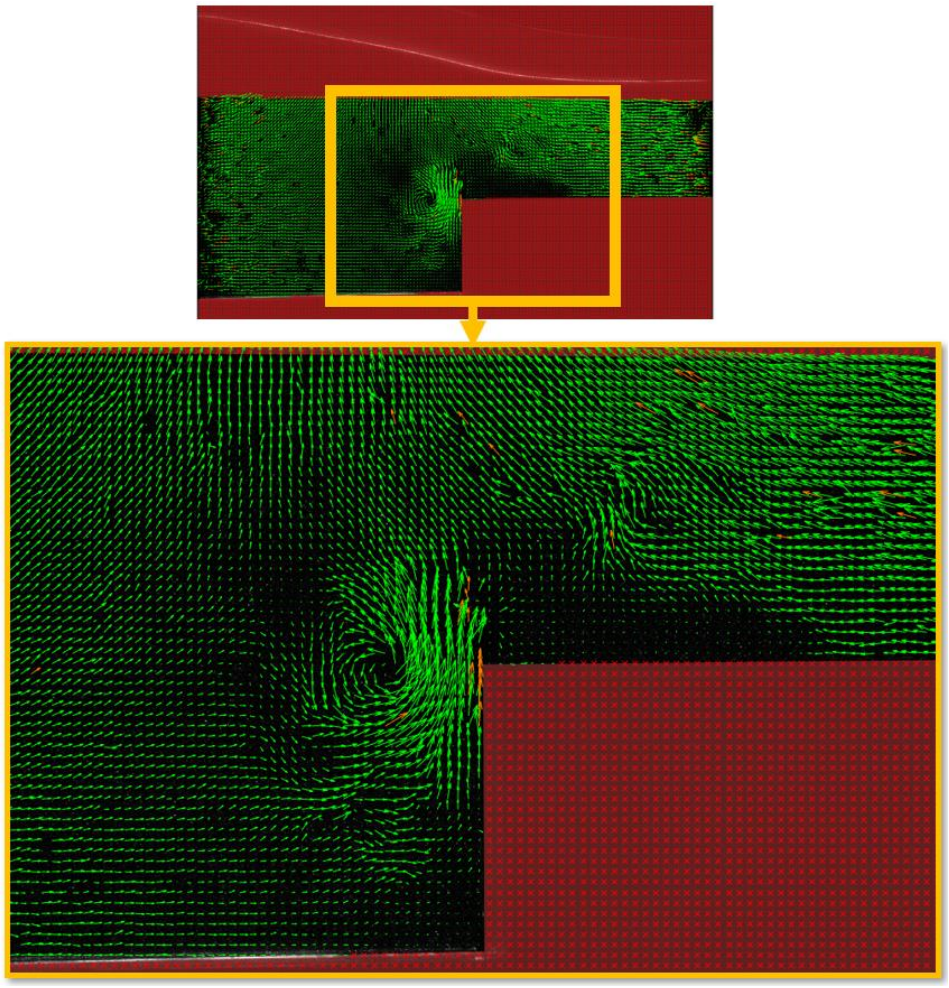

Figure 3-3, Vector field for one moment in time for a setup with a cliff. The red coloured arrows in Figure 3-3 are statistically rejected by exceeding either the local mean or the standard deviation threshold. The field is almost completely green aside from a small area against the top of the cliff.

3.1.1.2. Particle movement

The time interval between the first and second images in a vector field is chosen to ensure that particles do not travel a distance exceeding half of the interrogation window. In the near cliff region maximal velocity vectors of ~1 m/s are observed (M06 in Appendix C). With a timestep set to 4200µs, particles will travel 4.2 mm for a 1 m/s velocity.

$$x_{max} = v_{max} * \Delta t = 1 * 0.0042 = 0.0042\ m \tag{7}$$

$$maximal\ pixel\ displacement = \frac{x_{max}}{pixel\ size} = \frac{0.0042}{0.00028} = 15\ pixels \tag{8}$$

One pixel is 0,28 mm in width and height. The maximal particle displacement is therefore 15 pixels, which is within half of an interrogation window (16 pixels). If this ratio between the timestep and the interrogation window size would be higher than 16 pixels, the cross-correlation of that interrogation window would yield invalid vectors. Looking at the calculated velocity fields, this is not the case (Figure 3-3).

The calculated velocity vectors are further analysed by showing the histogram and relation between the *u* and *w* component of each vector (Figure 3-4). It shows that the velocity limit of 16 pixel/frame is not reached. The histogram and plot do not show a tendency of the particle displacement approaching an integer number (as can be seen in the example in Figure 2-9), thus no peak locking occurs in this vector field.

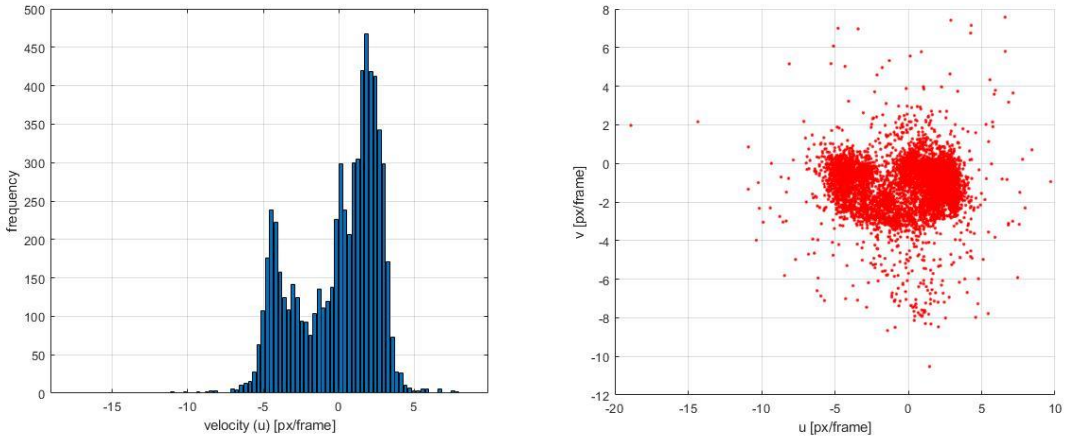

Figure 3-4, A histogram of pixel displacement at for the velocity field of Figure 3-3 (left panel) and the u and w component scatterplot (right panel).

3.1.1.3. Noise

Verifying all PIV requirements, the imaging processing is expected to yield clear velocity fields. However, in certain experiments, external factors led to noise in the area of interest. In some instances, small 'clumps' of material were discovered near the cliff, causing the calculation of invalid vectors . The source of this material remains unclear, but it could potentially be contamination from previous experiments in the form of tiny plastics sticking together. Breaking waves and return flow from the dike can create noise at the area in front of the cliff in the form of entrained air bubbles. Especially during small water depths, heavy breaking and air entrainment occurs at the cliff. The areas in which these air bubbles occur cause false velocity patterns due to the density difference of the air bubbles compared to water and therefore incorrect velocity vectors. This is especially the case during experiment M01 (Figure 3-5), which led to decide not include this experiment for the near-cliff velocity analysis..

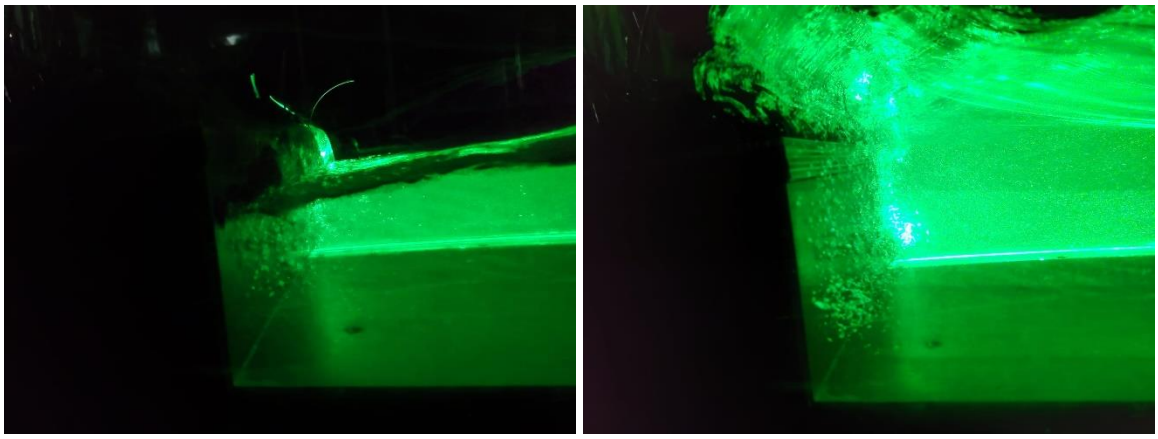

Figure 3-5, Air bubble noise in the water column generated by return flow (left) and breaking waves (right) for the M01 case discussed in section 2.6. The images were captured in the dark room using a mobile camera configured with an extended shutter time. This setting accounts for the visibility of the green light emitted by the LED PIV in the images

3.2. PIV accuracy analysis

To have a measure of accuracy of the PIV measuring technique in this setup, the PIV derived measurements are compared with ADV measurements. The measured ADV and PIV signal is presented for both situations, with and without a cliff. The maximal orbital velocities obtained through PIV and ADV are compared with the maximal velocities through linear wave theory in a scenario without a cliff.

3.2.1. Comparison without a cliff

Figure 2-14 illustrated the locations where ADV measurements are taken in the scenario without a cliff. The resulting *u* and *w* velocity components of both the ADV and the PIV at these locations are presented in Figure 3-6. The PIV velocity signal is extracted from the integration window located at the same position as the ADV measurement. To precisely identify the corresponding location in the PIV measurements, images of the ADV sensor are taken before the tests and the calibration procedure is followed to derive orthogonalized x and z coordinates of the exact measuring point of the ADV. The measuring location is 5 cm below the transducer. For this location in the calibrated image, the corresponding PIV interrogation window (and therefore velocity vector) is extracted and compared with the ADV measurement.

The *u* velocities show a smooth sinusoidal pattern at all the measurement depths, where the *w* component shows a more irregular pattern. Especially near the bed, at location 4, the PIV shows peak velocities that exceed the maximum orbital velocities according to linear wave theory, and these also diverges more from the ADV measurements than at other locations.

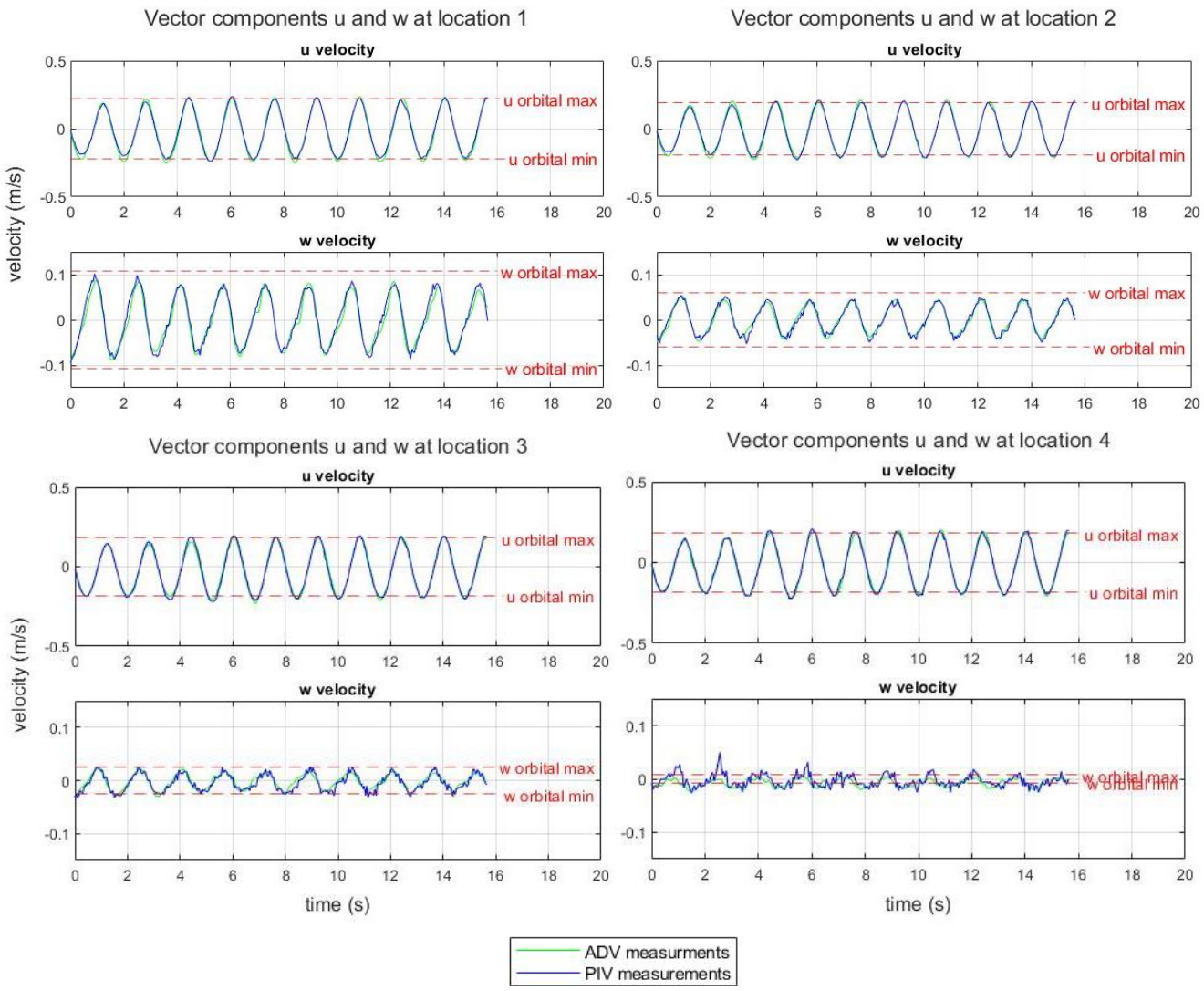

Figure 3-6, , Validation of the PIV measurements for the case without a cliff at the 4 numbered locations in Figure 2-14. The green line in the graphs is the smoothened ADV data and the blue PIV results are plotted on top of it in blue. The red dashed line is the maximum expected orbital velocity based on linear wave theory for the different measurement heights (25, 14, 6 and 2 cm form the bed for locations 1, 2, 3 and 4 respectively).

For all the 12 locations the RMSE and PBIAS are calculated (Figure 3-7 and Figure 3-8). Every measurement depth has 3 measurement points, as shown in Figure 2-14. Location 1a has the same water depth as location 1, but located at the left of location 1, while location '1b' is on the right of it. The same system is applied to the other measurement depths. The RMSE scores have also been plotted as percentages of the maximal orbital velocities that are expected at that location based on linear wave theory, to provide context to the RMSE values. When the measured velocities are higher, the RMSE is expected to be higher as well, while the relative error could be lower.

The RMSE values of the *u* component fall within a 0.025 m/s region and the *w* component fall within 0.015 m/s. These error values are higher than those solely expected from the ADV (~0.005 m/s) but are still interpreted as negligible in comparison to the peak near-bed velocities we are interested in.

The RMSE of the *u* component remains within 10% of the expected maximal orbital velocity. An error is anticipated due to the fact that the PIV and ADV data were not obtained in the same run, introducing inconsistencies in the generated orbital velocities and resulting in an error when comparing the two measurements. The RMSE in the *w* component increases as a percentage of the maximal expected

velocity component when the velocities become smaller. At the depths of locations 1 and 2, the RMSE is also about 10% of $\hat{w}\ max$, while it rises to 25% and 100% at locations 3 and 4, closer to the bed. The PBIAS in the different locations does not exceed 10 percent, except for the *w* component at location 4. This bias reflects the noise in the PIV *u* component of location 4 in Figure 3-6.

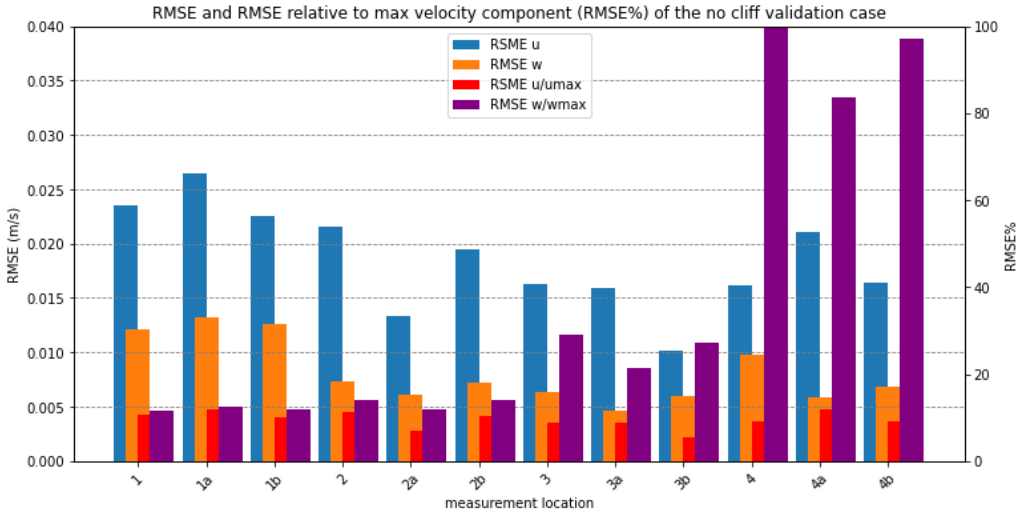

Figure 3-7, No cliff scenario RMSE values for the u and v vector components (blue and orange bars) of the PIV compared to the ADV. The red and purple bar represent the RMSE as a percentage of the maximal expected orbital velocity component. See Figure 2-14 for the exact locations.

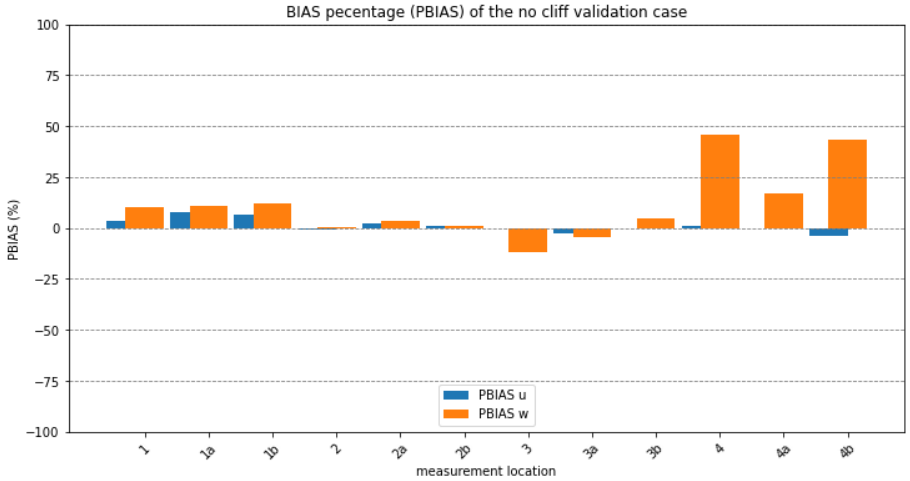

Figure 3-8, No cliff scenario PBIAS values for the u and v vector components (blue and orange bars) of the PIV compared to the ADV. See Figure 2-14 for the exact locations.

3.2.2. Validation with a 12cm cliff

Figure 2-15 showed the locations for which the PIV is compared to the ADV measurements, when a 12cm cliff is present. These points are chosen because of the high interest in the near cliff regions of the velocity fields.

In Figure 3-9 the PIV and ADV time series for the velocity components are plotted for four locations: 1, 3, 7 and 8. At location 1, which is located 8 cm above the saltmarsh, the velocity profiles closely align for both the *u* and *w* components. Even though there is a slight difference in the shape of the *w* component orbital cycle, it still corresponds well. At location 3, which is 4 cm above the saltmarsh edge,

the velocity profile of the PIV in the *w* component shows more variation compared to the ADV. The upward velocities measured with the PIV are notably higher than those recorded by the ADV in this location. In locations 7, which is 10 cm in front of the cliff edge, the time series match well again, whereas in location 8, which is closer to the mudflat bed, some unexpected fluctuations in the orbital cycles of both the ADV and the PIV are observed.

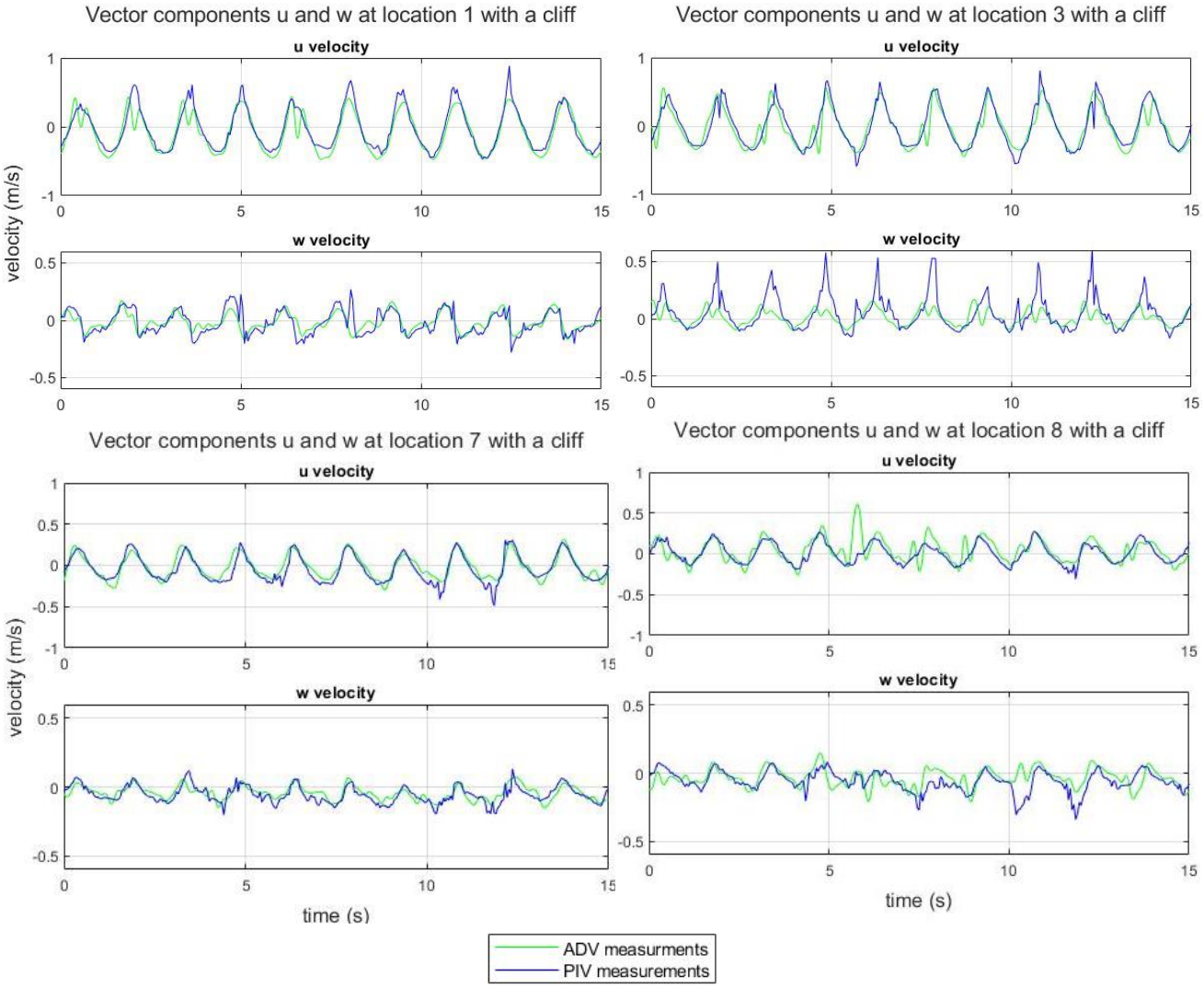

Figure 3-9, Validation of the PIV measurements for the case with a cliff at the locations 1, 3, 7 and 8 (Figure 2-15). The green line in the graphs is the smoothened ADV data and the blue PIV results are plotted on top of it in blue.

The resulting RMSE and PBIAS scores for all the locations are shown in Figure 3-10 and Figure 3-11. The scores indicate a lesser degree of similarity between the ADV and PIV compared to the case without a cliff. The RMSE scale in this figure extends up to 0.4m/s, whereas it was 0.04m/s in the case without a cliff. The RMSE value of the *u* component at location 2 could be argued to be an outlier, but the RMSE for most locations is in the range of 0.1 to 0.15 m/s, which is significant compared to the maximum velocities (1 m/s) we intend to measure. Therefore the PIV measured velocities in one location in this complex hydrodynamic region around the cliff have to be put into context before they are presented as the actual velocities.

To provide context to the resulting RMSE scores, the RMSE is plotted as a percentage of the highest 2% of the velocity components at the measurement location (red and purple bars in Figure 3-10). The RMSE of both the *u* and *w* components in all the measurement locations fall within 15 to 45% of the

highest 2% velocity components. These percentages also indicate that the use of the vector data around the cliff deviates a lot from the ADV.

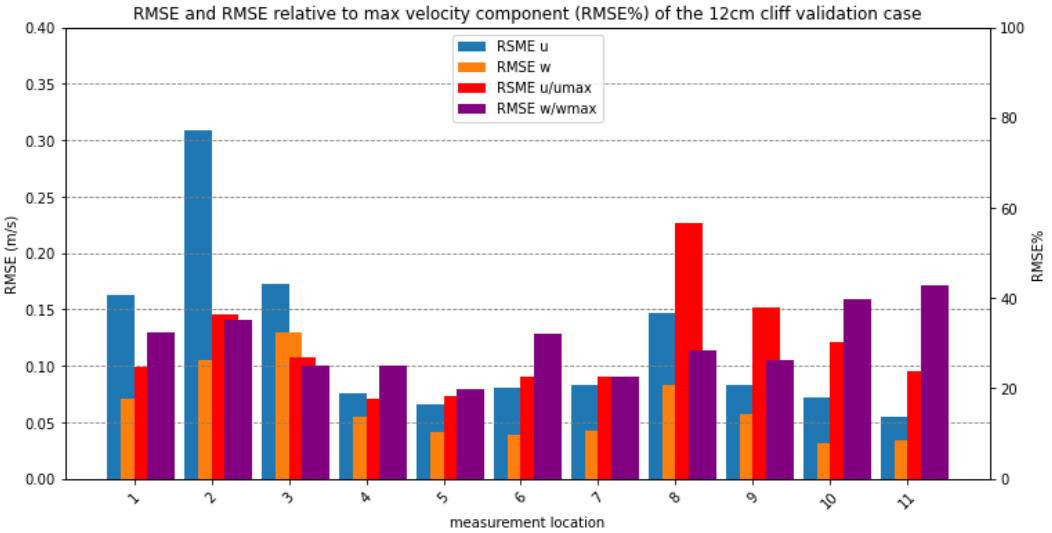

Figure 3-10, The 12 cm cliff scenario RMSE values for the u and v vector components (blue and orange bars) of the PIV compared to the ADV. The red and purple bar represent the RMSE as a percentage of the highest 2 % velocity component.

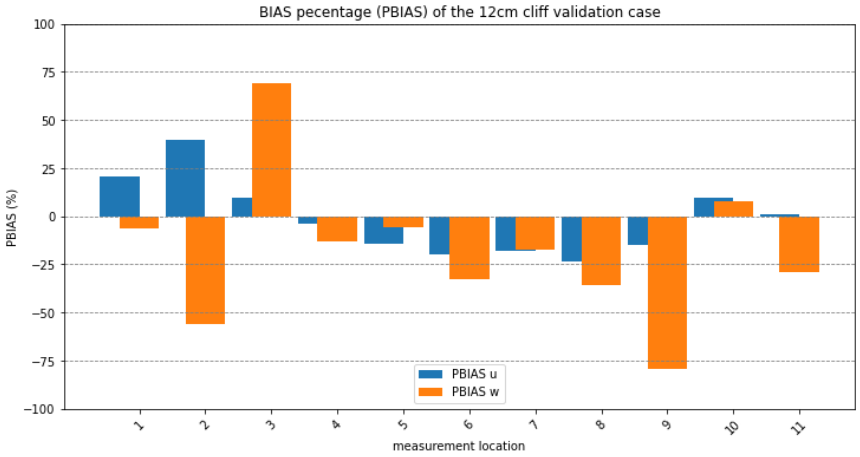

Figure 3-11, The 12 cm cliff scenario PBIAS values for the u and v vector components (blue and orange bars) of the PIV compared to the ADV.

The lower performance of the RMSE is not solely due to PIV measurements error, but is also highly impacted by inconsistent velocity component cycles and noise in the ADV measurements. As an example, reference is made to the *u* and *w* velocity component measurements at measurement locations 1 and 8 (Figure 3-9). The ADV measured *u* component at location 1 shows a trough in the middle of the peak in the first 5 cycles, which is not expected to actually have happened. A more likely explanation would be a vibration of the ADV device, or measurement errors.

However, There is no clear pattern in over- or underestimating the values, since the PBIAS is both positive and negative in both vector components. The high values of the PBIAS occur in the *w* direction at the locations that are closest to the bed, locations 2, 3 and 9. The PBIAS at these locations is off a lesser concern, as explained in the no cliff scenario. But the values are much higher than in the less complex hydrodynamic region where no cliff is present, indicating more and higher deviations from the measured ADV vector velocities.

3.3. Near-cliff velocities analysis

The following section examines the measured velocity fields around a cliff. Flow patterns are analysed with phase-averaged velocity fields and time-averaged velocity fields. Then an analysis of the local peak near-bed velocities around a cliff is presented.

3.3.1. Velocity patterns

In this section the observed hydrodynamic patterns are explained with help of both time-averaged velocity maps and velocity fields. The patterns are described with the time-averaged velocity maps (Figure 3-12) and velocity fields measured at 6 different moments in the wave period (Figure 3-13 till Figure 3-18), for base experiment M07. The effect of differing wave characteristics on the patterns are highlighted. The time-averaged velocity maps of the experiments with different wave characteristics can be found in Appendix B. The time-averaged velocity maps of the *u* component of all experiments show average velocities toward the dike near the water level, where this is in opposite direction near the saltmarsh bed. This is expected due the occurrence of Stokes drift and compensating return flow.

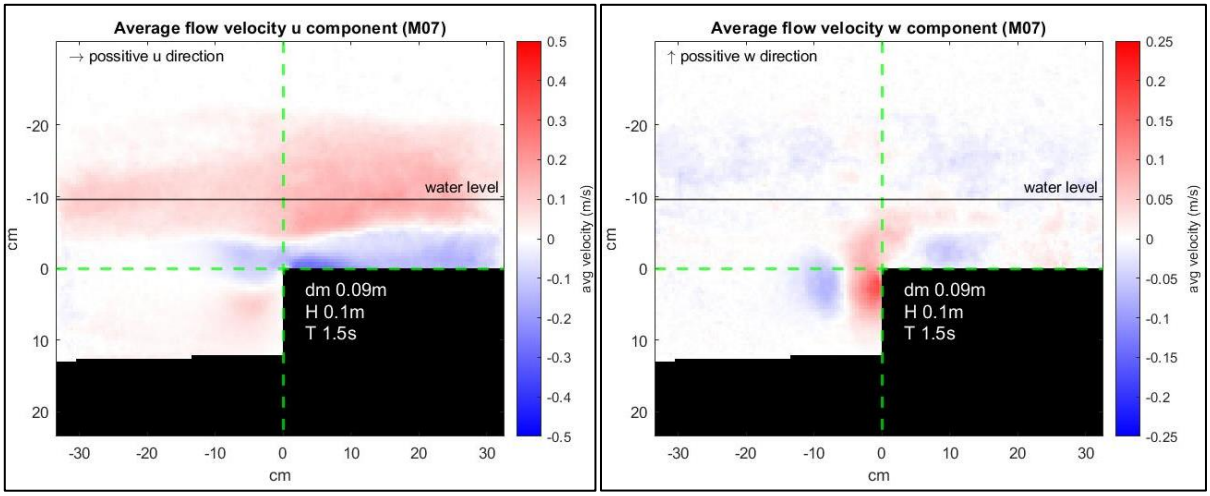

Figure 3-12, time-averaged velocities maps for the u and w components in the base experiment M07. (dm is the water level on the saltmarsh, H the offshore wave height and T the wave period).

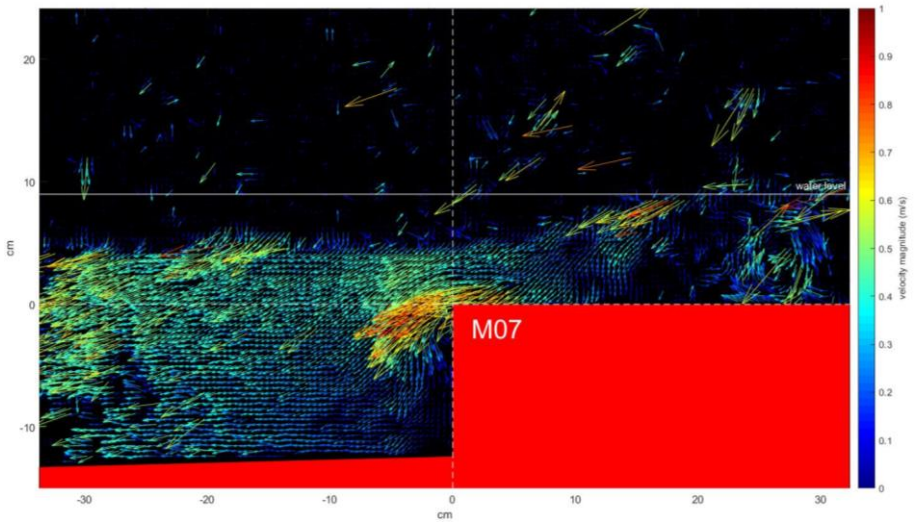

Figure 3-13, M07 velocity field at t=t_0. Return flow is starting to form as the wave crest passed out of the right side of the image.

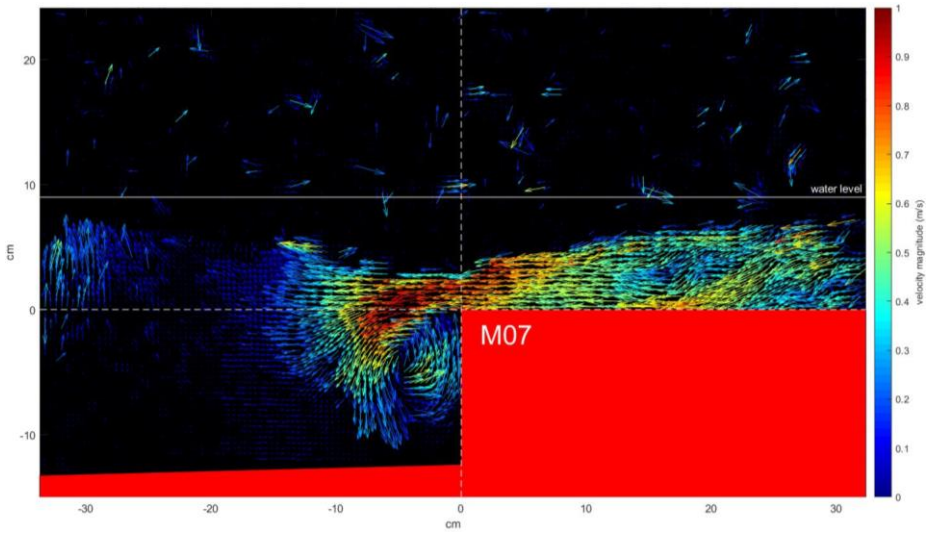

Figure 3-14, M07 velocity field at t=t0+1/6T. The return flow is now further developed, initiating a vortex in front of the cliff face.

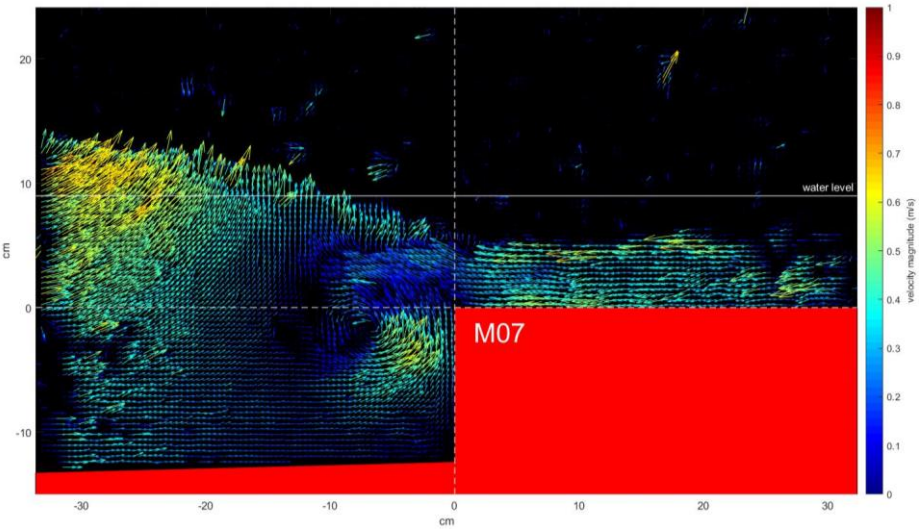

Figure 3-15, M07 velocity field at t=t0+2/6T. A fully developed vortex is starting to be pulled upwards as a new wave crest is entering the image on the left side.

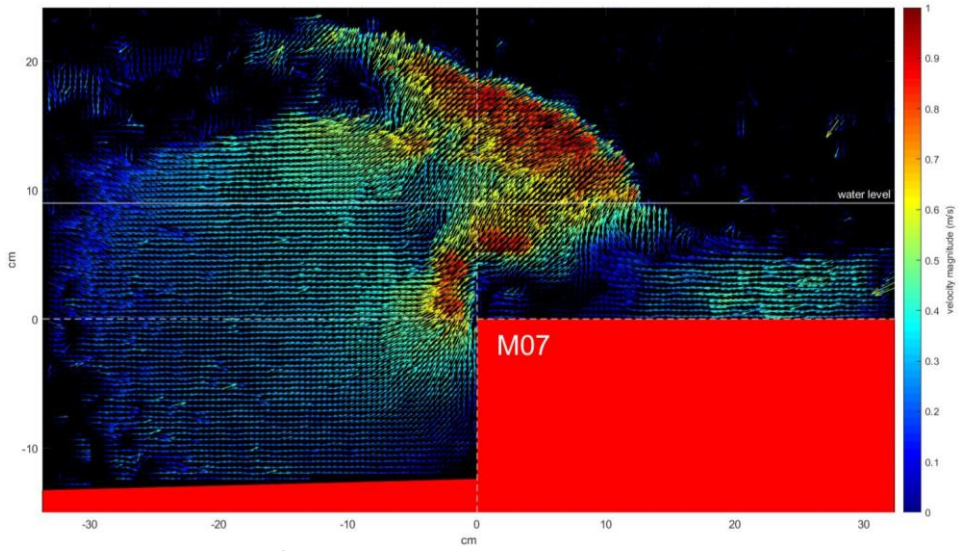

Figure 3-16, M07 velocity field at t=t0+3/6T. The vortex opened up and joined the crest flow. Flow is compressed against the cliff face as the waves pulls the water upwards.

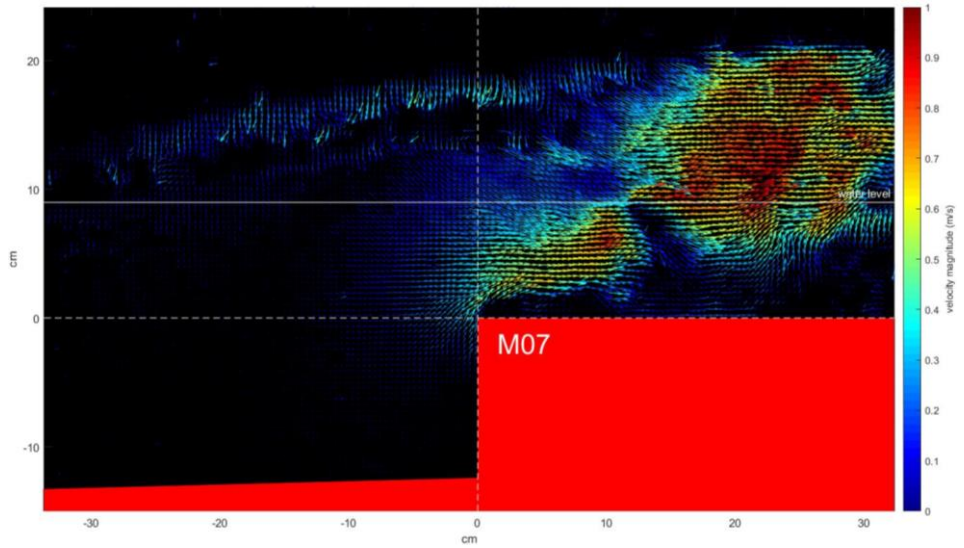

Figure 3-17, M07 velocity field at t=t0+4/6T. The wave crest is above the cliff, transporting water towards the dike.

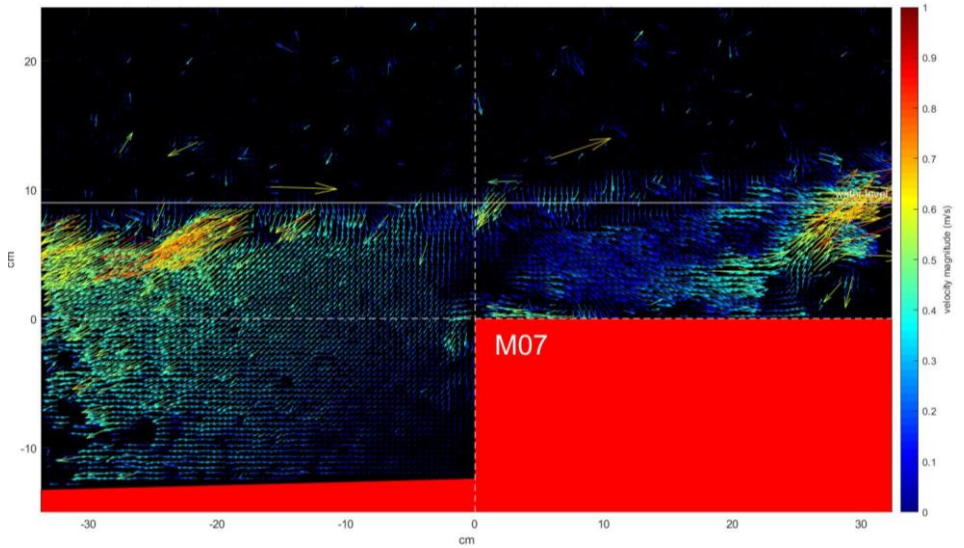

Figure 3-18, M07 velocity field at t=t0+5/6T. The last part of the wave crest passes out of the right side of the image. While flow is still towards the dike on the saltmarsh, the water on the mudflat is already pulled backward by the next wave crest.

3.3.1.1. Vortex in front of the cliff

The simulation of storm conditions during the experiments is expected to result in the creation of a vortex in front of the cliff, as described by Suzuki & Klaassen (2011). To visualize the velocity fields over time, a video or images can be used to observe the vortex. Figure 3-13 till Figure 3-18 showcases six different stages in the creation and decomposition of the vortex (which has its centre at x=-5 cm and y=-5 cm). This follows the pattern described by Suzuki and Klaassen. The vortex is moving anti-clockwise in the images (upwards velocities against the cliff face), which can also be observed in the time-averaged velocity components (Figure 3-12). The red region located in front of the cliff shows an average velocity to the dike, while the blue region on top of it shows an offshore direction. A similar pattern can be observed in the mean *w* component, where water moves upward against the cliff and downward further offshore. The vortex creates near-bed velocities on the cliff face, and possibly on the mudflat in front of the cliff if the vortex gets large enough to interact with the mudflat.

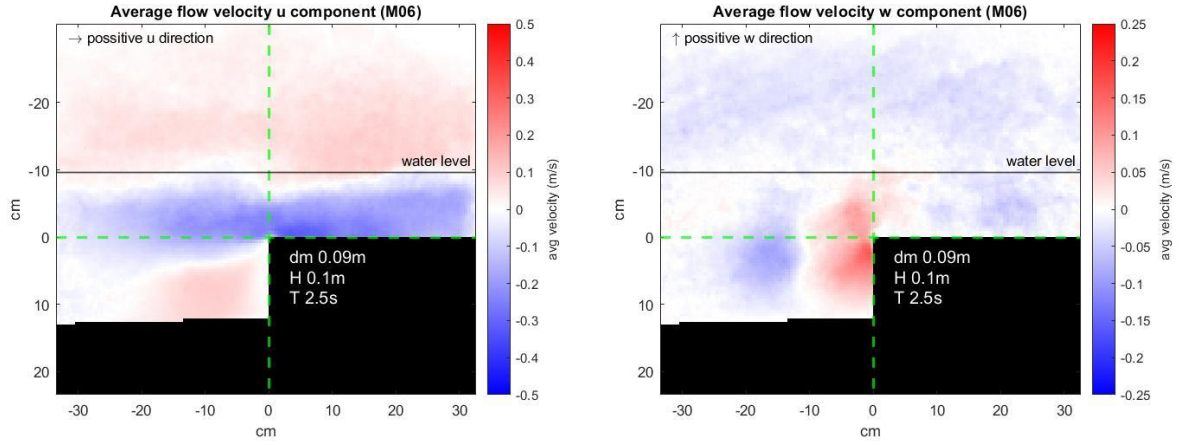

Figure 3-19, Time-averaged velocity map for M06 (longer wave period +1s), where the red and blue region in front of the cliff are much larger than at the M07 base-case (Figure 3-12)

Increasing the wave period (Figure 3-19) and wave height increases the size of the vortex, while a water level increase does not affect the vortex size. The split between the blue and red area in the base experiment are horizontal and vertical for the *u* and *w* components respectively. This is not the case for the larger vortices. The experiment with a larger wave height is used as an example where the blue and red regions are divided with a tilted line (Figure 3-20). This occurrence suggests that the vortex grows in size while its centre travels downwards and further offshore.

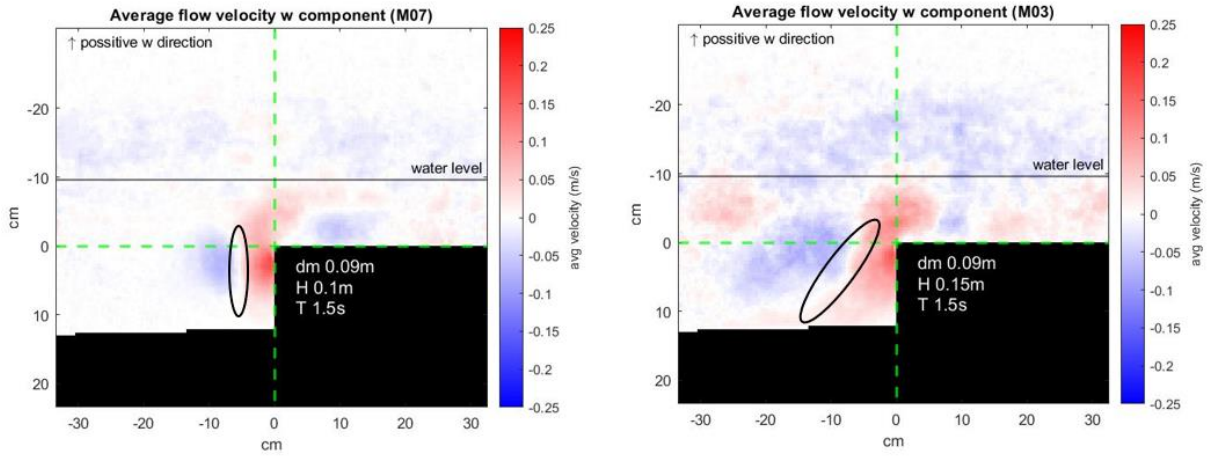

Figure 3-20, Flow separation zone for the vortex in front of the cliff of M07 vs M03.

3.3.1.2. Vortex on top of the saltmarsh

The darkest blue spot in the time-averaged *u* velocity map is found on top of the saltmarsh just behind the cliff edge (Figure 3-12). This indicates faster, or longer return flow in that region. A smaller vortex is found on top of the saltmarsh directly after the cliff edge. This vortex is found when the wave crest is just passed the cliff. Water is pulled over the cliff crest leaving low velocity area on the first part of the saltmarsh, where flow is pulled into a cycle for a small duration. The vortex holds on average for 5 frames in M07, which equals a duration of 0.25 s (or $1/6^{th}$ of the wave period). In Figure 3-16 and Figure 3-17 the vortex can be observed at x=3 cm and y=1 cm. A more zoomed in section is provided in Figure 3-21. Velocities towards the cliff are present over the saltmarsh bed near the cliff, while they are towards the dike in the upper part of the vortex. High near-bed velocities directed offshore could be part of this vortex on the saltmarsh.

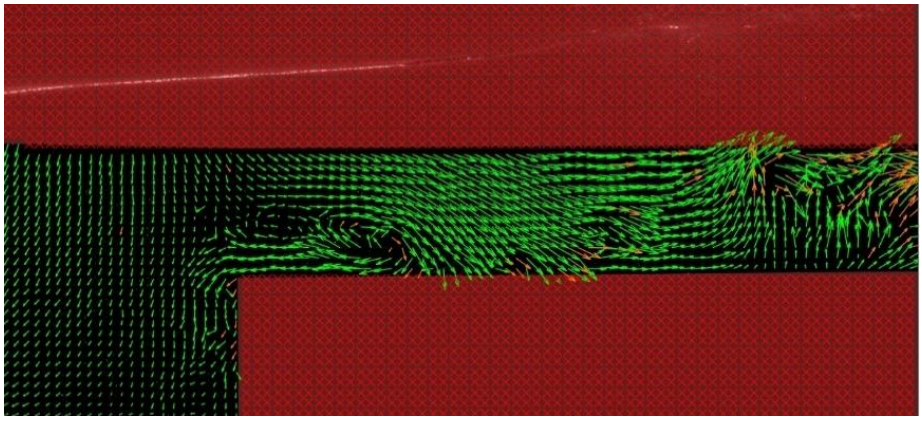

Figure 3-21, Fully developed vortex on top of the saltmarsh.

3.3.2. Effect of wave characteristics on peak near-bed velocities

To indicate the locations that are highly vulnerable to erosion due to local flow field and vortices, the phased-averaged peak or maximum velocities are calculated for each scenario. Specifically, this study focusses on erosion hotspots due to near-bed velocities. As such, the near-bed peak velocity parallel to the mudflat, cliff and saltmarsh platform are of interest. On top of the saltmarsh platform and on the mudflat, the velocity peaks towards the dike and the return flow are of interest (positive and negative *u* component), where the up and downward velocity peaks are of interest along the cliff face (positive and negative *w* component). First, the base case experiment M07 is analysed, after which the effect of the changes in wave characteristics will be assessed through the other experiments. The peak velocity maps for the four velocity directions in the base case experiment, M07, are shown in Figure 3-22. The peak velocity fields for the other experiments can be found in Appendix C.

The peak negative *u* component (towards the left), shows a strong return flow over the saltmarsh (Figure 3-22 A). The return flow is only present in the lower part of the water column on the saltmarsh, and diffuses when the water depth becomes larger on the mudflat. The peak velocities near the bed of the saltmarsh get higher closer to the cliff, which is likely due to the vortex propagating on top of the saltmarsh.

High velocities under the wave crest towards the dike are observed in the peak velocity map to the right (Figure 3-22 B). The peak velocities in the wave crest get higher when the water depth becomes smaller, as can be seen by the higher velocity peaks above the saltmarsh than above the mudflat. There are high near-bed velocities on top of the saltmarsh as well as on the mudflat. On the saltmarsh the higher near-bed velocities are found 20 cm after the cliff. This is because the wave crest pulls water up

and forwards and compresses the flow around the top of the cliff, resulting in higher velocities that are not near the saltmarsh bed (further initiating flow detachment and a vortex on top of the saltmarsh).

The highest velocities in the negative *w* component (down ward flow) are concentrated under the wave crest and in front of the cliff due to the vortex in front of the cliff (Figure 3-22 C). Except for that small region at the cliff edge, there is no location where significant near-bed velocities are noticed.

There is a clear peak positive *w* velocity component (upward) area in front and above the cliff (Figure 3-22 D). When the vortex is propagating upwards under the incoming wave crest, the vortex is compressed against the top part of the cliff face. This creates the high upward velocities against the top of the cliff and continues above the cliff to diffuse over the rest of the water depth. These high peak velocities against the cliff face suggest a local hotspot for erosion.

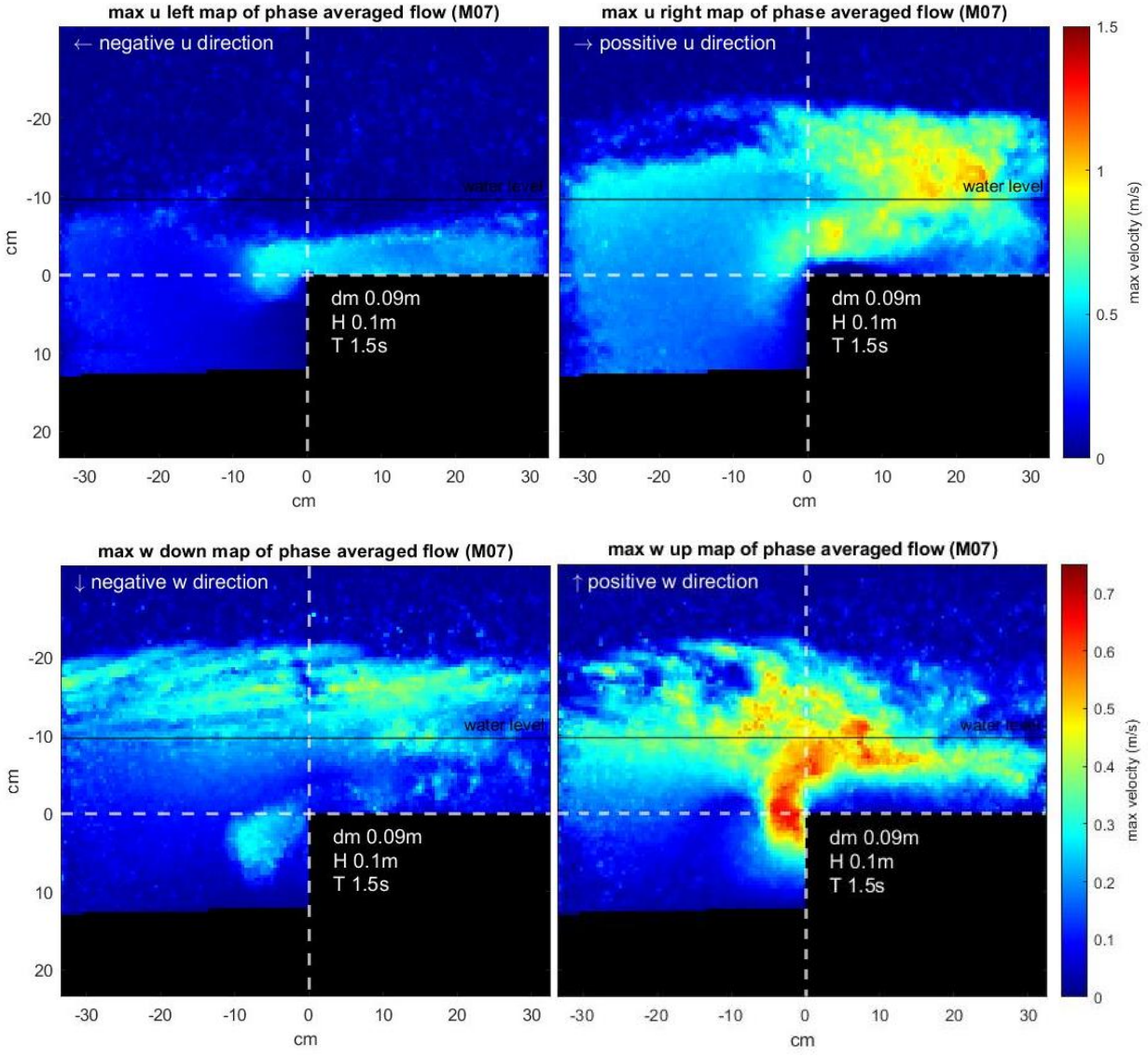

Figure 3-22, Phase-averaged peak velocity maps for the velocity components to the: left (A), right (B), down (C) and up (D).

This leads to the identification of four distinct regions as schematised in Figure 3-23. These regions are vulnerable to local high near-bed or face velocities and indicate a local hotspot for erosion in the near-cliff region.

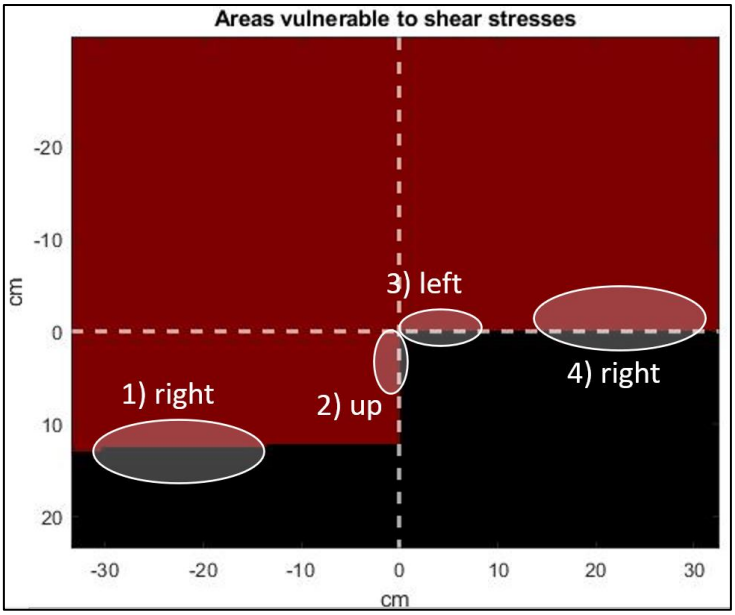

Figure 3-23, Areas around the cliff that are vulnerable to near-bed velocities created by wave-induced hydrodynamics. The flow direction that creates the highest near-bed velocities are displayed for the different locations.

To asse the effect of different wave characteristics, the phase-averaged peak near-bed velocities are collected at the previous defined zones, e.g. the mudflat, saltmarsh and cliff front.

The peak near-bed velocities on the mudflat are larger towards the dike than offshore (negative x-axis of Figure 3-24). Increasing the water depth or lowering the wave height (M08 and M02) reduces the velocities towards the dike, where the increase of the wave height (M03) has barely any effect compared to the base experiment (M07). A clearer pattern is visible with different wave periods and therefore wave length, where a lower wave period (M04) results in lower peak near-bed velocities and the experiments with increased wave periods (M05 and M06) show a step wise increase. Longer wave periods cause a larger vortex in front of the cliff, as has been observed in the time-averaged velocity fields. The increase in size and depth of the vortex creates faster rotational motion, which is towards the dike on the mudflat, of which the peak near-bed velocities on the mudflat are part of.

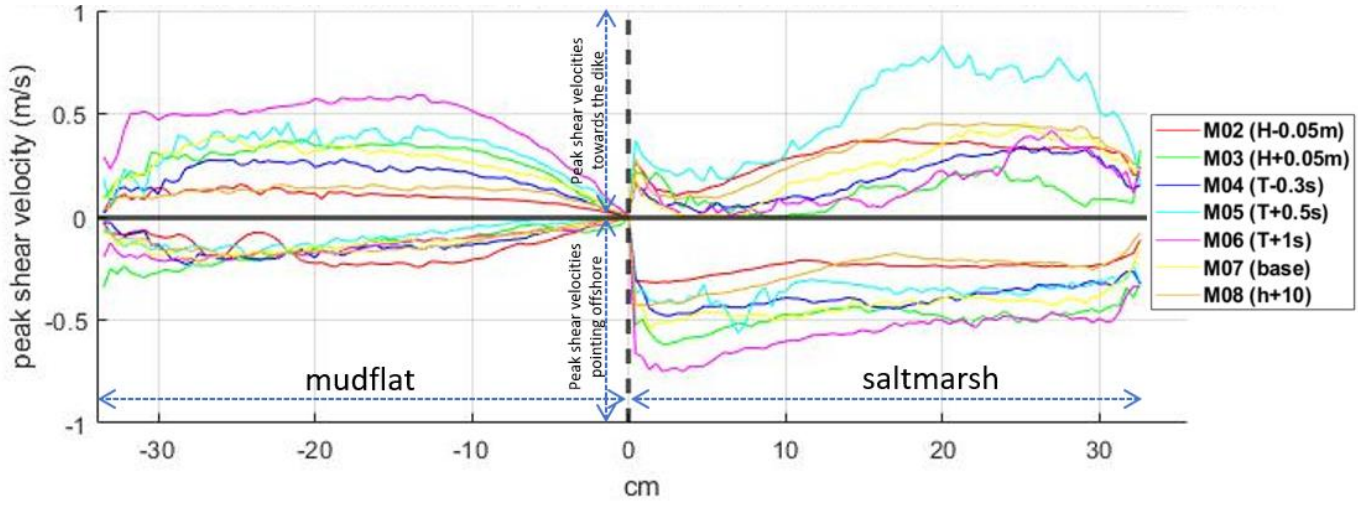

Figure 3-24, The peak near-bed velocities on the mudflat and saltmarsh for the 7 experiments (see legend). The velocities shown on the horizontal bed at the mudflat (left of x=0) and on the saltmarsh bed (right of x=0). The dashed line is the cliff transition, and on the right of it the peak near-bed velocities on the saltmarsh bed are shown. The positive velocities represent the peak velocities to the right (towards the dike) and the negative values to the left (offshore).

Two vulnerable areas have been identified on the saltmarsh platform. The first region is just behind the cliff, which is vulnerable to return flow and the vortex on the saltmarsh. The second region is further towards the dike, where higher peak shear velocities occur towards the dike. These regions are again analysed for the scenarios with different wave characteristics (positive x-axis in Figure 3-24). The highest peak near-bed velocity towards the dike is observed with a slight wave period increase (M05), where a bigger wave period increase (M06) shows a decrease of peak shear velocities towards the dike compared to the base experiment (M07). The opposite pattern is found in the return flow direction, where the highest peak near-bed velocities are observed in M06, while it is reduced in the M05 experiment. An increase of water depth (M08) creates slightly higher peak near-bed velocities towards the dike, where they are much lower pointing offshore compared to the base experiment. The opposite is observed for the experiment with increased wave height (M03).

The cliff face is found susceptible to upward velocities that are part of the vortex in front of the cliff (Figure 3-25). The near-bed velocities grow from the bottom up to 2cm under the cliff edge, where a small reduction is observed. This reduction is most likely to happen due to return flow interfering with the upward motion of the vortex. The peak near-bed velocity against the cliff face shows a positive relation to both the wave period and the wave height. An increase in water depth shows minimal change in peak near-bed velocities compared to the base experiment, which is expected because the vortex observed in front of the cliff has equal size. While all the experiments show a decrease in near-bed velocity towards the cliff top, it keeps increasing in the M05 experiment towards the edge. This behaviour can be linked to the lower return flow peak velocities near coming from the saltmarsh.

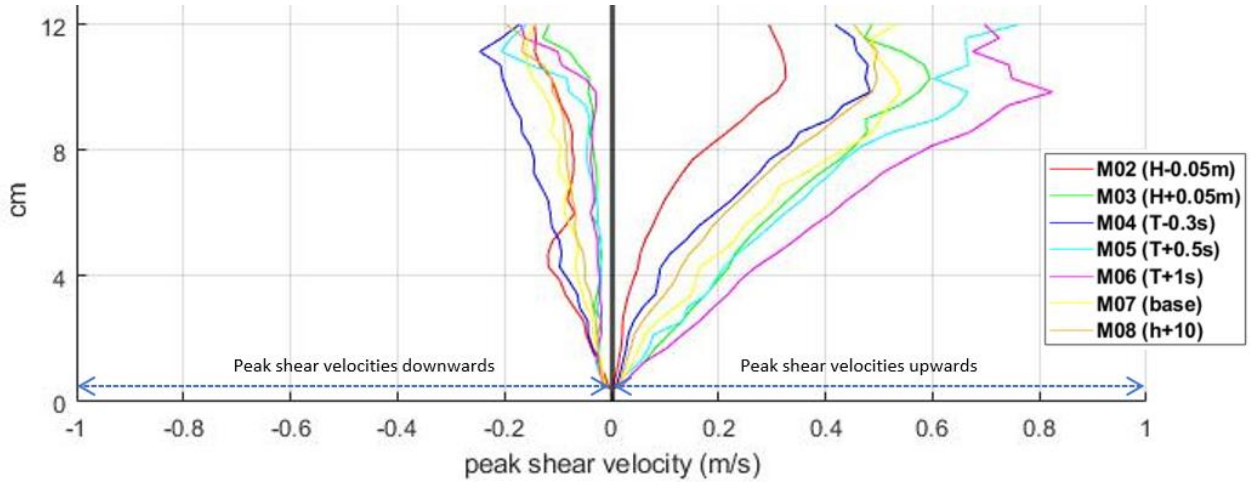

Figure 3-25, The peak near-bed velocities on the 12cm high cliff face. The y-axis represents the cliff height and the x-axis the peak near-bed velocities going upward (positive x-axis) and downward (negative x-axis).

The effects of the parameter changes on the peak near-bed velocities are shown in Table 4. From these values is also concluded that a wave length increase leads, mostly, to higher near bed velocities, where a wave height reduction and a water depth increase reduce the peak near bed velocities.

Table 4, Effect of change in the input characteristics compared with the base scenario in %.

	Parameter changed and experiment ID					
area	H-0,05	H+0,05	T-0,03	T+0,5	T+1	h+0,10
	M02	M03	M04	M05	M06	M08
1 (mudflat)	-60%	-3%	-28%	17%	51%	-60%
2 (cliff face)	-40%	10%	-11%	40%	52%	-8%
3 (marsh to offshore)	-41%	13%	-12%	3%	37%	-21%
4 (marsh to dike)	-18%	-46%	-25%	81%	-8%	-1%

The influence of the combined parameters can be expressed with a parameter like the Ursell number. This parameter is used to visualize a relationship between the peak near-bed velocities, and the offshore wave conditions. The Ursell number (*U*) indicates the non-linearity of waves, and is calculated with the formula shown below in equation 9. In this formula the wave period is represented by the wave length, while the wave height and water depth are also included in the formula.

$$U = \frac{H\,\lambda^2}{h^3} \tag{9}$$

In this equation is H the wave height, λ the wave length and h the water depth. The wave length is calculated in a similar way as done in section 2.5, except that the lookup table is not used, but the wave length is found by iteratively trying values for the wave length to solve the dispersion relation (van der Werf, 2021). The offshore Ursell numbers for the different scenarios (Table 5) are then plotted against the peak near bed velocities (Figure 3-26). The offshore Ursell number is used instead of the Ursell number close to or on the cliff, because around the cliff no linear wave theory can be applied, and thus the wave length is hard to determine.

Table 5, Ursell numbers for the different experiments.

Exp.ID	h offshore (cm)	H (cm)	T (s)	λ (m)	Ursell Number (-)
M02	45	5	1,5	2,7	4
M03	45	15	1,5	2,7	12
M04	45	10	1,2	2,0	4
M05	45	10	2	3,9	17
M06	45	10	2,5	5,0	27
M07	45	10	1,5	2,7	8
M08	55	10	1,5	2,9	5

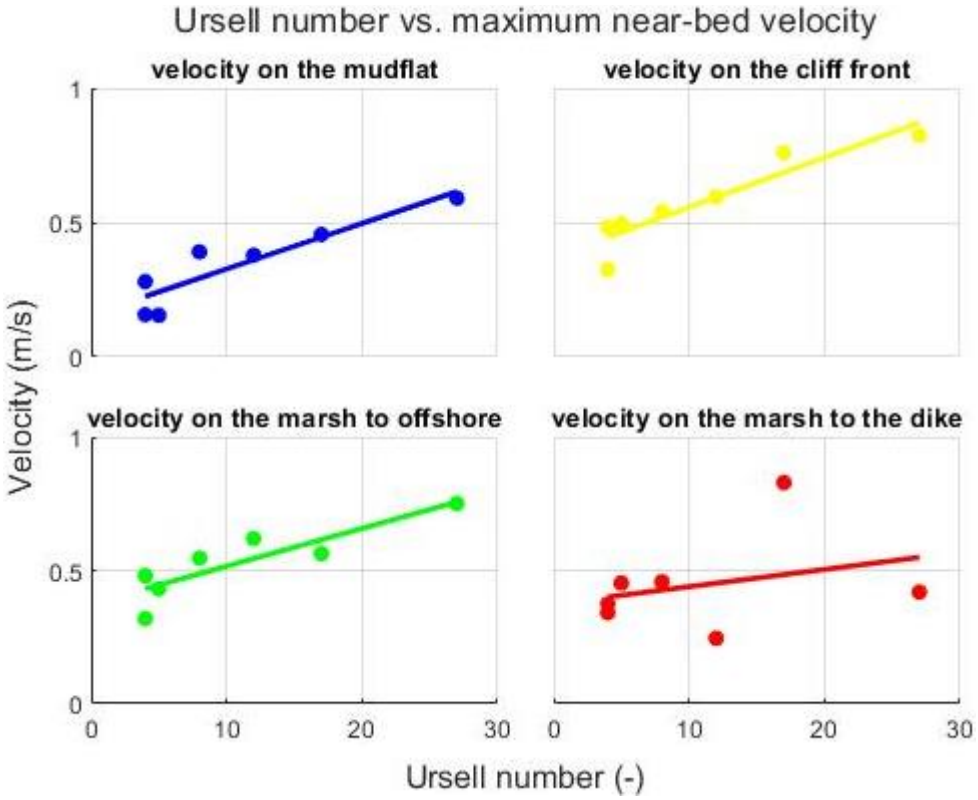

Figure 3-26, Maximal peak near-bed velocities plotted against the Ursell number graphed for the four areas around a cliff that are susceptible to near-bed velocities. The seven dots in every graph represent the different experiments that are conducted.

A trend line has been fitted to for the 7 experiments, and all the locations seem to have a possitive linear relation to the Ursell number, except for the near-bed velocities towards the dike on the saltmarsh. In that area only the M05 scenario, which is the red dot with the high velocity, has a high near bed velocity, 0.8 m/s, while the other scenario remain under 0.5 m/s. By analysing the peak velocity map towards the dike of M05 (Figure 3-27), the flow around the cliff edge bends quickly towards the saltmarsh bed. This is not observed in the other experiments (Figure 3-22(b) and Appendix C).

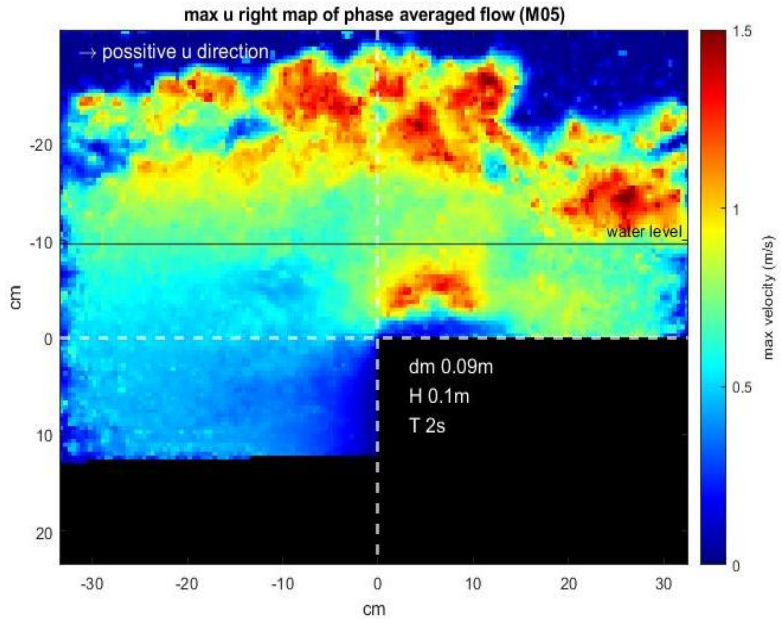

Figure 3-27, M05 experiment, where the velocities moving to the dike reach to the saltmarsh bed, which does not occur in the other experiments.

4. Discussion

This research provides insight into using PIV measurements for studying wave-induced hydrodynamics during storm conditions around a scaled saltmarsh cliff. This discussion will expand on the findings' interpretation, including limitations caused by measurement errors and uncertainties.

Experimental setup

A scaled model of a coastal transect with a foreshore, cliff, saltmarsh and dike in a wave flume is used to analyse wave-induced hydrodynamics around a saltmarsh cliff. The experimental setup is designed on a 1:10 scale according to Froude similitude, which is appropriate for open channel flow, where friction effects are minimal, or for flow patterns that are highly turbulent, as the turbulence dissipates the energy instead of the model (Taveira Pinto, 2020). The waves are assumed to only lose wave energy due to shoaling, until they interact with the return flow and the cliff hydrodynamics, making the surface friction components negligible, and allowing the Froude scaling. However, the effect of the neglected friction forces is unknown.

The presented requirements for a PIV setup are abided by the setup used. The particles are well visible, and its concentration in the water is within boundaries. No peak-locking is observed in the used experiments, and the experiments that caused air bubbles in the near cliff region have been excluded from PIV measurement analysis. For this study the displacement threshold is not exceeded with the near-bed velocities, but the velocities observed in the in the wave crests during experiment M05 and M06 experiments (max 1.5 m/s)(appendix C) do exceed the threshold (1.07 m/s). These velocities magnitudes can not be measured accurately with the 32x32 interrogation window, but with different setting in the PIV software they can be captured (e.g. 64x64 pixel interrogation window).

The Light source used for the PIV measurements in this study is an LED-PIV, which is in-house developed by the Delft University of Technology (Bakker et al.). The use of a LED is unconventional as a laser is mostly used for PIV measurements. Bakker et al. reported on the accuracy of the usage of the LED where they used an interrogation window of 64x64 pixels, where the resolution in this study is 4 times higher (32x32 pixels interrogation window) while keeping the same area of interest (50x70 cm^2). The effect of this increase in resolution is yet unknown, however Bakker et al. reported on an increase in rejected velocity vectors when going from 128x128 to 64x64 pixels interrogation window from 1 to 5 %. A further increase when going to 32x32 can be expected, which could result in too much non-valid vectors in the velocity fields. The LED emits light through the bottom of the flume. The intensity of the light sheet reduces towards the water surface due to the divergence of the light sheet, causing less bright particle captures in the images further from the bed.

The image capturing software drops approximately six frames per 100 on average. The absence of 6 percent of frames results in an absence of 6 velocity frames per 50 frames, which is over 10 percent. This missing data is linearly interpolated, which is not necessarily seen as a problem, except when this would happen in a velocity peak, as interpolation would result in an exclusion of that velocity peak.

Measurements

The measuring method used in this research requires careful validation, since the PIV setup itself is not calibrated. To achieve this, the gathered data has been compared to both a calibrated measurement device (an ADV) and expected theoretical values. The PIV measurements show high similarity to the ADV measurements when a waves passed over the saltmarsh without a cliff and aligns with the maximal orbital velocities expected from linear wave theory (van der Werf, 2021). The comparison with a cliff and its complex flow produced less consistent results when compared with the ADV. The

comparison resulted in RMSE values that are within 15 % of the maximal velocities measured, questioning the validity of the measured velocity fields with a cliff.

To reduce the effect of PIV measurement uncertainty, inconsistencies caused by the wave generator and the impact of missing frames, the velocity fields of 10 fully developed waves are phase-averaged before conducting near-bed velocity analysis. Although this does mitigate the impact of the aforementioned inconsistencies, it assumes that the actual velocity field in a wave phase-would be consistent in all the 10 captured waves. The representation of incidental real velocity peaks can be reduced in the PIV data with this method, but no method is found to judge the validity of these peaks, therefore preferring the reduction of the uncertainty effects by phase-averaging.

The thesis expands the knowledge on the vortex in front of the cliff and peak near-bed velocities that drive erosion. The obtained correlations between the wave period and shear velocities over the mudflat and the cliff front appear significant. Both are influenced by the vortex, where peak near-bed velocities decrease as the wave period decreases, and increasing for longer wave periods with two separate steps. For the areas on top of the saltmarsh that have been assigned as vulnerable, the peak shear velocities are found highly sensitive to an increased wave period.

The vortex formation, both at the face of the cliff and over the saltmarsh platform, are closely linked to the occurrence of peak near-bed velocities. This formation of a vortex in front of the cliff is described by Suzuki & Klaassen's (2011). Here, they apply PTV in a similar scaled wave flume study and further resolve the full flow pattern with a numerical model. In their study, velocity fields are examined with slightly different wave conditions, a 3 cm higher cliff and the foreshore is sloped differently. Their numerical model shows a high similarity in the development of the vortex in front of the cliff as observed in this thesis. Although the velocities are not quantified, the strength and position of the vortex is found to be determined mainly by the wave height and wave period in their study, which is also concluded in the results of this study.

The experiments used in this report are limited in quantity, while more experiments have been conducted in the flume. Due to time scarcity and the complexity of the PIV data handling, no more data is processed, leading to a limited dataset for analysing the effects of changing wave conditions. However, with the seven conducted experiments, a linear relationship is found between the Ursell number and the Maximal near-bed velocity on the mudflat, cliff face and for the return flow over the saltmarsh. Whether this relations holds for all wave conditions, changes in the height of the cliff and when the cliff shape is not a sharp 90 degrees is unknown.

Relation to other studies

In this thesis, the impact of the waves on the cliff face have not been assessed. However, this thesis does show that waves traveling over the saltmarsh during storms have a large impact on the top of the cliff face. This indicates that the processes described by Bendoni et al. (2016) Francalanci et al. (2013) and Tonelli et al. (2010) doesn’t take place during extreme storms in the Netherlands. Lateral cliff erosion measurements taken in the Westernscheldt (Van Der Wal et al. (2023)) may be attributed to the near-bed velocities explained in this report. In their study erosion patterns are found where the upper sections of the cliff are eroded, which result in a multi-stepped cliff. This stepped shape is possibly because of the impact by the generated vortex on the higher cliff surface, similar to a single cliff as treated in this thesis. However, this would imply that storm conditions determine the shape of the cliff, instead of the finding that lateral cliff erosion is primarily driven by common weather conditions (Leonardi et al., 2016; Van Der Wal et al., 2023).

5. Conclusion

Particle Imaging Velocimetry (PIV) has been used to measure 2D wave-induced velocity fields around a saltmarsh cliff under extreme storm conditions. With these velocity fields this report aims to improve the understanding of flow velocity patterns around a cliff that govern cliff erosion. To this end four research questions were formulated, which are answered in this section.

RQ1. What are the requirements to carry out 2D PIV measurements in a complex hydrodynamic region of a saltmarsh cliff?

Particles are illuminated with a LED-PIV at 2 different moments, resulting in 2 images from which the particle displacement between them is calculated. While it seems obvious, the particles in the images should be larger than one pixel, otherwise the PIV software will not function accurately. The concentration of the particles in the water needs to be within the right boundaries, which depends on the desired vector resolution. A vector is created in every interrogation window, 32x32 pixels, in which on average 10 particles should be present. The particle displacement between the two illuminations should not exceed half an interrogation window to accurately measure the velocity vectors. A last requirement involves the occurrence of material in the water that does not share the density of water, which will result in velocities that differ from the water flow. During the experiments for this report, air bubbles are created by waves that break on the cliff. These bubbles are interpreted as big particles by the PIV software, resulting in false velocity fields.

RQ2. How well can PIV measure velocities in a complex region of a saltmarsh cliff compared to other measuring techniques in terms of accuracy.

For several locations in the PIV velocity fields, comparisons are made with ADV measurements in a scenario without a cliff. The PIV and the ADV show almost identical velocities, resulting in marginal RMSE values and no bias is found. Only near a surface (the bed in this case), the velocity vector perpendicular to that surface shows inaccuracies, however this perpendicular direction is of no interest in this report. The maximal velocities measured with PIV align with the maximal orbital velocities that were expected based on linear wave theory.

When a cliff is implemented, the resulting comparison between the PIV and ADV velocity vectors are further off. The RMSE values were in the order of 15 % of the maximal measured velocities, questioning the interpretation of the measured PIV velocity fields around the cliff.

RQ3. What wave-induced near-bed velocities patterns are critical for erosion of a saltmarsh cliff during storm conditions?

various velocity field patterns are observed around a saltmarsh cliff. These include stokes drift, return flow, a vortex in front of the cliff, and a vortex on top of the saltmarsh. This study confirms the impact of wave characteristics on the vortex in front of the cliff, as described by Suzuki & Klaassen (2011). Increasing wave heights and especially longer wave periods create a larger and stronger vortex in front of the cliff, although this effect appears to be absent when waves directly plunge when they reach the cliff.

RQ4. what is the effect of differing wave characteristics on the peak near-bed velocities that drive erosion?

By analysing peak near-bed velocity fields, four areas are found to be vulnerable to erosion caused by high near-bed velocities: 1) The offshore mudflat in front of the cliff, 2) The cliff face, 3) The saltmarsh platform immediately after the cliff edge, and 4) The saltmarsh platform further towards the dike. The

vortex in front of the cliff is the reason of the near-bed velocities on the mudflat directed towards the dike, and the upward velocities on the cliff face. The saltmarsh platform immediately after the cliff edge is susceptible to both the return flow and the vortex on top of the platform, which are both directed offshore. On the salt marsh platform further towards the dike, there are high near-bed velocities towards the dike. These occur as the wave crest passes over this region.

The water depth, wave height and wave period parameters have been varied to assess their influence on the maximal near-bed velocity in the four areas. The wave period is found to be most influential. A more general relationship between the three parameters has been found for location 1, 2 and 3: the Ursell number. A plot of the maximal near-bed velocity versus the Ursell number shows a positive linear trend at those locations.

Objective: ***To understand and quantify the near-bed wave-induced velocities as a proxy for cliff erosion of a coastal saltmarsh, using 2D PIV.***

The objective is achieved for the largest part in this study. The setup used in this study meets the requirements to conduct PIV at this scale, with use of a LED light source instead of a conventional laser. The comparison of the PIV measurements to the ADV measurements failed to prove high accuracy when a cliff is present, questioning the magnitudes of the measured near-bed velocities. However, the extracted velocity fields show clear flow patterns, with limited outliers, enabling us to understand the processes that govern near-bed velocities, and deriving a relation of the maximal near-bed velocities to the offshore wave conditions.

6. Recommendations

PIV potential

In this thesis velocity fields, acquired with PIV, are analysed around a cliff. The research potential of these velocity fields is much greater than performed in this study. In this thesis the maximal near-bed velocities around a cliff have been analysed under different wave conditions and regions vulnerable to high near-bed velocities have been located. Efforts have been made to uncover relationships between wave characteristics and near-bed velocities around the cliff; however, some effects remain uncertain or unknown. On the cliff face clear relationships have been found, but the processes that govern high near-bed velocities on the saltmarsh remain partially unknown. The resulting data suggests that the vortex creation on top of the saltmarsh is important. The off shore Ursell number is presented to have a relationship with the maximal near-bed velocity, but the amount of experiments this is based on, 7, is relatively low. Including more experiments could lead to a stronger or non-linear relationship.

Other validation/comparison methods

The comparison between the PIV and ADV in the scenario with a cliff concluded limited similarity. Both the PIV and ADV showed weird orbital cycle patterns in their velocity vectors, resulting in high RMSE values. A comparison of the PIV velocity fields with an numerical model could result in a higher correlation. A numerical model could calculate the full velocity field, instead of the point measurements from the ADV, resulting in more data points to compare, or the PIV data can be used to calibrate the numerical model. With this comparison local accuracy could be determined for the PIV, where the near bed vector accuracy would be of the highest interest for this study.

Other measurement devices

Next to near-bed stresses, pressure differences in the water column can also lead to cliff erosion by pushing and pulling on the soil of the cliff face and saltmarsh platform. Research in this field should reveal how the vorticity of the vortex in front of the cliff and on top of the saltmarsh affect this. The data from the pressure sensors in the mudflat, cliff and saltmarsh that incorporated in the flume setup of this study could help with further research .

Further research in this field should aim to understand how the vorticity of the vortex in front of the cliff and on top of the saltmarsh influences these pressure dynamics. Utilizing data from pressure sensors embedded in the mudflat, cliff, and saltmarsh, which were incorporated within the flume setup for this study, could provide valuable insights for future research in this area.

Vegetation influence

Next to more research into the hydrodynamics caused by a cliff, the effect of saltmarsh vegetation on the velocity field around the cliff should be studied as well. The vegetation is expected to reduce flow velocities near the bed, which compresses the velocity profile upwards. A return flow on top of the vegetation could lead to a higher position of the vortex in front of the cliff, making the cliff edge more vulnerable to erosion. These processes can be analysed by comparing non-vegetated and vegetated velocity fields. As explained in the methodology, other wave experiments have been performed including scaled vegetation saltmarsh meadow . Further analysing this data on the effect of a different return flow pattern due to vegetation compared with the results of this thesis is recommended.

Bibliography

Arunakumar, H. S., Suvarna, P., Abhijith, P. A., Prabhu, A. S., Pruthviraj, U., & Kamath, A. (2019). Effect of Emerged Coastal Vegetation on Wave Attenuation Using Open Source CFD Tool: REEF3D. In K. Murali, V. Sriram, A. Samad, & N. Saha (Eds.), *Proceedings of the Fourth International Conference in Ocean Engineering (ICOE2018)* (Vol. 22, pp. 591–603). Springer Singapore. https://doi.org/10.1007/978-981-13-3119-0_37

Bakker, W., Hofland, B., De Almeida, E., Oldenziel, G., & J Overmars, E. F. (2021). Pulsed LED line light for large-scale PIV—development and use in wave load measurements. *Measurement Science and Technology*, *32*(11), 115205. https://doi.org/10.1088/1361-6501/ac17ce

Bendoni, M., Georgiou, I. Y., & Novak, A. B. (2021). Marsh Edge Erosion. In D. FitzGerald & Z. Hughes (Eds.), *Salt Marshes* (1st ed., pp. 388–422). Cambridge University Press. https://doi.org/10.1017/9781316888933.018

Bendoni, M., Mel, R., Solari, L., Lanzoni, S., Francalanci, S., & Oumeraci, H. (2016). Insights into lateral marsh retreat mechanism through localized field measurements: MARSH RETREAT MECHANISM. *Water Resources Research*, *52*(2), 1446–1464. https://doi.org/10.1002/2015WR017966

Brodeur, J. (2022). *NOAA Blue Carbon White Paper*. https://doi.org/10.25923/V5FX-R089

Cameron, S. M. (2022). Theoretical description of PIV measurement errors. *Acta Geophysica*, *70*(5), 2379–2387. https://doi.org/10.1007/s11600-022-00901-9

Cao, H., Zhu, Z., Herman, P. M. J., Temmerman, S., Smit, J., Zhang, L., Yuan, L., & Bouma, T. J. (2021). Plant traits determining biogeomorphic landscape dynamics: A study on clonal expansion strategies driving cliff formation at marsh edges. *Limnology and Oceanography*, *66*(10), 3754–3767. https://doi.org/10.1002/lno.11915

Chen, D., Tang, J., Xing, F., Cheng, J., Li, M., Zhang, Y., Shi, B., Shi, L., & Wang, Y. P. (2023). Erosion and accretion of salt marsh in extremely shallow water stages. *Frontiers in Marine Science*, *10*, 1198536. https://doi.org/10.3389/fmars.2023.1198536

COGNEX. (2020). *Checkerboard calibration*. Checkerboard Calibration. https://support.cognex.com/docs/apasap_430/web/EN/ConceptsGuide/Content/Topics/Concept/Calib/Types/Checker/Checkerboard%20Calibration.htm#:~:text=Checkerboard%20calibration%20computes%20intrinsic%20parameters,are%20free%20of%20these%20distortions.

Dabiri, D. (2007). *Cross-Correlation Digital Particle Image Velocimetry – A Review*.

DeltaProgramma. (2023). *NATIONAAL DELTAPROGRAMMA 2023* [Overheid]. deltaprogramma. https://dp2023.deltaprogramma.nl/

Ecoshape. (2022). *Growing salt marshes*. EcoShape. https://www.ecoshape.org/en/concepts//growing-salt-marshes

EEA. (2022). *Global and European sea level rise* [Https://www.eea.europa.eu/]. European Environment Agency's. https://www.eea.europa.eu/ims/global-and-european-sea-level-rise

Evonik. (2022). *POLYAMIDE 12 POWDERS FROM EVONIK*. Vestosint. https://www.vestosint.com/en

Fagherazzi, S. (2019). *Shoreline erosion of the tidal marsh adjacent to Plum Island Sound*. https://lternet.edu/findings/sea-level-rise-and-storms-are-altering-salt-marshes/

Fagherazzi, S., Mariotti, G., Leonardi, N., Canestrelli, A., Nardin, W., & Kearney, W. S. (2020). Salt Marsh Dynamics in a Period of Accelerated Sea Level Rise. *Journal of Geophysical Research: Earth Surface*, *125*(8). https://doi.org/10.1029/2019JF005200

Francalanci, S., Bendoni, M., Rinaldi, M., & Solari, L. (2013). Ecomorphodynamic evolution of salt marshes: Experimental observations of bank retreat processes. *Geomorphology*, *195*, 53–65. https://doi.org/10.1016/j.geomorph.2013.04.026

Houttuijn Bloemendaal, L. J., FitzGerald, D. M., Hughes, Z. J., Novak, A. B., & Georgiou, I. Y. (2023). Reevaluating the wave power-salt marsh retreat relationship. *Scientific Reports*, *13*(1), 2884. https://doi.org/10.1038/s41598-023-30042-y

Kislaya, A. (2016). *Estimation and reduction of peak-locking errors in PIV measurements* (p. 114) [Msc Thesis]. TU Delft. https://repository.tudelft.nl/islandora/object/uuid%3A9ecec1a5-e3fa-4468-9ac0-e6ffacaa1905

Koppel, J. van de, Wal, D. van der, Bakker, J. P., & Herman, P. M. J. (2005). Self-Organization and Vegetation Collapse in Salt Marsh Ecosystems. *The American Naturalist*, *165*(1), E1–E12. https://doi.org/10.1086/426602

Leonardi, N., Ganju, N. K., & Fagherazzi, S. (2016). A linear relationship between wave power and erosion determines salt-marsh resilience to violent storms and hurricanes. *Proceedings of the National Academy of Sciences*, *113*(1), 64–68. https://doi.org/10.1073/pnas.1510095112

Meijer, M. C. (2005). *A numerical implementation of vegetation in SWAN*. Delft University of Technology. http://resolver.tudelft.nl/uuid:60eddf18-2289-47f5-b76c-5e989a1167ff

Muller, J. R. M. (2023). *Living Dikes Project: PIV images callibration reports*. University of Twente.

Nepf, H. M. (1999). Drag, turbulence, and diffusion in flow through emergent vegetation. *Water Resources Research*, *35*(2), 479–489. https://doi.org/10.1029/1998WR900069

Nepf, H. M. (2012). Flow and Transport in Regions with Aquatic Vegetation. *Annual Review of Fluid Mechanics*, *44*(1), 123–142. https://doi.org/10.1146/annurev-fluid-120710-101048

Nieboer, H. (n.d.). *Natural Coasts*. Nature Based Solutions. https://www.nature-basedsolutions.com/natural-coasts

NORTEK. (2023). *Vector—300m*. Nortekgroup. https://www.nortekgroup.com/products/vector-300-m

NWO. (2022, January 5). *Salt marshes for climate-resilient coastal defences*. Salt marshes for climate-resilient coastal defences. https://www.nwo.nl/en/cases/salt-marshes-climate-resilient-coastal-defences

Raffel, M., Willert, C. E., Wereley, S. T., & Kompenhans, J. (2007). *Particle Image Velocimetry: A Practical Guide*. Springer Berlin Heidelberg. https://doi.org/10.1007/978-3-540-72308-0

Rahman, A. (2015). *Cliff Erosion of salt marshes*. University of Twente. https://purl.utwente.nl/essays/68055

Rijkswaterstaat. (2023). *Watersnoodramp 1953* [Rijkswaterstaat]. Bescherming Tegen Het Water. https://www.rijkswaterstaat.nl/water/waterbeheer/bescherming-tegen-het-water/watersnoodramp-1953

Suzuki, T., & Klaassen, P. C. (2011). Hydrodynamics on seedlings of halophytic plants around a salt marsh cliff. *Journal of Coastal Research*, *64*.

Taveira Pinto, F. (2020). *Scaling Issues in Hydraulic Modelling*. Coastalwiki. https://www.coastalwiki.org/wiki/Scaling_Issues_in_Hydraulic_Modelling

Taylor, Z. J., Gurka, R., Kopp, G. A., & Liberzon, A. (2010). Long-Duration Time-Resolved PIV to Study Unsteady Aerodynamics. *IEEE Transactions on Instrumentation and Measurement*, *59*(12), 3262–3269. https://doi.org/10.1109/TIM.2010.2047149

Thielicke, W. (2023, April 12). *PIVlab*. https://nl.mathworks.com/matlabcentral/fileexchange/27659-pivlab-particle-image-velocimetry-piv-tool-with-gui

Tonelli, M., Fagherazzi, S., & Petti, M. (2010). Modeling wave impact on salt marsh boundaries. *Journal of Geophysical Research*, *115*(C9), C09028. https://doi.org/10.1029/2009JC006026

University College London. (2019). *Calibration*. https://mphy0026.readthedocs.io/en/latest/calibration/calibration.html

Van Der Wal, D., Van Dalen, J., Willemsen, P. W. J. M., Borsje, B. W., & Bouma, T. J. (2023). Gradual versus episodic lateral saltmarsh cliff erosion: Evidence from Terrestrial Laser Scans (TLS) and Surface Elevation Dynamics (SED) sensors. *Geomorphology*, *426*, 108590. https://doi.org/10.1016/j.geomorph.2023.108590

van der Werf, J. J. (2021). *Syllabus Wave-Dominated Coastal Dynamics*.

Van Loon-Steensma, J. M. (2015). Salt marshes to adapt the flood defences along the Dutch Wadden Sea coast. *Mitigation and Adaptation Strategies for Global Change*, *20*(6), 929–948. https://doi.org/10.1007/s11027-015-9640-5

van Loon-Steensma, J. M., van Duin, W. E., de Groot, A. V., van Wesenbeeck, B. K., & Smale, A. J. (2012). *Zoekkaart Kwelders en waterveiligheid Waddengebied* (p. 64). Altera.

Van Veelen, T. J., Karunarathna, H., & Reeve, D. E. (2021). Modelling wave attenuation by quasi-flexible coastal vegetation. *Coastal Engineering*, *164*, 103820. https://doi.org/10.1016/j.coastaleng.2020.103820

Willemsen, P. W. J. M., Borsje, B. W., Hulscher, S. J. M. H., Van Der Wal, D., Zhu, Z., Oteman, B., Evans, B., Möller, I., & Bouma, T. J. (2018). Quantifying Bed Level Change at the Transition of Tidal Flat and Salt Marsh: Can We Understand the Lateral Location of the Marsh Edge? *Journal of Geophysical Research: Earth Surface*, *123*(10), 2509–2524. https://doi.org/10.1029/2018JF004742

Willemsen, P. W. J. M., Borsje, B. W., Vuik, V., Bouma, T. J., & Hulscher, S. J. M. H. (2020). Field-based decadal wave attenuating capacity of combined tidal flats and salt marshes. *Coastal Engineering*, *156*, 103628. https://doi.org/10.1016/j.coastaleng.2019.103628

Ziegler, S. L., Baker, R., Crosby, S. C., Colombano, D. D., Barbeau, M. A., Cebrian, J., Connolly, R. M., Deegan, L. A., Gilby, B. L., Mallick, D., Martin, C. W., Nelson, J. A., Reinhardt, J. F., Simenstad, C. A., Waltham, N. J., Worthington, T. A., & Rozas, L. P. (2021). Geographic Variation in Salt Marsh Structure and Function for Nekton: A Guide to Finding Commonality Across Multiple Scales. *Estuaries and Coasts*, *44*(6), 1497–1507. https://doi.org/10.1007/s12237-020-00894-y

Appendix A: PIV measuring principle

The displacement of the tracer particles is not followed as a trajectory with PIV. The assumption is made that for small volumes the velocity direction and magnitude is the same (Bakker et al., 2021; Raffel et al., 2007). The timing of the images, the activation of the LED-PIV and the vector calculations are explained in this section for 2D PIV. For a constant terminology the setup of this study is used for explanation of the PIV measuring principles. The principles do not change when using a laser as a light source or conduction experiments in another substance than water, such as air.

A camera has a period in which the shutter is open. Old cameras take a long time to catch enough light, modern cameras have memory cards in which each photosite (mostly referred to as pixel) react to light. By controlling the moments on which a particle can reflect light, by activating the LED-PIV, it is exactly known when a particle is reflecting light. The time schedule in the figure below shows how pictures are taken in the top timeline, and when the sensor receives light because the LED-PIV is turned on (Taylor et al., 2010). Pictures are paired by the LED pulses that are closest to each other (one Δt divided from each other).

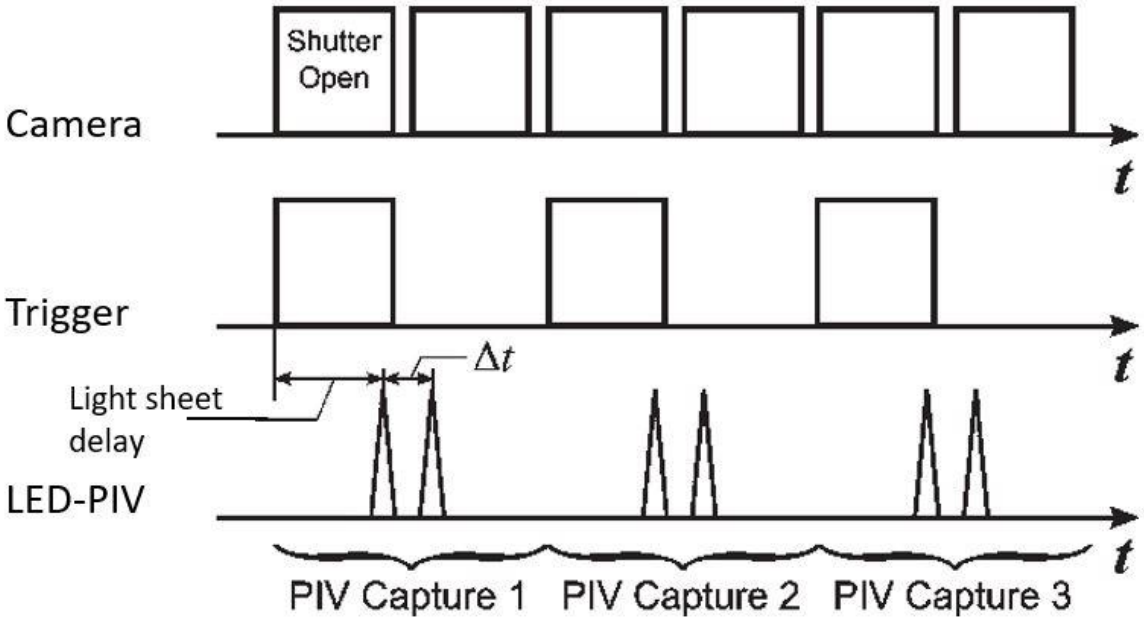

The first two shutter openings are described as an example:

- Camera shutter opens in a darkroom, so no light is caught. When the shutter is almost going to close the LED-PIV is activated for a very short amount of time (referred to as the light pulse) then the shutter closes and thus the reflection of particles during the light pulse is the only light caught by the sensor.
- Then the shutter opens again and immediately a light pulse is activated again. For the rest of the shutter time no light is emitted so the light pulse at the start of the picture is again the only light caught.
- This results in two frames that are a pair (named PIV Capture 1 in the figure above). Even though the pictures are taken at other moments, the moment the data is gathered is only during the light pulses and thus it is known how much time is spent between the particles captured in both frames.

A frame pair can be used to approximate the movement pattern within that timestep using cross-correlation. Cross-correlation is a statistical method in which the most probable displacement of particles within a sample domain is calculated, and results into a velocity vector in that domain (Dabiri, 2007). The figure on the next page is used as an example to clarify this:

- The frames consist of reflecting particles on a black background. Since only particles in the thin light sheet are illuminated, only that part is captured and in plane motion is detected.
    - The first frame is the first frame of the pair (thus the first light pulse)
    - The second frame is the second frame of the pair (second light pulse)
    - The time between them is Δt
- The dots are the illuminated particles (also referred to as seeding)
- The images are sampled into interrogation windows (e.g. 32x32pixels) and for every interrogation window a pixel shift (dx, dy) is determined with Cross-correlation between the first and second image. The size of the interrogation window therefore determines the spatial resolution. In the left bottom of the figure below a resulting correlation plane is shown.
    - The plane represents the directions in which the first interrogation window is shifted. In the centre spot of the plane interrogation is not shifted.
    - The height of the peaks in the plane show how well the particle locations in the shifted interrogation window correspond to the interrogation window of the second frame.
    - The location of the highest correlation peak represents the most likely displacement of the particles from the first to the second frame.
- The determined displacement in combination with the known time between the first and second frame results in a velocity vector.
    - The maximal expected displacement in the timestep should not exceed half of the interrogation window, because the particles of the first frame should also be in the second interrogation window. Therefore the relationship between the timestep and the interrogation window size must be in the right order.
- If the whole picture is split in areas and interpreted with cross-correlation, the right side of the figure below shows a possible resulting vector field.
- Because the vectors are statistically determined, there is a chance that vectors are incorrect. The minimization of this occurrence and the filter setting applied to deal with outliers is discussed in section 2.3.

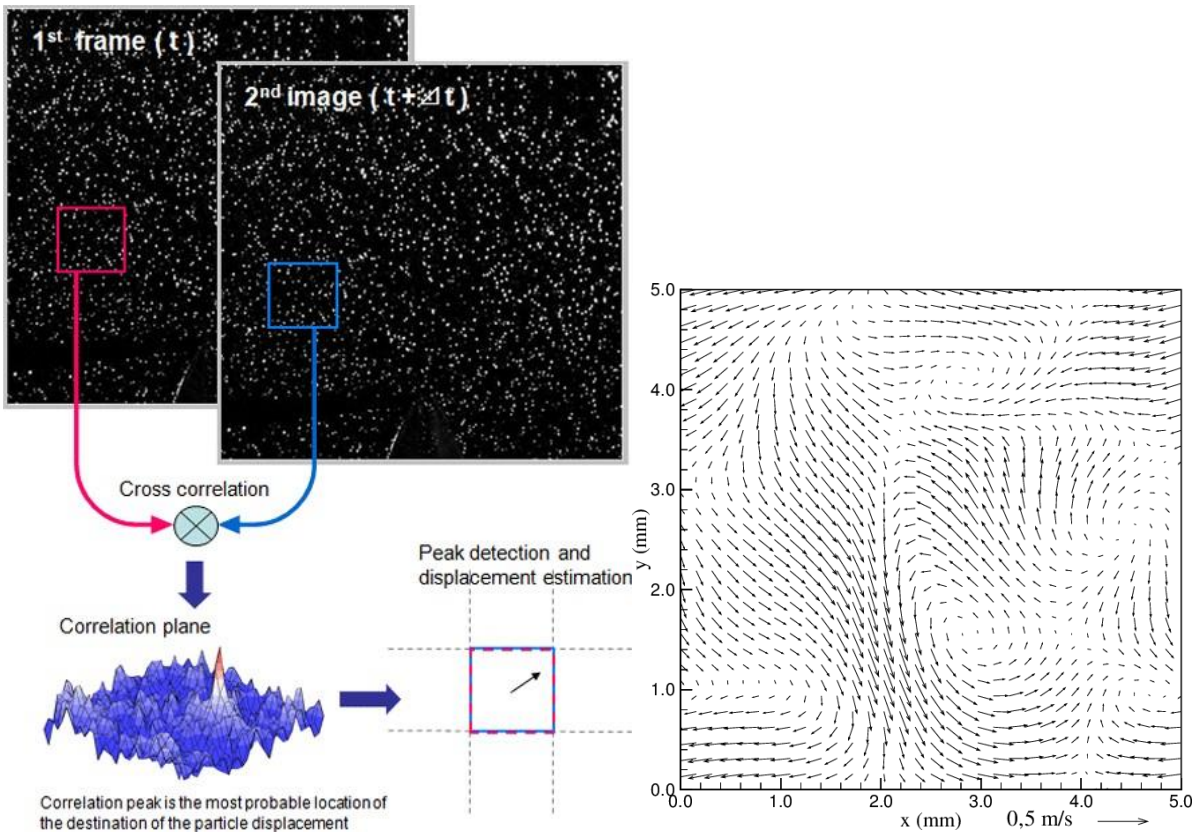
1st frame (t)
2nd image (t +⊿t)
Cross correlation
Correlation plane
Peak detection and
displacement estimation
Correlation peak is the most probable location of
the destination of the particle displacement
5.0
4.0
3.0
2.0
1.0
0.0
y (mm)
0.0
1.0
2.0
3.0
4.0
5.0
x (mm)
0,5 m/s

Appendix B: Time-averaged velocity maps

In this appendix the time-averaged velocity maps are presented for comparison with the base experiment, which is presented in the results. The wave characteristics are plotted in the saltmarsh elevation, which are: dm=0.09m, H=0.10m and T=1.5s; in the base experiment M07.

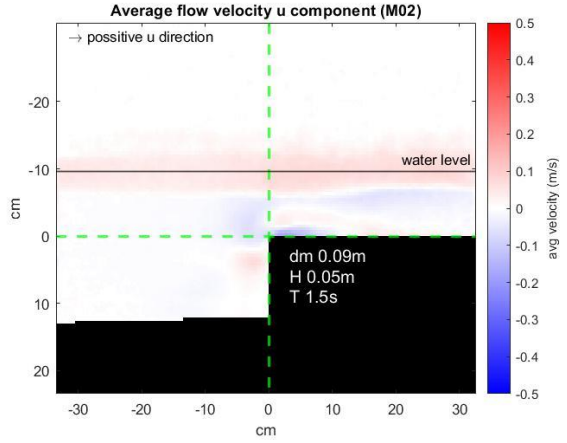

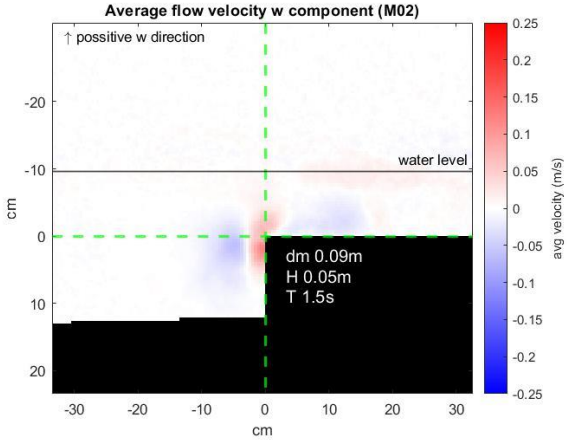

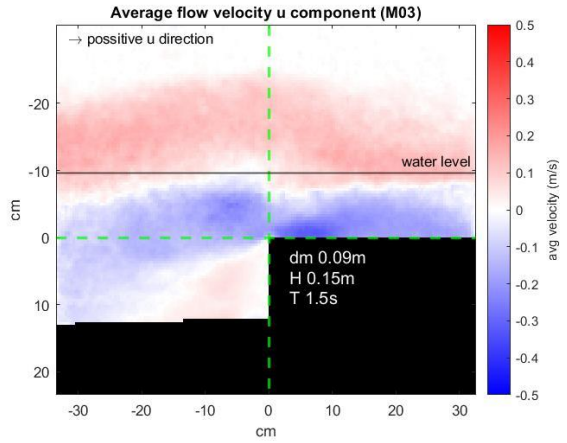

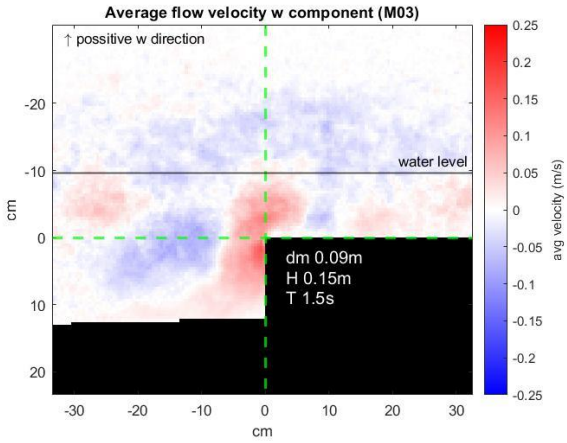

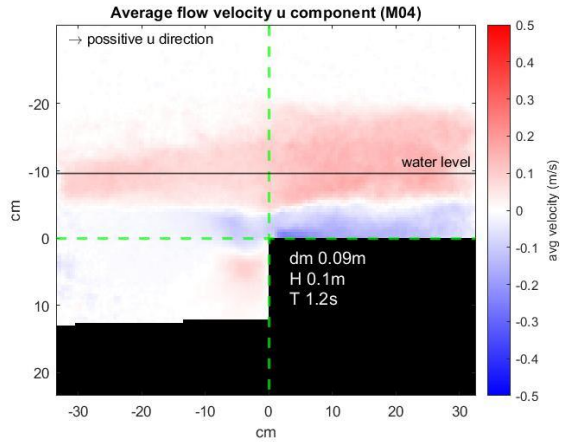

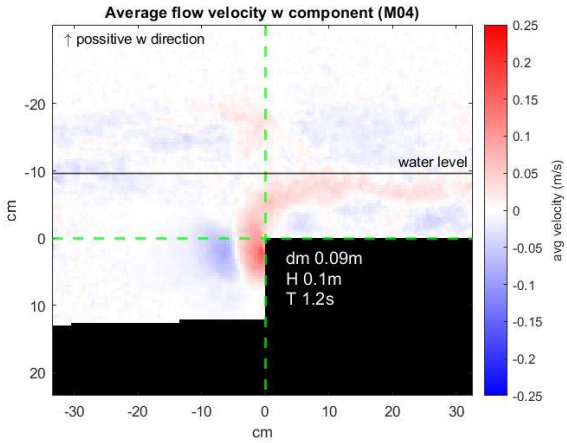

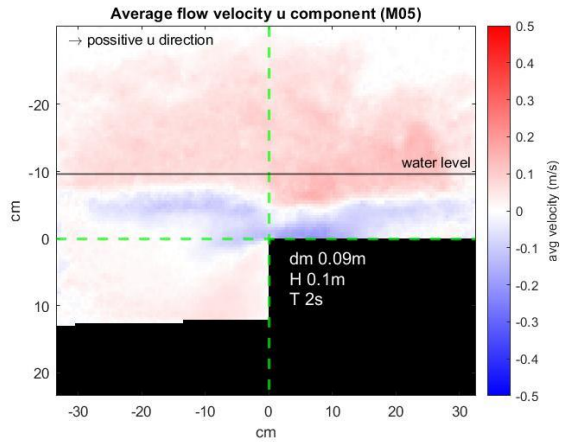
Average flow velocity u component (M05)
→ possitive u direction
water level
dm 0.09m
H 0.1m
T 2s
cm
avg velocity (m/s)

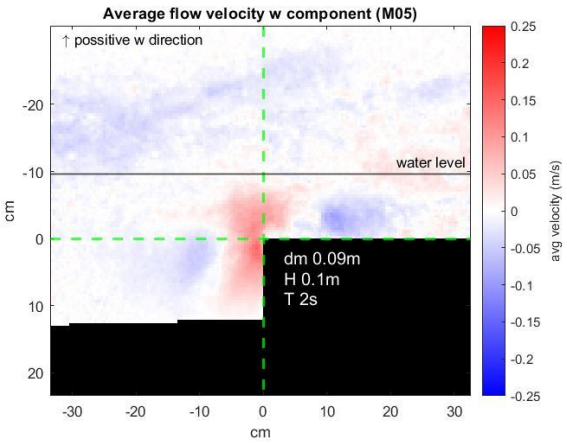
Average flow velocity w component (M05)
↑ possitive w direction
water level
dm 0.09m
H 0.1m
T 2s
cm
avg velocity (m/s)

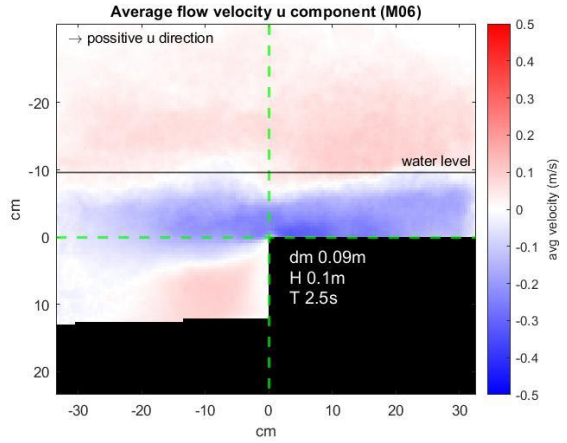
Average flow velocity u component (M06)
→ possitive u direction
water level
dm 0.09m
H 0.1m
T 2.5s
cm
avg velocity (m/s)

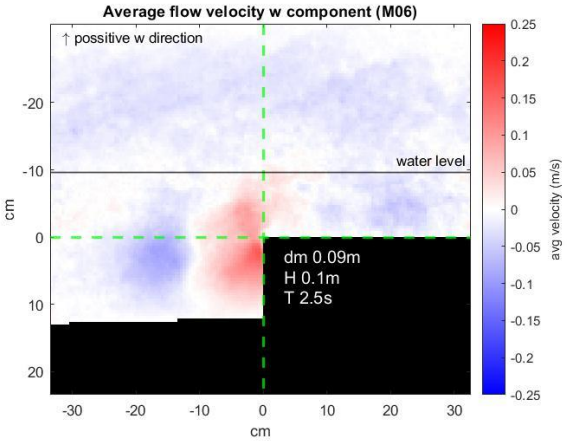
Average flow velocity w component (M06)
↑ possitive w direction
water level
dm 0.09m
H 0.1m
T 2.5s
cm
avg velocity (m/s)

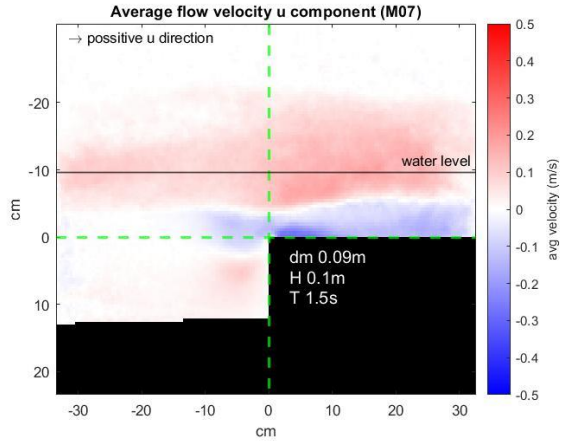
Average flow velocity u component (M07)
→ possitive u direction
water level
dm 0.09m
H 0.1m
T 1.5s
cm
avg velocity (m/s)

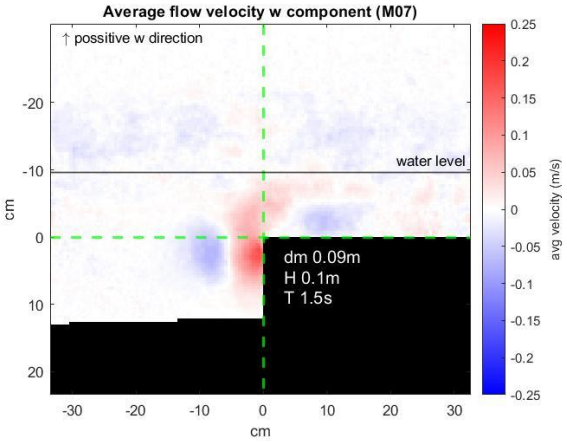
Average flow velocity w component (M07)
↑ possitive w direction
water level
dm 0.09m
H 0.1m
T 1.5s
cm
avg velocity (m/s)

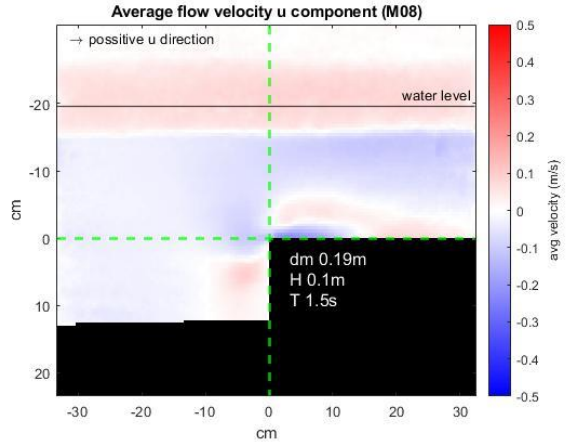
Average flow velocity u component (M08)
→ possitive u direction
water level
dm 0.19m
H 0.1m
T 1.5s
cm
avg velocity (m/s)

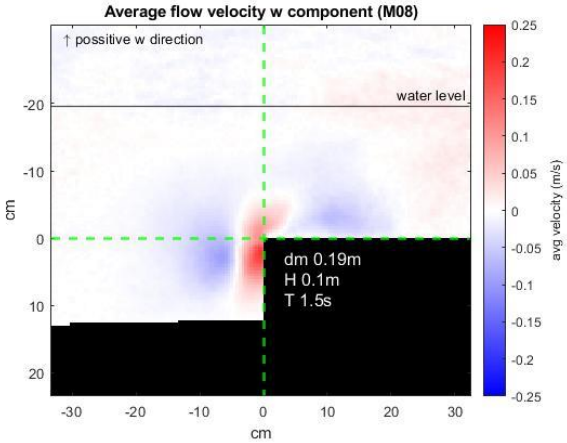
Average flow velocity w component (M08)
↑ possitive w direction
water level
dm 0.19m
H 0.1m
T 1.5s
cm
avg velocity (m/s)

Appendix C: Phase-averaged peak velocity maps

In this appendix phase-averaged peak velocity fields are shown for a comparative purpose. First the upward velocities are shown for the experiments that are not visualized in section 3.3.2. in which the top of the cliff face is the area of interest.

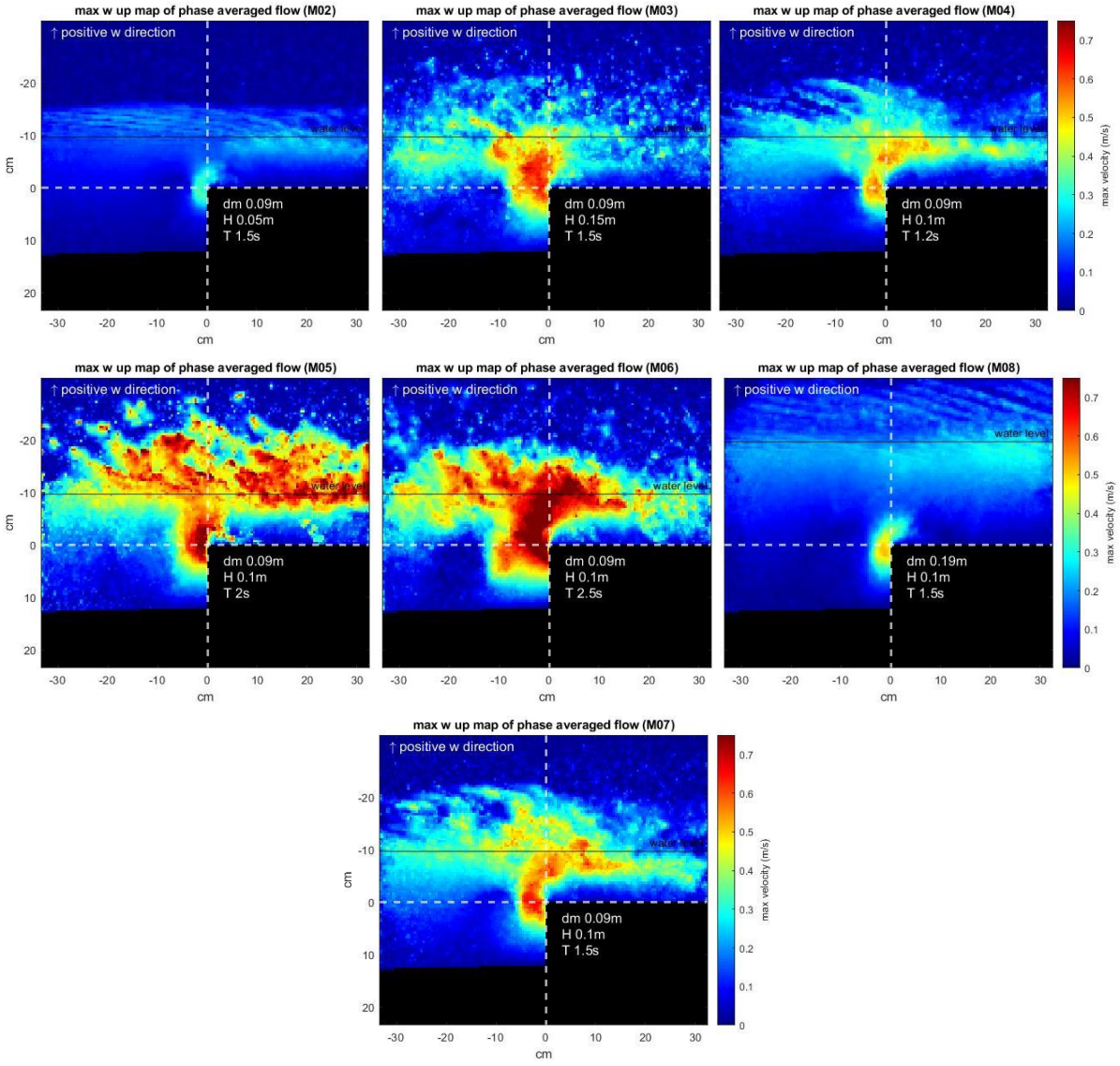

The peak velocity component to the right is shown here for illustration of the near-bed velocities on the off shore mud flat and on the saltmarsh.

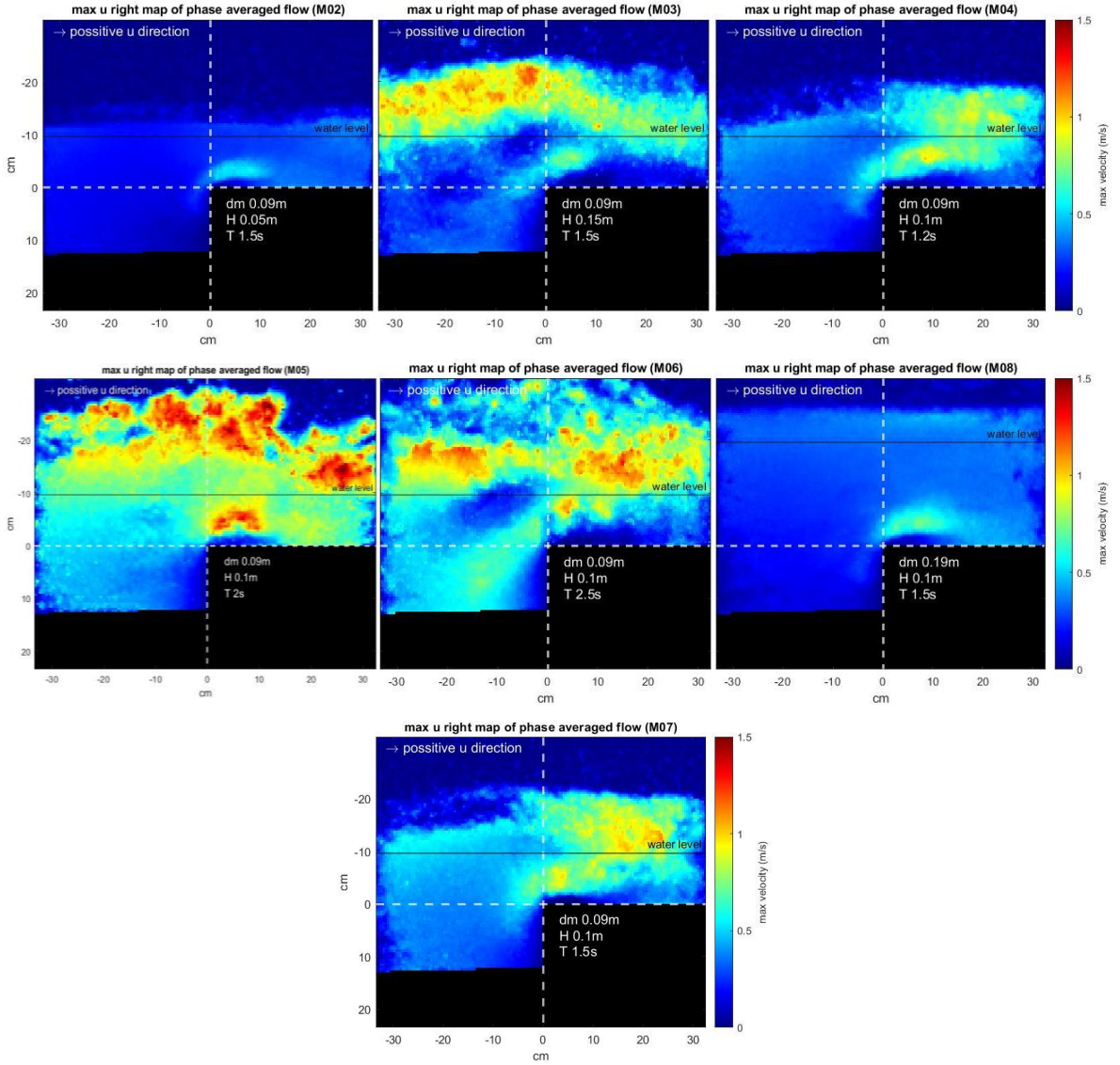

The peak velocities towards the left are shown here. The area that is vulnerable to near-bed velocities in this direction is on the saltmarsh.

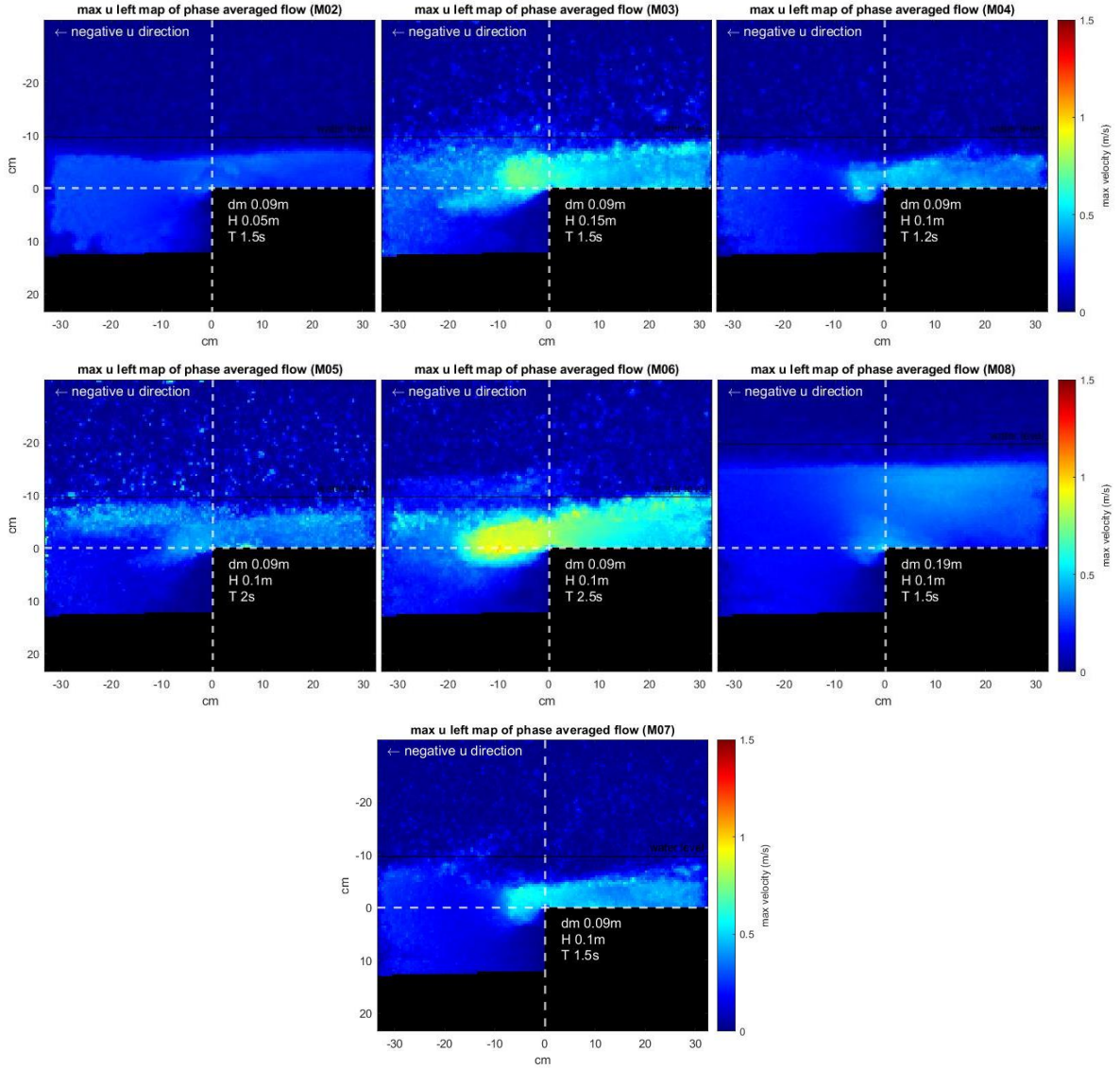

The peak velocity component downwards are presented for all the experiments. However, there is no region highly susceptible to this component.